INVESTIGATING THE MECHANISMS THAT REGULATE DIFFERENCES IN SCLERAL CARTILAGE MORPHOLOGY AMONGST TELEOSTS

by

Nicholas W. Zinck

Submitted in partial fulfilment of the requirements

for the degree of Master of Science

at

Dalhousie University

Halifax, Nova Scotia

July 2021

Table of Contents

List of Tables

List of Figures

Abstract

The vertebrate ocular skeleton is comprised of the scleral ossicles and scleral cartilage. The scleral cartilage can vary drastically in morphology across vertebrate taxa, from a cup-like structure in reptiles and birds, to a narrow ring like structure around the equator of the eye in teleosts. Very little is known about the development of teleost scleral cartilage. Thus, this thesis aims to generate an understanding of the mechanisms that regulate teleost scleral cartilage development in morphology. The research presented in this thesis is divided into two main sections. A descriptive analysis of scleral cartilage development and morphology in the surface and Pachón cave morphs of the Mexican tetra (*Astyanax mexicanus*) as well as the zebrafish (*Danio rerio*) was conducted and several differences in the patterning of the development of this cartilage were found. These differences consist of differential timing of scleral cartilage emergence and growth, as well as in the relative depth of scleral cartilage, and chondrocyte size. However, several similarities were also found. These include similar tendencies towards deeper scleral cartilage in the caudal segment of the cartilage ring during development, as well as a similar offset of the scleral cartilage with respect to the optic cup tissues. Next, an inhibition experiment designed to disrupt FGF and TGF-ß pathway signaling during scleral cartilage development via intravitreal injection was conducted in the zebrafish. Intravitreal inhibitor injection did not produce the hypothesized disruptive effect on the scleral cartilage. However, several effects in other cranial cartilages, including the epiphyseal bar, which shares origin with the scleral cartilage, as well as in the basihyal cartilage, and the basicapsular cartilage were found. Reasons for these differential effects are discussed and may relate to their neural crest origin. In conclusion, this thesis provides an increased understanding of scleral cartilage morphology and development in teleosts and serves as a foundation for future research on the mechanisms regulating teleost scleral cartilage induction.

List of Abbreviations and Symbols

° - degree

µL – microliter

µm – micrometer

ALK-1 – activin-like kinase-1

BMP – bone morphogenetic protein

DMSO – dimethyl sulfoxide

E – embryonic day

ECM – extracellular matrix

EMI – epithelial-mesenchymal interaction

FGF – fibroblast growth factor

FGFR – fibroblast growth factor receptor

HBQ – Hall and Brunt quadruple stain

HH – Hamilton Hamburger stage

mL - millilitre

mm – millimetre

N-CAM – neural cell adhesion molecule

nL – nano liter

NR – neural retina

NT – non-treated

PBS – phosphate buffered saline

PC – principal component

PCA – principal component analysis

PFA – paraformaldehyde

POM – periocular mesenchyme

RPE – retinal pigment epithelium

SC – scleral cartilage

SD – standard deviation

TGF-ß – transforming growth factor beta

WNT – wingless/integrated

Acknowledgements

I would thank Tamara Franz-Odendaal, PhD, for providing me the opportunity to grow as a scientist and an individual during my time in her lab. Thank you for the guidance, support, and kindness. It has all been greatly appreciated. To my committee members, Angelo Iulianella, PhD, Boris Kablar, MD, PhD, and Kazue Semba, PhD, thank you for your invaluable input, advice, and constructive criticism. Thank you to all members of the Bone Development Lab for your kindness and comradery. Specifically, I thank Dr. Franz-Odendaal, Dr. Jennifer Giffin, and Dr. Shirine Jeradi, for teaching me the techniques necessary to complete this work, and for always being open to talk to me when I faced uncertainty and challenges along the way. Thank you specifically to Shea McInnis for being such a great friend throughout this journey. I also thank my parents, Sheila Patterson, and Kenny Zinck, for your consistent support and interest in my work.

Thank you, Dalhousie University and Mount Saint Vincent University, for providing me with the facilities and classes to fulfill my degree requirements. I also thank those who have provided me with funding and support to complete my research and my degree; the Nova Scotia Graduate Scholarship Fund, the Natural Sciences and Engineering Research Council of Canada, the Killam Foundation, the Department of Medical Neuroscience, and Dr. Franz-Odendaal.

Chapter 1: Introduction

1.1 Vertebrate Cartilage

The vertebrate skeleton is composed of a combination of both cartilage and calcified bone. In general, cartilage is a connective tissue characterized by cells known as chondrocytes and a dense fibrous extracellular matrix (ECM) comprised of collagen-II and aggrecan mucopolysaccharides (DeLise et al., 2000; Gentili & Cancedda, 2009). Cartilage is found throughout the vertebrate body from early embryonic stages throughout adulthood. During this time, cartilage plays numerous roles from supporting movement in articular joints, forming permanent structures in the head and neck, and laying a foundational template of the embryonic skeleton (Hall, 2015).

In congruence with the numerous roles and localizations of cartilage from early development to adulthood, cartilage is not homogenous throughout the vertebrate body, nor is it similar between vertebrates. That is, several variations of cartilage exist throughout the body, each characterized by differences in their chondrocyte/ECM ratio and different histological traits such as enlarged lacunae (Benjamin, 1990). These include hyaline-cell cartilage, Schaffer's Zellknorpel elastic/cell-rich cartilage, fibro/cell-rich cartilage, matrix-rich hyaline cartilage, and cell-rich hyaline cartilage, to name just a few (Benjamin, 1990). Cell-rich hyaline cartilage is the most common cartilage type in zebrafish and can be found in structures such as Meckel's cartilage and the gill arches (Benjamin, 1990).

Cartilage can persist throughout life of the organism, or it can be replaced by bone in processes known as endochondral and perichondral ossification. For example, articular cartilages persist throughout an animal's lifespan, while template cartilages ossify during development and

growth of the organism. These different types of cartilages are known as permanent cartilages and replacement cartilages, respectively (Eames et al., 2004). Additionally, cartilages can also be subdivided into primary cartilages, which form early in development (e.g. Meckel's cartilage), and secondary cartilages, which form at a later timepoint (e.g. articular cartilages in joints) (Delatte et al., 2004). Differences in the adult fate of cartilage is determined via differential gene expression of key developmental genes during cartilage development.

1.1.1 Cartilage Development

The differences observed in cartilage composition throughout the body, and across taxa, are likely a result of slight alterations in developmental processes acquired throughout vertebrate evolutionary history. The earliest indication of cartilage development is the aggregation of mesenchymal cells to form a chondrogenic condensation (DeLise et al., 2000; Hall & Miyake, 2000; Giffin et al., 2019 for review on condensations). Condensation development is induced via reciprocal signaling between an epithelial layer and loose mesenchymal cells of either neural crest or mesodermal origins (Figure 1.1A) (Hall, 1981, 2015; DeLise et al., 2000). This reciprocal signaling, known as an epithelial-mesenchymal interaction (EMI), is required for both bone and cartilage development and has previously been demonstrated in the avian mandible and clavicle (Hall, 1981, 1986), as well as the cartilages of the zebrafish viscero-cranium (Walshe & Mason, 2003), and others, including the murine calvariae (Vivatbutsiri et al., 2008; Tubbs et al., 2012).

Chondrogenic condensations grow via cell migration and/or proliferation (DeLise et al., 2000; Hall & Miyake, 2000; Shimizu et al., 2007). Upon reaching a critical condensation size, the pre-chondrogenic mesenchymal cells will undergo differentiation to prechondrocytes (Figure

1.1A) (Hall & Miyake, 2000). This change is denoted by a switch of how the condensation grows from migration-driven to proliferation-driven (Shimizu et al., 2007). During this proliferative stage of development, prechondrocytes (also known as chondroblasts) will begin to express distinct cartilage markers, genes such as *COL2A1* and *SOX9 (*Figure 1.1A). Finally, throughout the proliferative growth of an early cartilage element, prechondrocytes will undergo hypertrophy and enter a non-proliferative state. During this period, a specialized extracellular matrix rich in fibrous proteins such as collagen-II, aggrecan, and other proteoglycans is secreted (Gentili & Cancedda, 2009). The presence of hypertrophic cells and dense matrix demarcates the final stage of cartilage development (Figure 1.1A). Throughout the post-natal growth of an organism, both hypertrophic and pre-hypertrophic cartilage cells can be found in the skeleton, allowing for the continued growth of cartilage element (e.g., the epiphyseal plate of long bones).

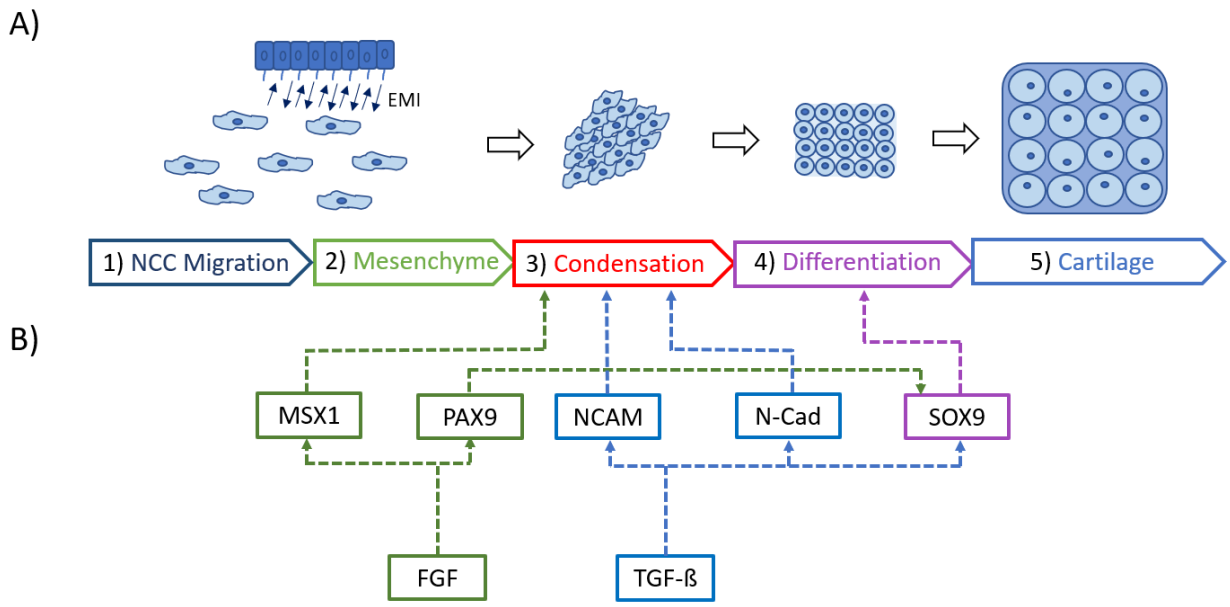

Figure 1.1. *Stages of chondrogenesis and the roles of FGF and TGF-ß signaling during early chondrogenesis. A, schematic illustrating the five stages of cartilage development. B, Highly*

simplified gene-regulatory network diagram illustrating the roles of FGF (green) and TGF-ß (blue) in the early phases of chondrogenesis (i.e. mesenchymal aggregation to form a stable condensation). GRN adapted from (Cole, 2011). Arrows between epithelium and mesenchyme (A), represent epithelial-mesenchymal interaction. Dotted lines with arrowheads (B) represent up-regulation of down stream gene expression and positive regulation of chondrogenesis stages.

Chondrogenesis requires the precise spatio-temporal orchestration of gene regulation. Several major developmental pathways, including the bone morphogenetic protein (BMP), the fibroblast growth factor (FGF), WNT/ß-catenin, and retinoic acid signaling pathways are crucial for proper cartilage development (For review, see Cole, 2011 & Li & Dong, 2016). Proper regulation of each of these foundational signaling pathways is required for the initiation and progression of chondrogenesis in vertebrates (Walshe & Mason, 2003; Retting et al., 2009; Horakova et al., 2014). As previously described, chondrogenesis proceeds via distinct development stages beginning with an EMI, followed by condensation development, and differentiation of prechondrocytes, and finally hypertrophy of chondrocytes and matrix secretion. Each of these key stages are marked by changes in gene expression, as mapped in the chondrogenesis gene regulatory network (Figure 1.1B) (Cole, 2011).

While several signaling pathways, and a myriad of genes, have been implicated in the early stages of vertebrate chondrogenesis, the specific signals and mechanisms regulating the transition from loose mesenchymal progenitors to a chondrogenic condensation are largely unknown. Research focusing on this early stage of chondrogenesis has identified a requirement for TGF-ß, FGF, and BMP signaling. Each of these pathways, when disrupted via inhibition or genetic knockdown, have produce deleterious effects on chondrogenesis (Yi et al., 2000; Walshe & Mason, 2003; Horakova et al., 2014; Lim et al., 2015; Zinck et al., 2021). Interestingly,

depending on the timing of signal inhibition, differential effects on chondrogenesis have been observed. For example, disruption of BMP signaling in the mouse and zebrafish by either chemical inhibition or genetic knockdown has provided evidence for BMP function throughout each stage of chondrogenesis (Wu et al., 2007; Retting et al., 2009; Lim et al., 2015; Li & Dong, 2016; Rajaram et al., 2017; Zinck et al., 2021). Interestingly, a vast majority of these studies have implicated down regulation of a downstream gene, SOX9, as common factor of BMP inhibition. SOX9, a master regulator of cartilage development, is required for chondrogenesis and is thought to indicate commitment to the skeletogenic fate (Lefebvre et al., 1997; Bi et al., 1999; Sekiya et al., 2000; Yan et al., 2002; Cole, 2011; Li & Dong, 2016; Lefebvre & Dvir-Ginzberg, 2017). Interestingly, research investigating SOX9 expression during chondrogenesis has also implicated a modulatory role for the TGF-ß and FGF signaling pathways.

While it is known that an EMI is required for induction of cartilage development, the signaling factors involved in this process remain unknown. Potential candidate signals include both TGF-ß and FGF signaling, as each has been shown to be required for cartilage formation in vertebrates (Figure 1.1B) (Tsonis et al., 1994; Lough et al., 1996; Walshe & Mason, 2003). In experiments investigating mesenchymal aggregation in the chick limb-bud, Tsonis et al., (1994) demonstrated that TGF-ß signaling regulates *N-Cadherin* expression in pre-condensation mesenchymal cells. *N-Cadherin* expression is downregulated following mesenchymal aggregation, illustrating its necessity for cell-cell signaling in the transition from loose mesenchyme to a prechondrogenic condensation (Figure 1.1B) (Tsonis et al., 1994). More recently, Walshe & Mason, (2003), demonstrated the requirement of FGF signaling in zebrafish chondrogenesis (Figure 1.1B). This was done via morpholino mediated knockdown of *FGF3* and *FGF8* signaling in larval zebrafish, which produced severe disruption of zebrafish head cartilage

(notably the pharyngeal and neurocranial cartilages that form by 5 days post-fertilization, each of which draw progenitor cells from the cranial neural crest). Interestingly, as a result of morpholino treatment, expression of both *FGF3* and *FGF8* was shown to be reduced in the pharyngeal endoderm and ventral forebrain, indicating that inductive FGF signaling may occur during the migration of the neural crest progenitor cells (Walshe & Mason, 2003). Thus, both the TGF-ß and FGF signaling pathways are likely involved in the early induction stages of chondrogenesis.

1.2 The Ocular Skeleton

Many vertebrate groups, including fish, reptiles, avians, as well as monotreme mammals, possess skeletal elements embedded in the sclera. These elements are the scleral cartilage and scleral ossicles, and together they form the ocular skeleton (Franz-Odendaal & Vickaryous, 2006; Franz-Odendaal, 2011, 2018). In most fish taxa, the scleral cartilage develops in a ring-like shape around the equator of the eye, while later in growth one to two scleral ossicles will develop via periskeletal ossification in resorbed sections of the scleral cartilage ring (Franz-Odendaal & Vickaryous, 2006; Franz-Odendaal et al., 2007). Periskeletal ossification is an unusual form of ossification that has only been described in the teleost ocular skeleton and will be discussed later. In contrast to fish, reptilian and avian scleral cartilage develops in a cup-like shape, encompassing much of the eye (Franz-Odendaal & Vickaryous, 2006; Franz-Odendaal, 2018). The scleral ossicles of these animals form near the anterior portion of this cup-like scleral cartilage (Franz-Odendaal & Vickaryous, 2006; Franz-Odendaal, 2008b; Atkins & Franz-Odendaal, 2016). However, unlike in fish, reptilian and avian scleral ossicles form directly in a process known as intramembranous ossification. Moreover, development of the reptilian and avian scleral ossicles occurs during embryonic development, while ossification of teleost scleral

ossicles occurs much later in life (Cubbage & Mabee, 1996; Franz-Odendaal, 2008b). Thus, while it is unlikely that the scleral ossicles are evolutionarily homologous structures between fish and other vertebrates, it is possible that the scleral cartilage is an evolutionarily and developmentally homologous structure (Franz-Odendaal & Hall, 2006; Franz-Odendaal & Vickaryous, 2006). For the purpose of this thesis, I will focus on the ring-like scleral cartilage of teleost fish.

While scleral cartilage typically exists as a ring in teleost fish, it can vary morphologically among teleosts. The most apparent difference in scleral cartilage morphology across teleost taxa is the extent to which the scleral cartilage extends towards the back of the eyeball. Thus some teleost species have a scleral cartilage element resembling a narrow ring while others have a SC element that extends deeper to form a cup-like structure (Franz-Odendaal & Hall, 2006; Dufton, 2013; O'Quin et al., 2015). The depth of the scleral cartilage ring is the only morphological difference among teleost scleral cartilages known to date, although no large-scale analysis has been conducted to examine this further. Interestingly, the differences in scleral ossicle morphology in fish has been found to be associated with different lifestyles and habitats (Franz-Odendaal, 2008a, 2018; Kindl & O'Quin, 2019). Similarly, it is possible that the increased mechanical strength provided by a deep cartilage is advantageous in deeper, benthic habitats, while a lighter, narrowing ring, is advantageous in pelagic habitats where speed elicits ossification of the cartilage. However, this topic has not yet been studied with respect to scleral cartilage.

The zebrafish, or *Danio rerio*, is a small teleost found in streams throughout south-east Asia. In recent decades the organism has proven invaluable to the study of vertebrate development. Zebrafish have become heavily utilized as a developmental model due to a number

of practical factors including large clutch size, as well as rapid and transparent development (Veldman & Lin, 2008). In addition to development, zebrafish are key model organisms in the study of behaviour, disease, and pharmacology (Veldman & Lin, 2008; Yin et al., 2011; Sanvitale et al., 2013; De Smet et al., 2014; Nassar et al., 2014). Of particular interest to this project is the development of the skeleton, which has been well documented in terms of development and morphology (Benjamin, 1990; Cubbage & Mabee, 1996; Bird & Mabee, 2003; Franz-Odendaal et al., 2007; Parichy et al., 2011). The zebrafish scleral cartilage has previously been described as a narrow ring of cell-rich hyaline cartilage encompassing the equator of the eye, which later gives rise to scleral ossicles at rostral and caudal points in the ring. Interestingly, the scleral ossicle themselves extend past the posterior boundary of the scleral cartilage (Figure 1.2A; Franz-Odendaal et al., 2007).

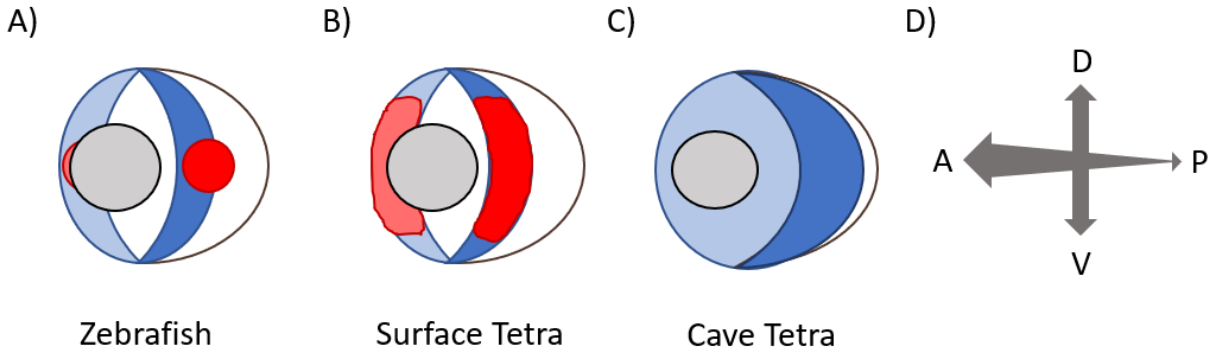

Figure 1.2. *Schematic of teleost ocular skeleton morphologies view anterio-laterally. A, schematic of zebrafish ocular skeleton. B, Schematic of surface tetra ocular skeleton. C, Schematic of cave tetra ocular skeleton. D, Schematics illustrating the orientation in which the eyes (A-C) are viewed. Blue represents scleral cartilage. Red represents scleral ossicles. Grey represents the lens.*

Astyanax mexicanus, or the Mexican tetra, exists in nature as two morphs with strikingly different morphologies: a pigmented surface morph with large, functional eyes, and an albino cave morph with highly reduced eyes (Torres-Paz et al., 2018). Of note, the divergent evolution responsible for the cave morph has occurred at least thirty times over approximately 20,000 years, indicated by thirty genetically different populations in unconnected caves across Mexico and the southern United States (Torres-Paz et al., 2018). Interestingly, slight variations in pigmentation and eye morphology exist across the cavefish populations, although they have all converged on troglomorphic phenotypes typical of cave-inhabiting animals (pigment and eye reduction) (Jeffery et al., 2003). *A. mexicanus* has been used as a model to study eye development, and in recent years research on the mechanisms responsible for eye degeneration in the cavefish have elucidated the role of the lens in leading this eye degeneration (Jeffery et al.,

2003; Protas et al., 2007; Borowsky, 2008; McGaugh et al., 2014). Interestingly, SC morphology also differs between the two morphs of *A. mexicanus* (Jeffery, 2001, Fig 3(I); Dufton, Hall, & Franz-Odendaal, 2012, Fig 7(F)). The surface morph possesses a ring of scleral cartilage typical of other teleosts such as the zebrafish (Figure 1.2B; Franz-Odendaal et al., 2007). In contrast, the reduced eye of the Pachón cave morph is encapsulated by SC that extends towards the posterior of the eye, much like the deep cup of cartilage found in many benthic fish (Figure 1.2C; Jeffery, 2001; Franz-Odendaal & Hall, 2006; Dufton et al., 2012). In comparison to the zebrafish, the scleral ossicles of the surface tetra ossify over a much wider portion of the scleral cartilage ring, and do not extend past the posterior scleral cartilage boundary. Interestingly, only a handful of cave tetra populations develop scleral ossicles. In these fish (namely the Tinaja population), the entire scleral cartilage ring ossifies (Kindl & O'Quin, 2019). The difference in SC morphology within two morphs of the same species provides an ideal system for investigating the differences in morphological regulation leading to each phenotype, while examination of the more phylogenetically distant zebrafish (Franz-Odendaal, 2008a) will allow for an understanding of how differences may have arisen over evolutionary time.

Little is currently known about scleral cartilage development. This is especially true for teleost scleral cartilage, which historically, has received relatively little attention from researchers compared to avian scleral cartilage development (Newsome, 1972; Stewart & McCallion, 1975; Hall, 1981; Thompson et al., 2010). More recently, and likely due to the widespread adoption of teleosts as model organisms (e.g., zebrafish, Mexican tetra, medaka, etc.), some research groups have focused their attention on teleost ocular skeleton development and morphology. However, the majority of this research has focused on scleral ossicle

development and morphology, with lesser attention given to the scleral cartilage (Franz-Odendaal & Hall, 2006; Franz-Odendaal et al., 2007; Kindl & O'Quin, 2019).

While few studies have closely examined the scleral cartilage, a few key findings have been made to date. Histology has revealed that zebrafish scleral cartilage bares greatest resemblance to cell-rich hyaline cartilage (Benjamin, 1990; Franz-Odendaal et al., 2007). By examining a transgenic zebrafish with *sox10*-dependent GFP expression, Kague et al., (2012) determined that zebrafish scleral cartilage is a derivative of cranial neural crest cells in the periocular mesenchyme (POM), similar to many other cranial cartilages in the zebrafish (Williams & Bohnsack, 2020). In research describing the initial appearance of skeletal elements in the zebrafish, Cubbage & Mabee, (1996) observed the zebrafish scleral ossicles at 8.0 and 9.4 mm standard length (SL) (for the anterior ossicle and posterior ossicle respectively). However, the timing of the appearance of scleral cartilage was not noted. Recent research from the Franz-Odendaal lab confirmed the earliest presence of zebrafish scleral cartilage at approximately 4.1 mm SL (Zinck et al., 2021). No other details of scleral cartilage development in teleosts are known, which leaves many gaps left to be filled, such as the identity of the epithelium involved in the scleral cartilage EMI, as well as the signaling molecules involved in its induction. The tissues and molecules involved are highly likely to be associated with the eye, given that the SC is situated adjacent to the retina in the sclera.

1.3 Eye Development

The vertebrate eye, a structure with both a complex morphology and development, has been described thoroughly in the mouse, chicken, and zebrafish, leading to the discoveries of various developmental differences between these models. This section will provide a detailed overview of general vertebrate eye development, and will then identify significant differences

between mouse, chicken, and zebrafish eye development, with the goal of describing the tissue environment in which the scleral cartilage develops.

1.3.1 Optic Cup Morphogenesis

The vertebrate eye forms as an out pocketing of the diencephalon (forebrain). As such, vertebrate eye development begins in the anterior neural ectoderm (England et al., 2006). During the early stages of neurulation, inductive signaling specifies a region of anterior neural plate ectoderm fated to become the optic field. As the anterior neural plate folds to form the neural tube, the eye field separates bilaterally into two distinct fields. These eye fields evaginate laterally, forming the optic vesicles (England et al., 2006; Kwan et al., 2012; Cavodeassi, 2018). Evagination of the optic vesicle takes place by 12 hours post-fertilization (hpf) in zebrafish, compared to embryonic day (E) 9.5 in mice, and HH10 (E1) in chicken (Johnston et al., 1979; Kwan et al., 2012; Chauhan et al., 2015).

Following evagination of the early forebrain to form the bilateral optic vesicles, the invagination stage occurs. In this stage, simultaneous development of the lens and invagination of the optic cup takes place. In both the mouse and chicken, the lens develops via invagination of a thickened surface ectoderm (the lens placode) superior to the primordial eye. That is, in the mouse and chicken, the presumptive lens and optic vesicle invaginate simultaneously (Fuhrmann, 2010). In contrast, in the zebrafish, the lens develops via delamination of cells from the surface ectoderm (Li et al., 2000). In each of the animals described the invagination stage of optic cup morphogenesis is finalized by the presence of bilateral optic cups paired with lenses and with subsequent development of an overlying cornea.

1.3.2 Establishment of the retinal pigment epithelium and neural retina.

During optic cup morphogenesis, two distinct layers of the future retina are established: the retinal pigment epithelium (RPE) and the neural retina (NR). In the early stages of invagination, the future RPE and NR are established in different regions of the optic cup. In the anterior layer (or the invaginating layer closest to the surface ectoderm), the future NR is established. In the posterior layer (closest to the forebrain) the future RPE is established (Strauss, 2005; Fuhrmann, 2010). While the tissues differ in function and morphology, both the development and functionality of the RPE and NR are interdependent from the earliest stages of their differentiation.

1.3.2.1 Retinal pigment epithelium development and function

Prior to differentiation, RPE precursors of the neural epithelium are ciliated cuboidal cells, with their apical side facing the lumen of the optic vesicle (Bok, 1993). As optic cup morphogenesis continues, the space separating the presumptive RPE and NR decreases, allowing for closer interaction of these epithelial layers. At this point, the space becomes filled with a specialized matrix to facilitate communication between the differentiating RPE and NR; the interphotoreceptor matrix (Gonzalez-Fernandez & Healy, 1990).

Upon the establishment of communication between the RPE and NR in zebrafish, overt differentiation takes places. The initiation of RPE differentiation is denoted by morphological changes in RPE cells. Namely, the cuboidal cells of the RPE flatten and widen, forming a squamous epithelium. This process occurs from approximately 16-24 hpf in the zebrafish (Li et al., 2000). During this time, differential expression of various transcription factors by the RPE and NR can be observed. For example expression of OTX2 (homeodomain-containing

transcription factor) and MITFA (microphthalmia-associated transcription factor) can be observed in the RPE of zebrafish; two genes involved in patterning and function of the tissue (Fuhrmann, 2010; Martínez-Morales et al., 2003). In contrast the expression of CRBP (cellular retinol binding protein), and CRABP (cellular retinaldehyde binding protein) can be observed in the developing NR; two genes involved in the retinal synthesis pathway (Martínez-Morales et al., 2003).

While the RPE is specified early in optic cup morphogenesis, its differentiation extends much later into embryonic/larval development as denoted by its gradual pigmentation. In the chicken, RPE pigmentation occurs in two distinct phases with differences in melanin synthesis rates indicated by tyrosinase enzyme activity (Stroeva & Mitashov, 1983). Early (low-rate) pigmentation occurs between Hamburger-Hamilton (HH) stages 18-25 (E3-E5), and a second, more robust (high-rate) pigmentation phase occurring between HH stages 26-39 (E5-E13) (Stroeva & Mitashov, 1983). In the zebrafish, RPE pigmentation is initiated at approximately 24-hpf, shortly after the transition from cuboidal cells to squamous cells (Lister, 2002). A terminal stage of pigment accumulation is not well described in the literature for zebrafish, but gradual changes in pigmentation indicate that RPE development occurs much later (i.e. over a few days) into larval development (Li et al., 2000; Lister, 2002). Thus, it appears that RPE development is not a rapid process in vertebrates, extending over a number of embryonic/larval stages.

1.3.3 Closure of the optic fissure

The final stage of optic cup morphogenesis is denoted by closure of the optic fissure. The optic fissure is a gap in the ventral region of the optic cup formed during invagination of the optic vesicle. In order to form the sphere-like structure of the adult eye, the ventral optic cup

tissues must meet and fuse. Closure of the optic fissure is a highly complex process that involves restructuring of both the ventral RPE and NR (Li et al., 2000; Kwan et al., 2012; Cavodeassi, 2018). Failure of this process can lead to a morphological defect known as ocular coloboma, in which a gap in the neural ectoderm-derived tissues of the optic cup (i.e. the RPE and NR) remains throughout adult life (Take-uchi et al., 2003; Brown et al., 2009; Fuhrmann, 2010; Gestri et al., 2012).

Knockdown studies in the zebrafish have implicated a few key genes involved in optic fissure closure. In treating zebrafish embryos with morpholinos, Take-uchi et al., (2003), demonstrated the requirement of *VAX1* and *VAX2* expression for closure of the optic fissure. Interestingly, simultaneous knockdown of *VAX1* and *VAX2* resulted in a more severe coloboma (i.e. a larger gap) than a single knockdown of either gene (Take-uchi et al., 2003). More recently, researchers have illustrated similar effects via knockdown or knockout of other genes such as *NLZ1*, *NLZ2*, *PAX2*, and *PAX6* (Brown et al., 2009; Dutta et al., 2015). Thus, the ability to induce disruption of the optic fissure may prove to be a useful tool in studying the role of the RPE in other developmental systems involving the eye, such as the scleral cartilage.

1.3.4 Contributions of the periocular mesenchyme: the sclera and scleral cartilage

While the optic cup eventually forms the NR and RPE, the cells of the sclera are derived from the POM. In addition to the sclera, the POM is responsible for the anterior segment of the eye, including the iris and ciliary body (Coulombre, 1961; Williams & Bohnsack, 2020). In the chicken, the POM is derived from a mixture of cranial NCC and lateral plate mesoderm (Coulombre, 1961). The same is likely true for teleost fish like the zebrafish. However, while zebrafish POM has been shown to possess mesenchyme from the cranial neural crest cells via a

SOX10 transgenic line (Kague et al., 2012; Van Der Meulen et al., 2020), no studies have explicitly demonstrated the presence of mesoderm.

Scleral development occurs during optic cup morphogenesis and is first indicated by aggregations of POM around the developing optic cup (Coulombre, 1961). These aggregating cells will later differentiate into fibroblasts and chondrocytes, and provide the eye with robust support via a rich collagen matrix (Coulombre, 1961; Johnston et al., 1979; Park et al., 2016). As previously discussed, in vertebrates such as fish and reptiles, the sclera houses both bony and cartilaginous skeletal elements known as the ocular skeleton (Franz-Odendaal & Vickaryous, 2006; Franz-Odendaal et al., 2007; Franz-Odendaal, 2018). Similarly to the sclera, the ocular skeleton (i.e. the scleral ossicles and scleral cartilage) is derived from the POM in both chicken and zebrafish; the two organisms in which the ocular skeleton has been fate mapped (Stewart & McCallion, 1975;Couly et al., 1993; Kague et al., 2012; Franz-Odendaal, 2018; Williams & Bohnsack, 2020)

1.4 A potential role for the retinal pigment epithelium in scleral cartilage development

As previously described, little is known about scleral cartilage development. What little knowledge exists regarding scleral cartilage development has been generated from research utilizing the chicken and zebrafish as model organisms (with an emphasis on the chicken, historically) (Newsome, 1972; Stewart & McCallion, 1975; Hall, 1981; Franz-Odendaal & Vickaryous, 2006; Franz-Odendaal et al., 2007; Thompson et al., 2010; Zinck et al., 2021).

Cartilage development requires initiation via an epithelial-mesenchymal interaction. While it is clear that scleral cartilage is derived from POM progenitors (Newsome, 1972; Stewart & McCallion, 1975; Kague et al., 2012), the identity of the inducing epithelium, and the signals

involved, remain unknown. Research to understand the chicken scleral cartilage development has provided some evidence for RPE involvement in scleral cartilage induction (Newsome, 1972; Stewart & McCallion, 1975; Thompson et al., 2010). In a series of grafting experiments, Newsome (1972), demonstrated that RPE donated from HH25 chicken embryos could induce chondrogenesis in HH17 and HH18 (~E3) POM, but not in HH19, HH20, or HH23 (E4) mesenchyme. Subsequent experiments in which HH25 RPE and HH17/18 POM was individually grafted to the chorioallantoic membrane did not result in cartilage induction. Thus, they concluded that communication between the RPE and the mesenchyme is time dependent for RPE-induced chondrogenesis (Newsome, 1972). That is, the mesenchyme is only competent to respond for a short period in chickens, prior to a fate-restriction event at approximately HH19. More recently, Thompson et al., (2010) demonstrate that enucleation of the chicken eye (removal of the optic cup, and thus, the developing NR and RPE) at HH12 to HH14 prevented scleral cartilage induction. In additional graft experiments, Thompson et al., (2010) demonstrated that pairing HH18 or HH19 RPE with cranial mesenchyme temporal to the eye of equivalent age (which does not normally generate cartilage *in vivo*), resulted in generation of small cartilage nodules directly below the grafted RPE. In order to determine if RPE grafts could rescue scleral cartilage development following enucleation, the researchers grafted HH18/19 RPE into the cavity left by enucleation in HH12-14 chick embryos. Interestingly, this resulted in cartilage induction in the mesenchyme surround the graft. Similar grafts utilizing NR instead of RPE did not result in cartilage induction (Thompson et al., 2010). While these experiments provide strong evidence for involvement of the RPE in scleral cartilage induction in the chicken, they are potentially flawed. That is, Thompson et al. (2010), demonstrated *in vivo* expression of markers of pre-committed cartilage *(*namely, *CART1* and *SOX9*) in the POM adjacent to the RPE

beginning at HH18. However, *in vivo Aggrecan* expression (which indicates the initiation of cartilage differentiation) was not noted until HH26. In their grafting experiments, Thompson et al. (2010), grafted HH18 and HH19 RPE to head mesenchyme, eliciting expression of the genes mentioned above, and later, cartilage development. However, at this timepoint the RPE is still in an early phase of its development and thus has likely not undergone a reduction of its inductive potential (Hall, 1981; Stroeva & Mitashov, 1983; Muller et al., 2007). Furthermore, cranial neural crest cells are competent to form cartilage under the right signals (Hall & Tremaine, 1979; Ekanayake & Tuan, 1994; Yang et al., 2021), thus it is unsurprising that signaling from an immature epithelium early in the process of differentiation was able to induce chondrogenesis. Therefore, while this study concluded a role of the RPE in scleral cartilage induction, the interpretations of these experiments might have been misinterpreted or exaggerated, as note above.

1.5 Objectives and Hypotheses

Research Objective: To understand the development and morphology of scleral cartilage in teleosts.

Sub-Objective 1: To determine the pattern of scleral cartilage induction and growth in teleosts with different scleral cartilage morphology, namely the surface and Pachón cave morphs of the Mexican tetra (*Astyanax mexicanus*), and the zebrafish *(Danio rerio*).

> **Hypothesis 1a:** I hypothesize that scleral cartilage induction (followed by cartilage differentiation) will <u>first</u> occur in the sclera near the anterior most extent of the optic cup tissues (ora serrata) because this is the location of the SC in fish with narrow rings.

Hypothesis 1b: Following on from hypothesis 1a, I hypothesize that in species with deeper scleral cartilage rings, that growth will continue in the posterior direction (towards the back of the eye) and that in species with narrow scleral cartilage rings, growth will be halted after chondrogenesis has occurred.

Sub-Objective 2: To investigate the involvement of the RPE in scleral cartilage induction and morphogenesis.

Hypothesis 2: I hypothesize that scleral cartilage morphology will be altered in CRISPR-zebrafish with disrupted RPE development.

Sub-Objective 3: To determine the role of FGFs and TGF-B in scleral cartilage development.

Hypothesis 3a: I hypothesize that local inhibition of the FGFRs or TGF-B receptors will lead to disruption of scleral cartilage morphology.

The following chapters of this thesis will focus on a descriptive analysis of scleral cartilage morphology and growth in the surface tetra, cave tetra, and zebrafish (Chapter 2) and injection experiments aimed to disrupt TGF-ß and FGF signaling in the zebrafish eye at the hypothesized time of scleral cartilage induction (Chapter 3). The results of each of these sections will be discussed at the conclusion of their respective chapters. The combined results obtained in Chapter 2 and Chapter 3 will be further discussed in Chapter 4, with regard to the overall research objective and how the results align with the RPE-induction hypothesis proposed in past research utilizing the chicken. A short Chapter focusing on the progress made towards Sub-Objective 2 can be found in Appendix A.

Chapter 2: Histological Analysis of Teleost Scleral Cartilage

2.1 Introduction

Very little is known about teleost scleral cartilage development. As previously mentioned, teleost scleral cartilage typically appears around the equator of the eye as a narrow ring of hyaline cartilage (Franz-Odendaal & Vickaryous, 2006; Franz-Odendaal et al., 2007). Previous descriptions also indicate variation in the extent to which the scleral cartilage extends towards the back of the eye (i.e. the scleral cartilage depth), across teleost groups (Franz-Odendaal et al., 2007). As such, the research presented in this chapter aims to determine the pattern of scleral cartilage development and growth in teleosts with different scleral cartilage morphology, namely the Mexican tetra (*Astyanax mexicanus*) surface and Pachón cave morphs, and the zebrafish (*Danio rerio*). I hypothesize that SC development (followed by cartilage differentiation) will first occur in the sclera near the anterior most extent of the optic cup tissues (ora serrata). Secondly, I hypothesize that in fish with deeper scleral cartilage rings, that growth will continue in the posterior direction (towards the back of the eye) and that in species with narrow scleral cartilage rings, growth will be halted when the scleral cartilage has reached its maximum depth. Alternatively, it is possible that in fish with deeper scleral cartilage, the cartilage could emerge (or develop) synchronously over the entire spatial distribution of the sclera (i.e., lining the entire RPE). However, such a mechanism would be unexpected since cartilage elements typically emerge as small anlage (from chondrogenic condensations), followed by growth via pre-chondrocyte proliferation (Kimmel et al., 1998; Shimizu et al., 2007).

In order to test these hypotheses, the scleral cartilage of a developmental series of surface tetras, cave tetras, and zebrafish was analyzed via histological sections. Specifically, coronal sections were stained using the Hall-Brunt Quadruple (HBQ) method (Brian K Hall, 1986), to allow for visualization of scleral cartilage depth. HBQ staining utilizes four histological stains in order to clearly visualize cartilage (Alcian Blue), mineralised bone and collagen rich tissues (Direct Red), along with the cytoplasm and nuclei of other cell types. Thus, the HBQ staining method provides an ideal way to visualize teleost scleral cartilage during its development and will allow for a detailed analysis of scleral cartilage depth and morphology.

This chapter is organized as follows: First, comparisons between the surface tetra, cave tetra, and zebrafish, in terms of eye size, scleral cartilage depth, and scleral cartilage cell-count at multiple timepoints and standard lengths are presented. This is followed by an examination of the positioning of the scleral cartilage with regard to the optic cup tissues. Finally, comparisons between each type of fish in terms of scleral cartilage positioning, namely in the rostral and caudal regions, are presented. The chapter is concluded with a discussion of the descriptive results.

2.2 Methods

2.2.1 Husbandry

AB strain zebrafish (*D. rerio*) were provided from the Dalhousie Zebrafish Core Facility at Dalhousie University, Halifax, Nova Scotia. All processes involving zebrafish outlined below were approved by the SMU-MSVU Animal Care Committee under protocol #20-20A2. Fish were obtained on the day of fertilization and reared at Mount Saint Vincent University. Between 10-20 zebrafish were housed in glass cups containing approximately 300 mL of conditioned

water maintained at 28°C via an external submersible heating unit. Water changes were performed daily of approximately 25% volume. Larvae were fed Gemma 75 following hatching (5 days post-fertilization). Once larvae were able to consume coarser grained food, they were fed Gemma 150.

Surface and Pachón variants of Mexican tetra (A. mexicanus) were provided from the Stowers Institute Cave Fish Facility, Kansas City, Missouri. All processes involving tetras outlined below were approved by the SMU-MSVU Animal Care Committee under protocol #20-20A2. Upon arrival at Mount Saint Vincent University, the tetras were transferred to glass cups containing approximately 300 mL of conditioned water maintained at 21°C. Approximately 10-20 fish were kept in each cup. Larvae were fed Gemma 75 following hatching, and Gemma 150 once they were able to consume coarser grained food.

2.2.2 Sample Collection and Tissue Fixation

In order to generate a developmental series of surface tetras, cave tetras, and zebrafish, samples of each fish were collected at 10-, 15-, 20-, and 30-days post fertilization (dpf). At these time points, fish were euthanized via submersion in 0.1% MS-222 and their standard lengths were recorded. Standard length, or SL, is the standard method to evaluate growth of fish since stocking densities can affect their growth rate. Following euthanization, the fish were submersed in 4% paraformaldehyde overnight at 4°C for tissue fixation. On the following day, samples were rinsed three times in phosphate-buffered saline (PBS). Samples were stored short-term (less than a week) in 1X PBS at 4°C.

2.2.3 Agarose Pre-embedding

In order to allow for precise control of the orientation of the fish for histological analyses, fish samples were embedded in 1% agarose prior to wax embedding. Agarose was dissolved with heat in a beaker containing distilled water. Once the beaker was able to be handled (after approximately 2-4 minutes after removal from heat), a small amount was poured into a plastic petri dish to reach a depth of approximately 4 mm. Fish were then placed in the molten agarose as it cooled. Using metal forceps, the fish were oriented ventral side down before the agarose solidified. Additional finer adjustments were made to ensure that the eyes of individual fish settled on a level plane, allowing for even coronal sections. Once the agarose gel had set (after approximately 15 minutes), the fish were cut-out from the agarose in small blocks. Agarose blocks were then immediately submerged in 25% ethanol and dehydrated as outlined in Section 2.2.4 below.

Fish collected at 30-dpf were decalcified via submersion in 10% ethylenediamine tetra-acetic acid (EDTA) overnight and rinsed with PBS prior to agarose pre-embedding. Fish of other age groups were not decalcified. For the full agarose-embedding protocol see Appendix E.

2.2.4 Paraffin Wax Embedding

In preparation for wax embedding, agarose-embedded samples were dehydrated to 100% ethanol via a series of 25%, 50%, 70% 90%, 95% and 100% ethanol. Following dehydration, samples were incubated in Citrisolv (Fisher Scientific 22-143975) for two one-hour periods. Samples were then blotted dry on a kimwipe and transferred to a preheated metal mould containing molten paraffin wax (McCormick 39503002) using preheated forceps. Moulds were then transferred to a vacuum oven (Napco Model 5831) and incubated at 58°C and 15 mmHg for

two hours. The used wax was discarded, and the samples were incubated with fresh molten wax overnight at 58°C and 15 mmHg. The following day, the used wax was discarded again, replaced with fresh molten wax, and the samples were embedded by freezing on an ice pack. During embedding, samples were adjusted using pre-heated forceps to ensure proper orientation for coronal sectioning. Once secured in position, a plastic wax block holder was placed on top of the metal mould, which was then filled with wax. The embedded samples were then transfer to a freezer at -20°C where they hardened overnight. Samples were stored at -20°C until needed. For the full wax embedding protocol see Appendix E.

2.2.5 Tissue Sectioning

Frozen wax blocks were retrieved from the -20°C freezer and the metal moulds were removed. Excess wax was trimmed away from the samples using a razorblade. Samples were sectioned at a thickness of 6 µm using a Leitz 1512 microtome. Using a paint brush, sections were then transferred to glass slides which were covered in small pools of warmed water. Two ribbons of five to ten consecutive sections were placed on each slide. Section ribbons were adjusted using paint brush and excess water was removed using Kimwipe. Slides were then incubated overnight at 37°C in order to remove any remaining moisture. For a full procedure see Appendix E.

2.2.6 Hall-Brunt Quadruple Staining

In order to visualize skeletal elements, sections of 10-, 15-, 20-, and 30-dpf fish were stained using the Hall-Brunt Quadruple method (Hall, 1981). Slides containing sections of the eye were selected and placed in a metal staining rack. To dissolve the paraffin wax, the rack was then placed in Citrisolv for two five-minute periods. The sections were then rehydrated via an

ethanol dilution series consisting of 100%, 90%, 70% and 50% ethanol. The slide rack was placed in each of these solutions for one minute each, then transferred to distilled water for two minutes. Slides were then processed through a series of stains consisting of Celestine Blue for five minutes, Mayer's Haematoxylin for five minutes, Alcian Blue for five minutes, Phosphomolybdic acid for one minute, and Direct Red for five minutes. Slides were rinsed in distilled water between each of the staining steps. Following staining, the slides were briefly rinsed in 100% ethanol and washed in Citrisolv for four one-minute periods. Cover slips were applied to slides with DPX mountant (Sigma 44581) and placed on metal trays to dry in a fume hood overnight. For the full staining procedure see Appendix E.

2.2.7 Imaging and Measurements

In order to compare the scleral cartilage of surface tetras, cave tetras, and zebrafish, measurements were made based on prominent anatomical landmarks. Imaging was conducted using a Nikon SMZ1500 microscope equipped with a Nikon DS Fi2 camera. Image analysis was performed using Nikon NIS software. Length measurements were obtained using the line measurement function and cell area was obtained using the area function of the NIS software. Eye measurements were developed that utilize anatomical landmarks that are present in all fish samples regardless of age and species (Figure 2.1A). Eye width was determined by measuring the length between the anterior-lateral junction of the photoreceptor cell layer and retinal pigment epithelium (or the ora serrata). Eye depth was measured as the length between the halfway point on the width line and the most posterior of the photoreceptor cell layer (the depth line was positioned to meet the width line at a 90° angle). Scleral cartilage depth was measured as the length between the anterior and posterior edges of the scleral cartilage.

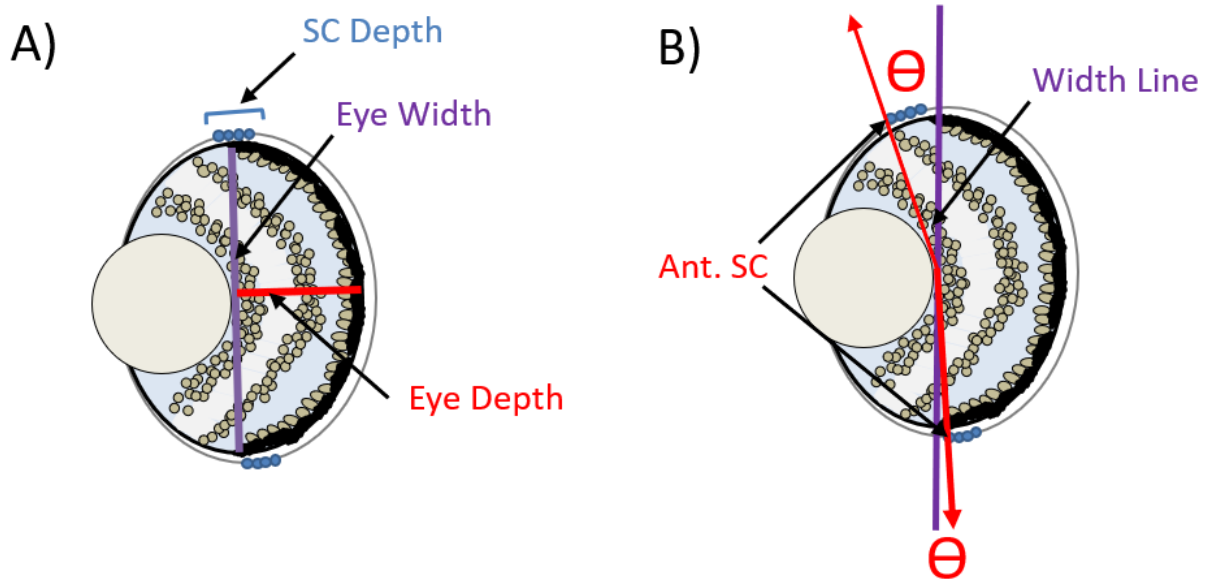

Figure 2.1. *Schematics illustrating histological measurement methodology. A, Schematic illustrating how eye width (purple line), eye depth (red line), and scleral cartilage depth (blue bracket line), were measured. B, schematic illustrating how scleral cartilage offset angles were measured between the width line (purple line) and the anterior aspect of the scleral cartilage (red, Ant. SC arrows). Red theta indicates measured angle (B).*

The number of chondrocytes in both the rostral and caudal portions of the scleral cartilage ring were counted manually in each section (only cells with clearly defined nuclei and/or clearly defined boundaries were counted). In addition, the angle between the width line and the anterior aspect of the rostral and caudal portions of the scleral cartilage was recorded for 30-dpf fish to generate a better understanding the ring's orientation about the eye (Figure 2.1B). The cross-sectional area of scleral cartilage chondrocytes was also measured in 15-, 20-, and 30-dpf samples of each tetra morph in order to better understand the differences in scleral cartilage morphology between the surface fish and cave fish (this was not performed at 10-dpf due to a

lack of scleral cartilage in fish at this age). Since chondrocyte cell size appeared to differ in the tetra morphs, the area of cell bodies in the retinal ganglion cell layer were also measured in order to compare to the chondrocyte sizes so that a better understanding of cell-size differences between the tetra morphs could be obtained. Lastly, the angle of the anterior aspect of the scleral cartilage with respect to the eye-width line was measured using the Nikon Imaging Software for both the rostral and caudal portions of the scleral cartilage ring.

In total, n=25 surface tetras (10-dpf, n=8; 15-dpf, n=7; 20-dpf, n=7; 30-dpf, n=3), n=19 cave tetras (10-dpf, n=8; 15-dpf, n=3 20-dpf, n=6; 30-dpf, n=2), and n=25 zebrafish (10-dpf, n=6; 15-dpf, n=7; 20-dpf, n=7; 30-dpf, n=5) were measured. For each individual eye, measurements (eye depth, eye width, scleral cartilage depth, cell-counts, and scleral cartilage angle) were taken on three consecutive sections at the widest portion of the eye. The three measurements were then averaged, to provide a single average measurement for each eye (e.g., scleral cartilage depth for an individual eye is the average of scleral cartilage depth at three consecutive sections). Cross-sectional area measurements of chondrocytes (and ganglion cells, defined as the layer of cells closest to the lens) were conducted on one section per individual eye (i.e., the widest section of the eye) using the area measurement feature in NIS elements. Thus, data points for cross-sectional area represent the area of individual cells.

Statistical analyses were conducted using the analysis function of the PRISM GraphPad software. Specifically, one-way analysis of variance (ANOVA) with *post-hoc* Tukey tests were used to assess differences in the mean measurements at each developmental timepoint. Statistical significance was considered at a p-value less than 0.05. Specific p-values are listed in the Results section below.

2.3 Results

2.3.1 Cave tetra eye size remains constant between 10-dpf and 30-dpf unlike surface tetra and zebrafish eye size, which increase linearly.

In order to generate an understanding of how eye size differs between the surface tetra, cave tetra, and zebrafish, the mean eye width and eye depth were compared between fish at 10-, 15-, 20-, and 30-dpf (Figure 2.2). The data shown in Figure 2.2A shows that the surface tetra and zebrafish occupy the same morphospace with respect to eye-size and display a similar, linear increase in eye size over time. However, the cave tetra occupies a unique eye-size morphospace at the lower end of the scale, regardless of age. Graphing the width and depth data across age groups further illustrates the differences in eye size between the sighted fish and cavefish. Specifically, the surface tetra and zebrafish have similar eye depth at each time point examined, which gradually increases between each timepoint (Figure 2.2B, C). In contrast, both the eye width and eye depth of the cave tetra remains constant across each timepoint examined (Figure 2.2B, C). A one-way ANOVA with *post-hoc* Tukey tests indicated significant differences in both eye depth and eye width at each timepoint between sighted fish (surface tetra and zebrafish) and the cave tetra ($p<0.0001$ at all timepoints; Figure 2.2B, C). Despite having similarly sized eyes at most timepoints, there is a statistically significant difference in both eye depth ($p<0.0001$) and eye width ($p<0.0001$) at the 20-dpf timepoint between zebrafish and surface tetras. Specifically, zebrafish have slightly larger eyes than surface tetras with a mean difference of 32.96 μm in depth, and 47.13 μm in width (Figure 2.2B, C). When eye width and eye depth were compared in terms of standard length, similar results were found (Appendix B). The measurements and mean values are given in Appendix C and the p-values for each comparison can be found in Appendix D.

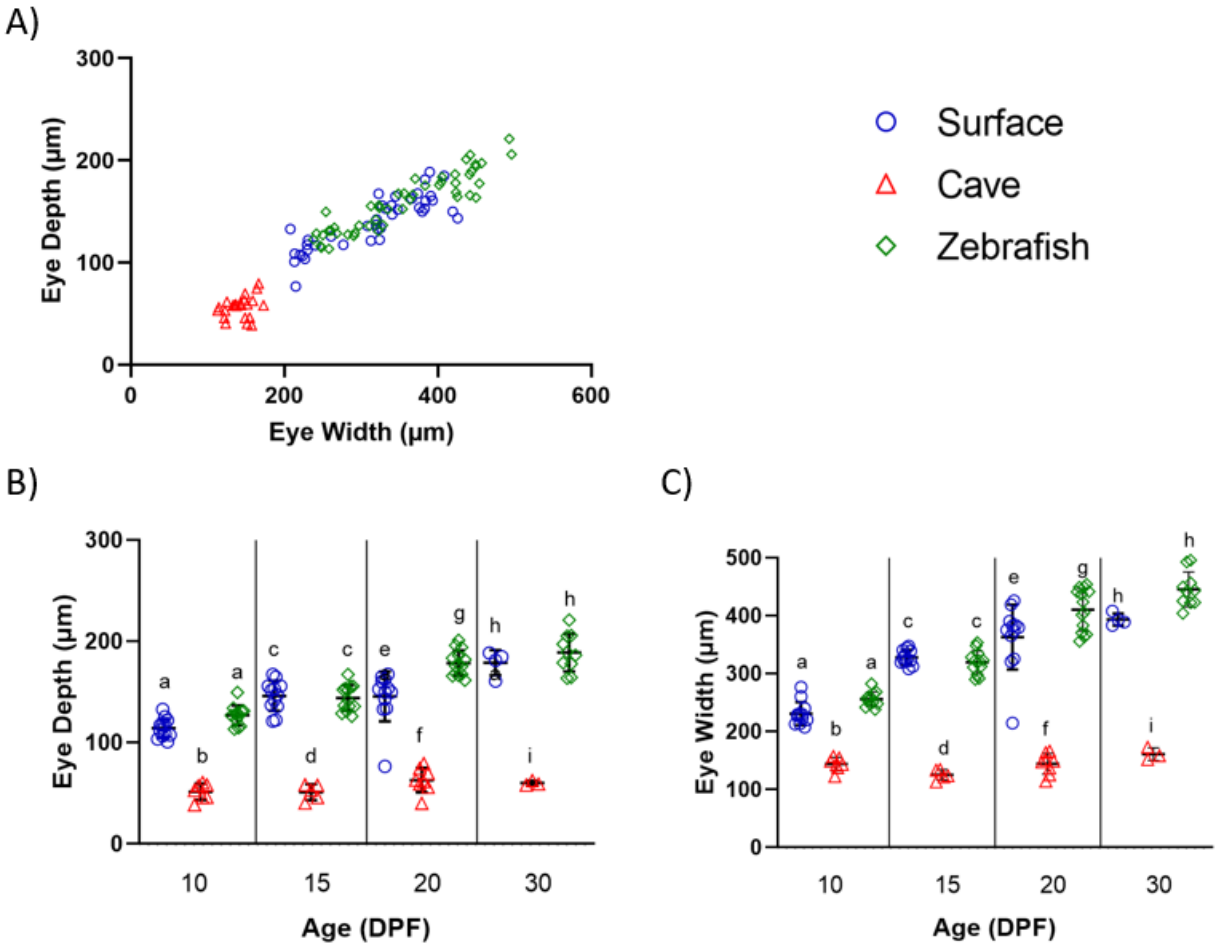

Figure 2.2. *Comparison of eye width and eye depth among surface tetra, cave tetra, and zebrafish at 10-, 15-, 20-, and 30-dpf. A, scatterplot illustrating eye depth vs. eye width for surface tetra (blue circles), cave tetra (red triangles), and zebrafish (green diamonds) with all age groups combined. B, C, interval plots illustrating differences in eye depth (B) and eye width (C) of surface tetra (blue circles), cave tetra (red triangles), and zebrafish (green diamonds) at each age group. Different letters indicate statistically significant differences between group means (compared between types of fish within each timepoint). Error bars indicate standard deviation (B, C).*

2.3.2 Scleral cartilage depth differs between teleosts during development.

In order to better understand the differences in scleral cartilage depth between the surface tetra, cave tetra, and zebrafish, scleral cartilage depth was compared between surface tetras, cave tetras, and zebrafish at each timepoint in the developmental series (Figure 2.3).

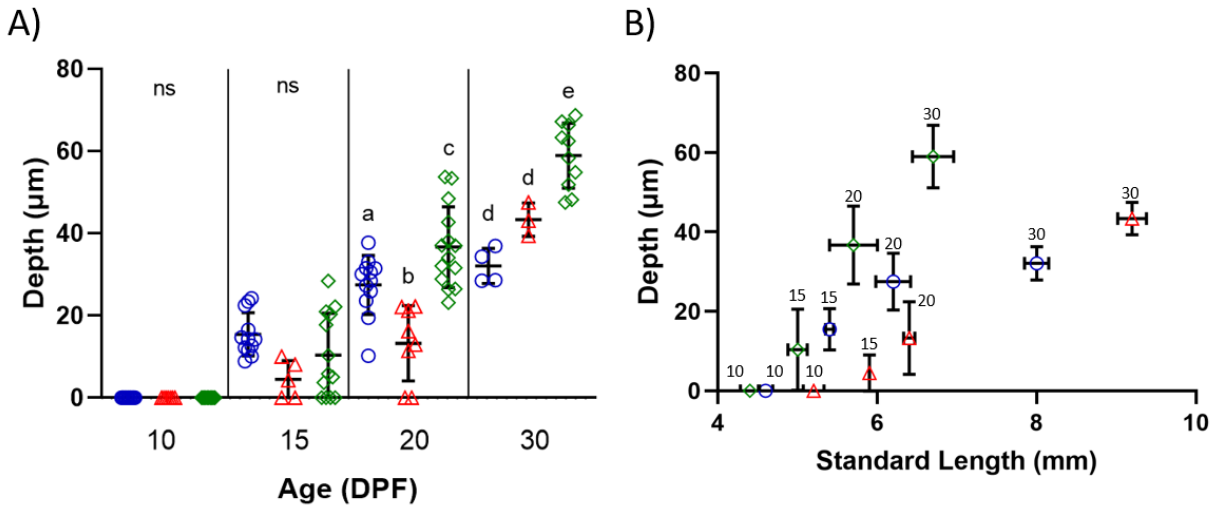

Figure 2.3. *Comparison of scleral cartilage depth between surface tetras, cave tetras, and zebrafish at 10-, 15-, 20-, and 30-dpf. A, an interval plot of scleral cartilage depth for surface tetras (blue circles), cave tetras (red triangles), and zebrafish (green diamonds). Different letters indicate statistically significant differences between group means (compared within each timepoint). B, a scatterplot comparing mean scleral cartilage depth to mean standard length for surface tetras (blue circles), cave tetras (red triangles), and zebrafish (green diamonds) at each timepoint. Timepoints are indicated by numbers above each point in the scatter plot (e.g., 10 = 10-dpf). Error bars indicate standard deviation (A, B).*

Scleral cartilage was not apparent in any samples at 10-dpf; hence, each type of fish has an average scleral cartilage depth of zero at this timepoint. By 15-dpf, scleral cartilage was

apparent in all surface tetras analyzed, and the majority of cave tetras and zebrafish. Surface tetra had a mean scleral cartilage depth of 15.47 μm (SD 5.20 μm), cave tetra had a mean scleral cartilage depth of 4.48 μm (SD 4.58 μm) and zebrafish had a mean scleral cartilage depth of 10.34 μm (SD 10.23 μm) (Figure 2.3A, B). No statistically significant differences were present at the 15-dpf timepoint (Figure 2.3A).

By 20-dpf, all surface tetra and zebrafish samples analyzed possessed scleral cartilage, while some cave tetras still lacked scleral cartilage (Figure 2.3A). Surface tetra had a mean scleral cartilage depth of 27.16 μm (SD 7.16 μm), cave tetra had a mean scleral cartilage depth of 13.27 μm (SD 9.14 μm) and zebrafish had a mean scleral cartilage depth of 36.68 μm (SD 9.84 μm) (Figure 2.3A, B). Statistically significant differences in mean scleral cartilage depth were found between each type of fish at 20-dpf (Tukey's test: surface tetra vs. cavefish, $p<0.001$; surface tetra vs. zebrafish, $p<0.05$; cavefish vs. zebrafish, $p<0.0001$) (Figure 2.3A).

By 30-dpf, each cavefish sample analyzed also possessed scleral cartilage (Figure 2.3A). Surface tetra had a mean scleral cartilage depth of 32.11 μm (SD 4.24 μm), cave tetra had a mean scleral cartilage depth of 43.36 μm (SD 4.06 μm) and zebrafish had a mean scleral cartilage depth of 58.94 μm (SD 7.92 μm) (Figure 2.3A, B). A statistically significant difference in mean scleral cartilage depth were not found between the two tetra morphs, however, there was a statistically significant difference between the mean scleral cartilage depth of zebrafish and each tetra morph (Tukey's test: surface tetra vs. zebrafish, $p<0.0001$; cave tetra vs. zebrafish $p<0.05$) (Figure 2.3A). Exact values for all measurements and mean values are given in Appendix C with the p-values for each comparison in Appendix D.

A scatter plot illustrating the relationship between mean scleral cartilage depth and mean standard length was constructed in order to understand the differences in standard length at each of these timepoints (Figure 2.3B). This analysis demonstrates a similar trend in terms of increasing scleral cartilage depth during development. Additionally, this plot further illustrates the growth plateau met by surface tetras after 20-dpf (or approximately 6.1 mm SL), while the cave tetra and zebrafish demonstrate a linear increase in depth throughout the developmental stages examined.

In summary these data illustrate distinct differences in scleral cartilage depth throughout development for each type of fish examined. Specifically, it appears that surface tetra scleral cartilage is fully present by 15-dpf (5.4 mm SL), but its growth plateaus at 20-dpf (6.2 mm SL) and is not significantly different by 30-dpf (8.0 mm SL). In contrast, cave fish scleral cartilage generally appears by 15-dpf (5.9 mm SL) but remains absent in some fish until as old as 20-dpf (6.4 mm SL). However, by 30-dpf (9.2 mm SL), all cavefish possess scleral cartilage, and their mean scleral cartilage depth increases steadily over the timepoints examined. It is unclear if the cartilage increases in depth with increasing age. Finally, zebrafish scleral cartilage is apparent in most zebrafish by 15-dpf (5.0 mm SL) and is present in all zebrafish by 20-dpf (5.7 mm SL). In contrast to the other sighted fish (i.e., the surface tetra), zebrafish scleral cartilage depth increases gradually between all timepoints examined and appears to still be in a period of growth. In general, it appears that scleral cartilage depth increases during development in each type of fish. Interestingly, the surface tetra scleral cartilage depth appears to plateau between 20- and 30-dpf at approximately 30 μm, while the scleral cartilage of both cave tetras and zebrafish continues to deepen between 20- and 30-dpf. Further research examining more advanced stages of cavefish and zebrafish are required in order to understand when cartilage depth ceases to increase.

2.3.3 Cave tetra scleral cartilage is deeper than sighted fish scleral cartilage relative to eye depth.

In order to understand the differences between perceived ‘narrow’ and ‘deep’ scleral cartilage rings, the mean scleral cartilage depth of the surface tetra, cavefish, and zebrafish were compared with respect to eye depth.

The relative scleral cartilage depth was plotted at each timepoint for each type of fish examined. It was found that at 15-dpf, the relative scleral cartilage depth was similar between each type of fish examined, with the scleral cartilage encompassing approximately 10% of the eye (Figure 2.4). At 20-dpf, the relatively scleral cartilage depth was similar between each type of fish, encompassing closer to 20% of the eye (Figure 2.4). By 30-dpf, differences were apparent in relative scleral cartilage depth between each type of fish, with the cave tetra displaying a much greater relative depth than its sighted counterparts. Interestingly, the relative scleral cartilage depth of zebrafish appeared to be greater than that of the surface tetras at 30-dpf. Specifically, by 30-dpf surface tetra had a relative scleral cartilage depth of 17.9% (SD 2.0%), cave tetra had a relative scleral cartilage depth of 72.4% (SD 8.9%), and zebrafish had a relative scleral cartilage depth of 31.2% (SD 3.5%) (Figure 2.4). Via a one-way ANOVA, it was found that relative scleral cartilage depth was significantly different between each type of fish at the 30-dpf timepoint. All measurements and mean values can be found in Appendix C with p-values for each comparison given in Appendix D.

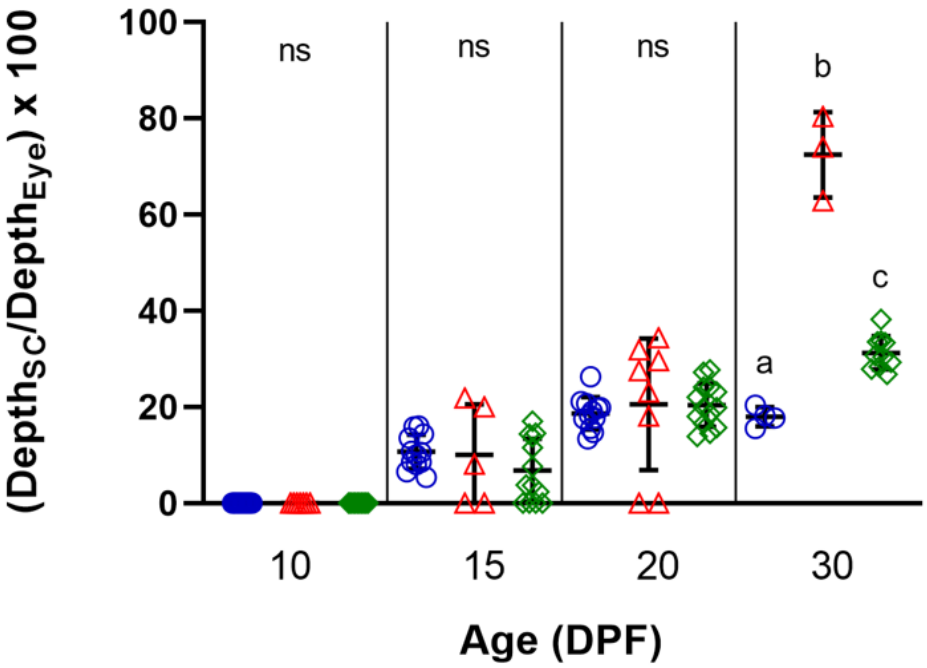

Figure 2.4. *Relative scleral cartilage depth with regard to eye depth. The percentage of eye depth covered by scleral cartilage is shown on the y-axis and compared for the surface tetra (blue circle), cave tetra (red triangle), and zebrafish (green diamond) at 10-, 15-, 20-, and 30-dpf. Different letters indicate a statistically significant difference between group means, compared within each timepoint. Error bars indicated standard deviation.*

These data show that surface tetra, cave tetra, and zebrafish scleral cartilage encompasses a relatively small portion of the eye early in development, but differences in encompassment arise at 30-dpf. Interestingly, the surface tetra and cave tetra show similar scleral cartilage depth in terms of an absolute measure (Figure 2.3), however, in terms of relative depth the cave tetra scleral cartilage covers a much greater proportion of the eye, leading to the observation of a cup-like scleral cartilage (Figure 2.4). However, other morphological differences in scleral cartilage may exist between the morphs.

2.3.4 Scleral cartilage cell count differs between teleosts during development.

In order to better understand the differences in scleral cartilage morphology between sighted fish and the cave tetra, the number of chondrocytes comprising the scleral cartilage of each fish was compared between surface tetras, cave tetras, and zebrafish at each timepoint in the developmental series.

Scleral cartilage was not apparent in any samples at 10-dpf; hence, each type of fish has an average scleral cartilage cell count of zero at this timepoint. By 15-dpf, scleral cartilage was apparent in all surface tetras analyzed and many cave tetras and zebrafish. Surface tetra had a mean scleral cartilage cell count of 1.75 cells (SD 0.73 cells), cave tetra had a mean scleral cartilage cell count of 0.60 cells (SD 0.63 cells) and zebrafish had a mean scleral cartilage cell count of 1.78 cells (SD 1.82 cells) (Figure 2.5A, B). No statistically significant differences were present at the 15-dpf timepoint (Figure 2.5A).

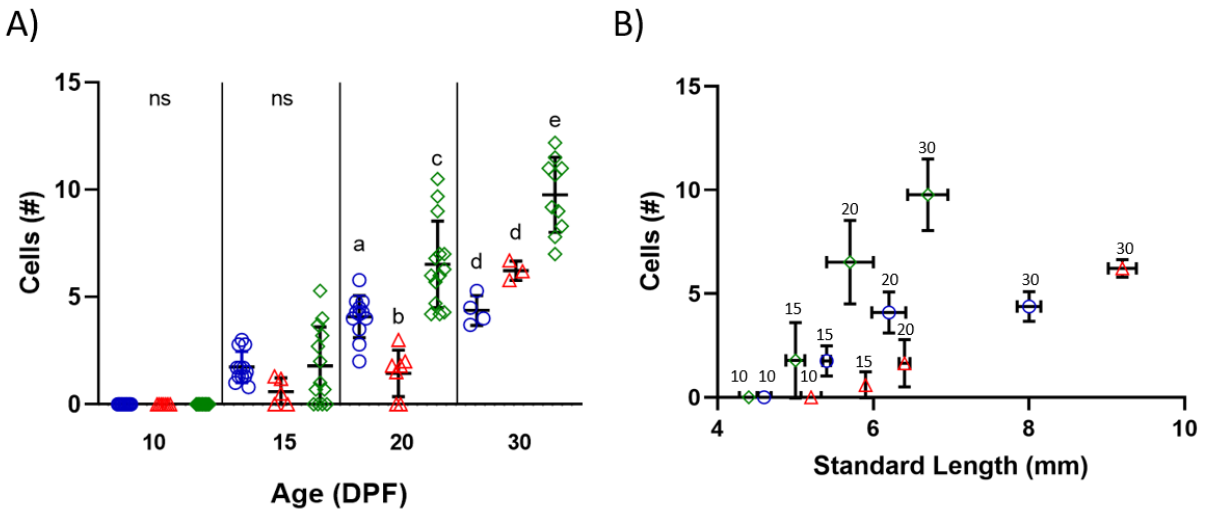

Figure 2.5. *Comparison of scleral cartilage cell count between surface tetras, cave tetras, and zebrafish at 10-, 15-, 20-, and 30-dpf. A, an interval plot of scleral cartilage cell count for*

surface tetras (blue circles), cave tetras (red triangles), and zebrafish (green diamonds). Different letters indicate statistically significant differences between group means (compared within each timepoint). B, a scatterplot comparing mean scleral cartilage cell count to mean standard length for surface tetras (blue circles), cave tetras (red triangles), and zebrafish (green diamonds) at each timepoint. Timepoints are indicated by numbers above each point in the scatter plot (e.g., 10 = 10-dpf). Error bars indicate standard deviation (A, B).

By 20-dpf, all surface tetra and zebrafish samples analyzed possessed scleral cartilage, while some cave tetras still lacked scleral cartilage (Figure 2.5A). Surface tetra had a mean scleral cartilage cell count of 4.06 cells (SD 1.00 cells), cave tetra had a mean scleral cartilage cell count of 6.22 cells (SD 0.42 cells) and zebrafish had a mean scleral cartilage cell count of 6.52 cells (SD 2.02 cells) (Figure 2.5A, B). Statistically significant differences in mean scleral cartilage cell count were found between each type of fish at 20-dpf (Tukey's test: surface tetra vs. cavefish, $p<0.001$; surface tetra vs. zebrafish, $p<0.0001$; cavefish vs. zebrafish, $p<0.0001$) (Figure 2.5A).

By 30-dpf, surface tetra had a mean scleral cartilage cell-count of 4.38 cells (SD 0.73 cells), cave tetra had a mean scleral cartilage cell count of 6.22 cells (SD 0.42 cells) and zebrafish had a mean scleral cartilage depth of 9.77 cells (SD 1.73 cells) (Figure 2.5A, B). A statistically significant difference in mean scleral cartilage cell count were not found between the two tetra morphs, however, there was a statistically significant difference between the mean scleral cartilage cell count of zebrafish and each tetra morph (Tukey's test: surface tetra vs. zebrafish, $p<0.0001$; cave tetra vs. zebrafish $p<0.05$) (Figure 2.5A). The values for all cell counts and mean values can be found in Appendix C with p-values for each comparison given in Appendix D.

In summary, these data illustrate distinct differences in scleral cartilage cell count. throughout development for each type of fish examined. Overall, the apparent trends in this analysis heavily resemble those observed in the analysis of scleral cartilage depth, indicating a close relationship between scleral cartilage depth and cell count. In general, it appears that the number of chondrocytes comprising the scleral cartilage increases during development in each type of fish. Interestingly, the number of chondrocytes comprising surface tetra scleral cartilage appears to plateau between 20-dpf and 30-dpf at approximately 4 cells (similar to the plateau observed with mean scleral cartilage depth), while the number of chondrocytes comprising the scleral cartilage of both cave tetras and zebrafish continues to increase between 20- and 30-dpf.

In order to understand the differences in standard length at each of these timepoints, a scatter plot illustrating the relationship between mean scleral cartilage cell count and mean standard length was constructed (Figure 2.5B). Overall, this plot illustrated trends similar to those described above.

2.3.5 Scleral cartilage chondrocytes are larger in cave tetras compared to surface tetras.

In order to determine whether differences in scleral cartilage depth were due to a combination of both cell-count and cell-size, scleral cartilage chondrocytes size was assessed via comparison of cross-sectional area. Surface tetra at 15-dpf had a mean cross-sectional area of 26.97 μm^2 (SD 6.86 μm^2), while cave tetra at 15-dpf had a mean cross-sectional area of 22.93 μm^2 (SD 2.63μm^2). No significant difference in mean chondrocyte cross-sectional area was found at 15-dpf (Tukey's Test, $p>0.05$). Surface tetra at 20-dpf had a mean chondrocyte cross-sectional area of 31.10 μm^2 (SD 19.41 μm^2), while cave tetra at 20-dpf had a mean chondrocyte cross-sectional area of 47.76 μm^2 (SD 17.94 μm^2) (Tukey's test, $p<0.05$; Figure 2.6). Surface tetra at 30-dpf had a

mean chondrocyte cross-sectional area of 41.72 μm^2 (SD 13.30 μm^2), while cave tetra at 30-dpf had a mean chondrocyte cross-sectional area of 59.10 μm^2 (SD 24.66 μm^2) (Tukey's test, $p<0.01$). In summary, it was found that the mean chondrocyte cross-sectional area of cave fish was higher than surface fish chondrocyte cross sectional area at both 20-dpf and 30-dpf, but not at 15-dpf.

In order to determine whether the larger cell size observed in the scleral cartilage chondrocytes of the cave fish were a common feature of all cells in this morph, the differences in cell size between the tetra morphs was further assessed by comparing the cross-sectional area of cell bodies in the retinal ganglion cell layer (These cells were chosen as they are present in the same eye sections of the scleral cartilage). The data shows that there was no significant difference between the cross-sectional area of retinal ganglion cell bodies between the tetra morphs at either timepoint examined (Tukey's Test, $p>0.05$). This result indicates that, generally, surface tetras and cave tetras possessed similarly sized retinal ganglion cells. Therefore, the differences in chondrocyte cross-sectional area variability observed in Figure 2.6 may indicate continued chondrocyte proliferation in the cave morph. Further research is needed to explore rates of cell proliferation within the scleral cartilage.

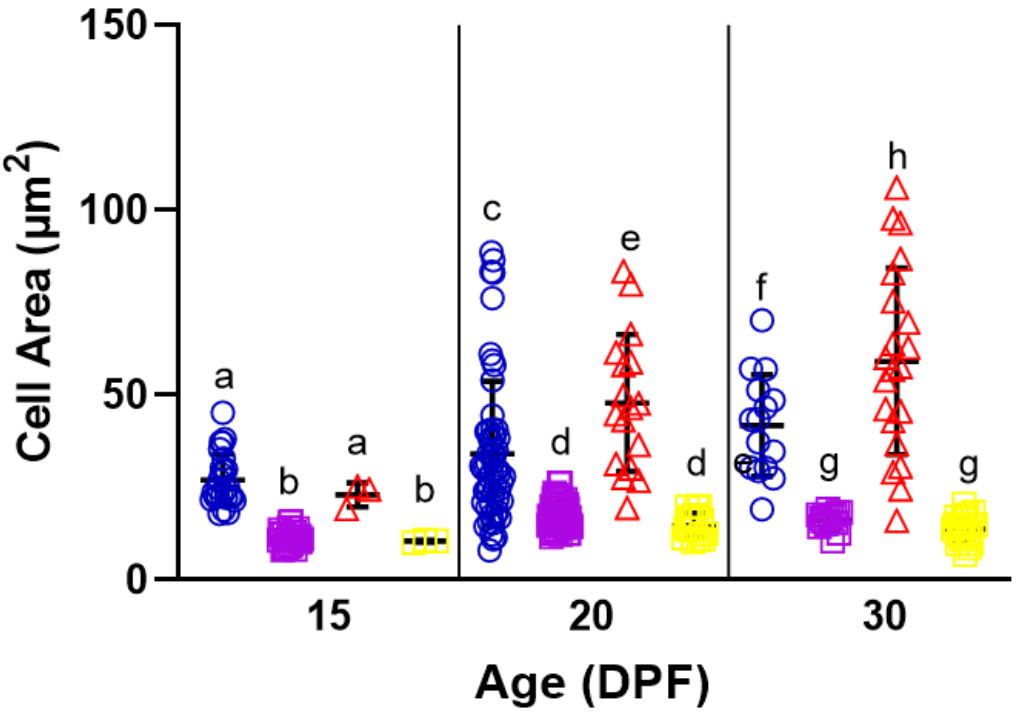

Figure 2.6. *Comparison of scleral cartilage chondrocyte cross-sectional area for surface tetras and cave tetras at 15-, 20-, and 30-dpf. Cross-sectional area of surface tetra chondrocytes (blue circles) and retinal ganglion cell bodies (purple squares), as well as cave tetra chondrocytes (red triangles) and retinal ganglion cell bodies (yellow squares) are compared within each timepoint. Error bars indicate standard deviation.*

2.3.6 Scleral cartilage first appears near the ora serrata.

In order to determine the location of scleral cartilage emergence in teleosts, coronal sections of the eye were examined. It was hypothesized that scleral cartilage would emerge near the anterior most point of the optic cup tissues, or the ora serrata (the junction point of the retinal pigmented epithelium and the photoreceptor cell layer). Indeed, in each type of fish examined the scleral cartilage was first apparent near this junction point (Figure 2.7.).

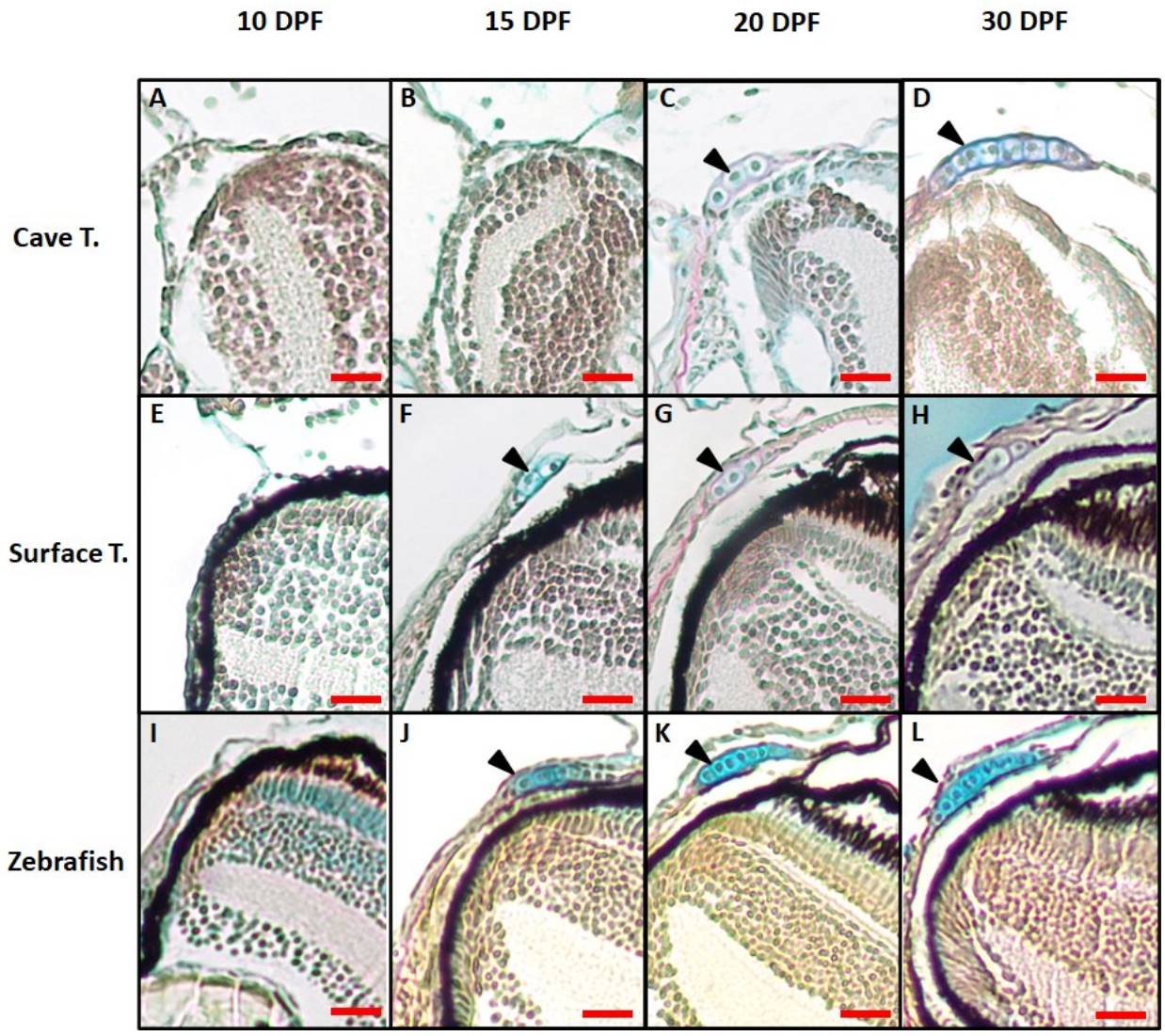

Figure 2.7. *Developmental series of surface tetra, cave tetra, and zebrafish displaying scleral cartilage in coronal sections. A-D, coronal sections of cave tetra eyes at 10-, 15-, 20-, and 30-dpf. E-H, coronal sections of surface tetra eyes at 10-, 15-, 20-, and 30-dpf. I-L, coronal sections of zebrafish eyes at 10-, 15-, 20-, and 30-dpf. The caudal portion of the scleral cartilage ring is shown in each image. Arrowheads indicate scleral cartilage. Scale bars represent 15 µm.*

In congruence with the previous results for scleral cartilage depth and cell-count, no fish displayed scleral cartilage at 10-dpf (Figure 2.7A, E, I). By 15-dpf, both the surface tetra and

zebrafish possessed scleral cartilage near the ora serrata (Figure 2.7F, J), while many cave tetras still lacked cartilage (Figure 2.7B). By 20-dpf, scleral cartilage was observed consistently in each type of fish at the ora serrata junction point (Figure 2.7C, G, K). Finally, by 30-dpf, a robust section of scleral cartilage was observed in each type of fish in a similar position (Figure 2.7D, H, L). Interestingly, it appeared that the anterior aspect of the scleral cartilage extended anteriorly, past the ora serrata in several of these sections (e.g., Figure 2.7C, G, K). Thus, an examination of the anterior extent of the scleral cartilage was performed.

By measuring the angle between the anterior aspect of the scleral cartilage and the 'width line' previously used for determination of eye size, a difference was observed in the positioning of the scleral cartilage between the rostral and caudal portions of the ring. While the rostral portion of the scleral cartilage ring of 30-dpf surface tetras and zebrafish exists in a close proximity to the ora serrata (with a mean offset of -3.0° and -1.7°, respectively), the caudal portion of the scleral cartilage is positioned anteriorly with respect to the ora serrata (with a mean offset of 9.0° and 9.2°, respectively) (Figure 2.8). In contrast, both the rostral and caudal portions of the cave tetra scleral cartilage ring are positioned anteriorly with respect to the ora serrata (with a mean rostral offset of 15.6° and a mean caudal offset of 24.2°) (Figure 2.8). Thus, the scleral cartilage ring appears to vary in proximity to the ora serrata at different points around its circumference in the surface tetra and zebrafish, while cave fish scleral cartilage is positioned anteriorly in both regions analyzed. This deviation from surface tetra and zebrafish is likely due to morphological changes in the cave tetra eye throughout degeneration. Exact values for all measurements and mean values can be found in Appendix C.

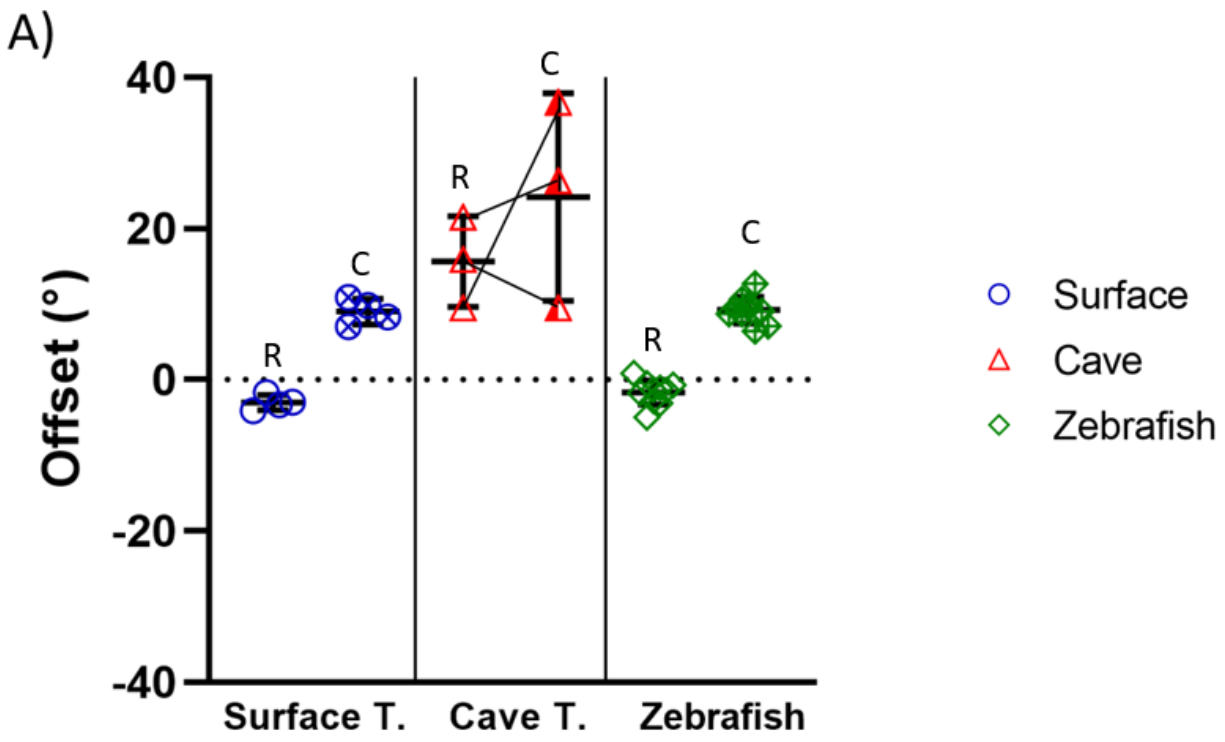

Figure 2.8. *Offset angle of scleral cartilage with respect the ora serrata. Angles were measured between the anterior most point of the scleral cartilage and the ora serrata, using the midpoint of the eye-width measure as a vertex. A, offset angles for rostral and caudal scleral cartilage of surface tetras (rostral, empty blue circles, caudal, crossed blue circles), cave tetras (rostral, empty red triangles, caudal, semi-filled red triangles), and zebrafish (rostral, empty green diamonds, caudal, crossed green diamonds. Cave tetra data points from the same eye are paired with connecting lines. Rostral measurements indicated by 'R'; Caudal measurements indicated by 'C'. Error bars indicate standard deviation.*

2.3.7 Scleral cartilage does not develop uniformly around the eye.

In order to further assess the differences in the uniformity of teleost scleral cartilage development, scleral cartilage depth and cell-count in the rostral and caudal regions of the eye

were compared for the surface tetra (Figure 2.9), cave tetra (Figure 2.10), and zebrafish (Figure 2.11).

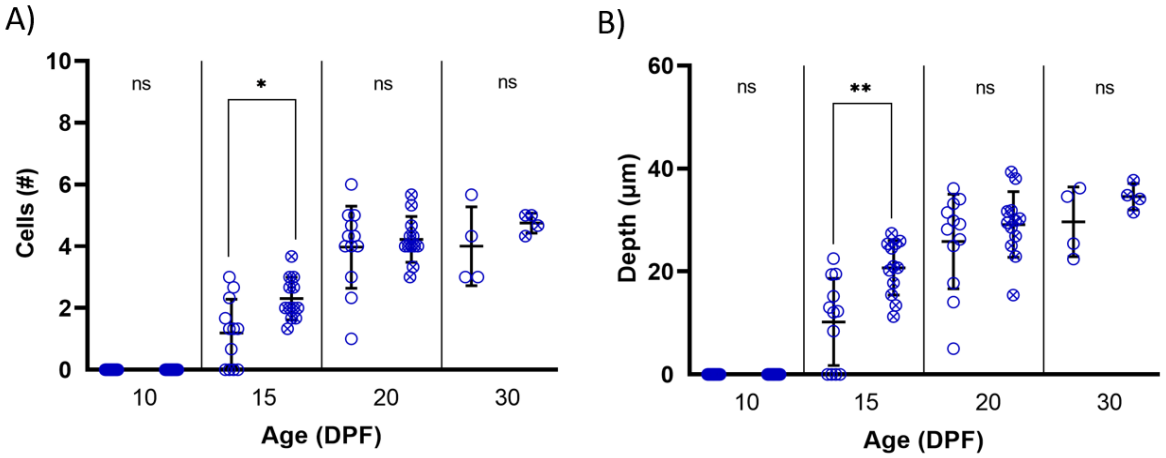

Figure 2.9. *Comparisons of cell count and depth of scleral cartilage between rostral and caudal regions of the surface tetra scleral cartilage ring. A, the differences in cell number between rostral (empty circle) and caudal (crossed-circle) region of the scleral cartilage at 10-,15-,20-, and 30-dpf. B, the differences in scleral cartilage depth between rostral (empty circle) and caudal (crossed circle) region of the scleral cartilage at 10-,15-,20-, and 30-dpf. Error bars indicate standard deviation. Statistical significances are indicated by asterisks (*, $p<0.05$, **, $p<0.01$).*

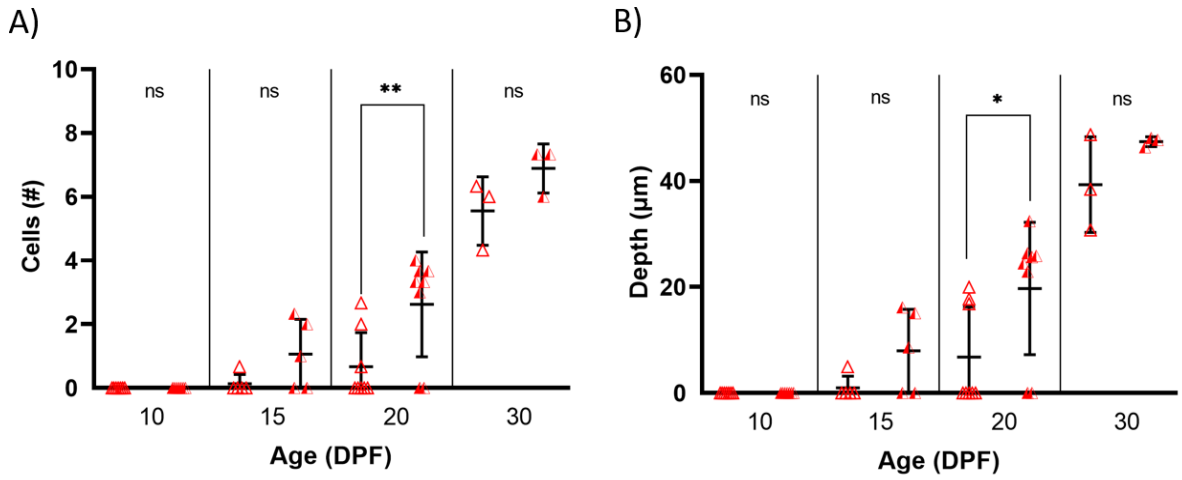

Figure 2.10. *Comparisons of cell count and depth of scleral cartilage between rostral and caudal regions of the cave tetra scleral cartilage ring. A, the differences in cell number between rostral (empty triangle) and caudal (semi-filled triangle) region of the scleral cartilage at 10-,15-,20-, and 30-dpf. B, the differences in scleral cartilage depth between rostral (empty triangle) and caudal (semi-filled triangle) region of the scleral cartilage at 10-,15-,20-, and 30-dpf. Error bars indicate standard deviation. Statistical significances are indicated by asterisks (*, $p<0.05$, **, $p<0.01$).*

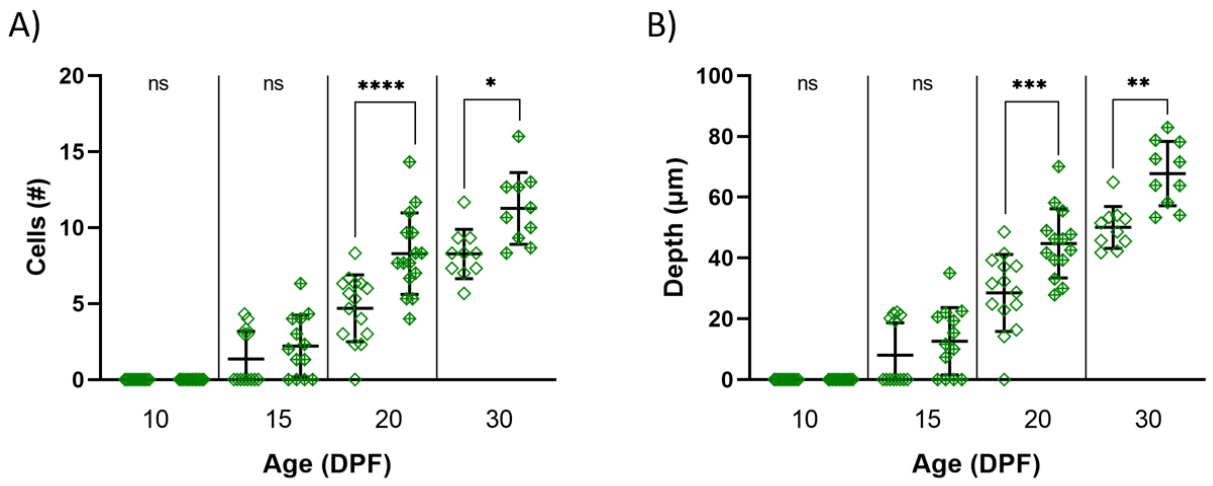

Figure 2.11. *Comparisons of cell count and depth of scleral cartilage between rostral and caudal regions of the zebrafish scleral cartilage ring. A, the differences in cell number between rostral (empty diamond) and caudal (crossed-diamond) region of the scleral cartilage at 10-,15-,20-, and 30-dpf. B, the differences in scleral cartilage depth between rostral (empty diamond) and caudal (crossed-diamond) region of the scleral cartilage at 10-,15-,20-, and 30-dpf. Error bars indicate standard deviation. Statistical significances are indicated by asterisks (*, $p<0.05$, **, $p<0.01$, ***, $p<0.001$, ****, $p<0.0001$).*

Surface tetras at 15-dpf had a mean cell count of 1.19 cells rostrally (SD 1.04 cells) and 2.31 cells caudally (SD 0.66 cells) (Tukey test $p<0.05$; Figure 2.9A) and a mean depth of 10.21 µm rostrally (SD 8.08 µm) and 20.73 µm caudally (SD 5.08 µm) (Tukey test $p<0.01$; Figure 2.9B). Surface tetras at 20-dpf had a mean cell count of 3.97 cells rostrally (SD 1.28 cells) and 4.22 cells caudally (SD 0.73 cells) (Figure 2.9A) and a mean depth of 25.85 µm rostrally (SD 8.82 µm) and 29.12 µm caudally (SD 6.18 µm) (Figure 2.9B). Finally, surface tetras at 30-dpf had a mean cell count of 4.00 cells rostrally (SD 1.11 cells) and 4.75 cells caudally (SD 0.28 cells) (Figure 2.9A) and a mean depth of 29.66 µm rostrally (SD 5.86 µm) and 34.56 µm caudally (SD 2.23 µm) (Figure

2.9B). This data indicates that surface tetra scleral cartilage develops non-uniformly, indicated by differences in the rostral and caudal regions early in development (i.e., 15-dpf). However, uniformity is achieved later in development as growth-rate is reduced (i.e., >20-dpf).

Cave tetras at 15-dpf had a mean cell count of 0.13 cells rostrally (SD 0.27 cells) and 1.07 cells caudally (SD 0.98 cells) (Figure 2.10A) and a mean depth of 0.99 μm rostrally (SD 1.98 μm) and 7.97 μm caudally (SD 7.00 μm) (Figure 2.10B). Cave tetras at 20-dpf had a mean cell count of 0.67 cells rostrally (SD 1.00 cells) and 2.625 cells caudally (SD 1.55 cells) (Tukey's test, $p<0.01$; Figure 2.10A) and a mean depth of 6.82 μm rostrally (SD 7.03 μm) and 19.72 μm caudally (SD 11.45 μm) (Tukey's test, $p<0.05$; Figure 2.10B). Finally, cave tetras at 30-dpf had a mean cell count of 5.56 cells rostrally (SD 0.79 cells) and 6.89 cells caudally (SD 0.47 cells) (Figure 2.10A) and a mean depth of 39.30 μm rostrally (SD 7.37 μm) and 47.41 μm caudally (SD 0.77 μm) (Figure 2.10B). This data illustrates that cave tetra scleral cartilage develops non-uniformly, indicated by statistically significant differences in the rostral and caudal regions at earlier stages of development (i.e., 20-dpf). Interestingly, this trend appears to continue into later development (i.e., 30-dpf), however, a statistical difference was not found in comparisons at the 30-dpf timepoint, likely due to small sample size.

Zebrafish at 15-dpf had a mean cell count of 1.36 cells rostrally (SD 1.75 cells) and 2.21 cells caudally (SD 1.95 cells) (Figure 2.11A) and a mean depth of 8.07 μm rostrally (SD 10.23 μm) and 12.62 μm caudally (SD 10.66 μm) (Figure 2.11B). Zebrafish at 20-dpf had a mean cell count of 4.69 cells rostrally (SD 2.10 cells) and 8.29 cells caudally (SD 2.65 cells) (Tukey's test, $p<0.0001$; Figure 2.11A) and a mean depth of 28.54 μm rostrally (SD 12.21 μm) and 44.81 μm caudally (SD 10.95 μm) (Tukey's test, $p<0.001$; Figure 2.11B). Finally, zebrafish at 30-dpf had a mean cell count of 8.27 cells rostrally (SD 1.55 cells) and 11.27 cells caudally (SD 2.25 cells)

(Tukey's test, $p<0.05$; Figure 2.11A) and a mean depth of 50.09 μm rostrally (SD 6.54 μm) and 67.78 μm caudally (SD 10.06 μm) (Tukey's test, $p<0.01$; Figure 2.11B). This data shows that zebrafish scleral cartilage develops non-uniformly, indicated by statistically significant differences in the rostral and caudal regions at 20-dpf and 30-dpf. Based on this data, it is unclear when zebrafish scleral cartilage growth-rate is reduced, or if uniformity is achieved later in development. A similar analysis at a later timepoint would be necessary to answer these questions.

In each type of fish examined, gradual increases in the rostral and caudal scleral cartilage depth and cell-count were observed across the 10-dpf to 30-dpf timepoints (Figures 2.9, 2.10, 2.11), congruent with the previous results in which the rostral-caudal averages were presented (Figures 2.3, 2.5). In surface tetras (Figure 2.9), it appeared that rostral and caudal scleral cartilage depth and cell-count differed at 15-dpf but became more similar at the 20-dpf and 30-dpf timepoints. In cave tetras (Figure 2.10), it appeared that rostral and caudal scleral cartilage depth and cell-count differed at each stage following emergence of the scleral cartilage. In zebrafish (Figure 2.11), a similar difference in rostral and caudal scleral cartilage depth and cell-count was observed, but mainly at the 20-dpf and 30-dpf timepoints.

In summary, this data illustrates that teleost scleral cartilage does not develop evenly around the eye in terms of cell count and depth in each type of fish examined. In the tetra morphs statistically significant differences in both scleral cartilage cell count and depth (in the rostral and caudal portions of the eye) are apparent in at 15-dpf in surface fish and at 20-dpf in cave fish. Interestingly, these differences appear to decrease as development continues, as seen in later timepoints when no statistically significant differences are present. In a similar fashion to the tetra morphs, zebrafish scleral cartilage also displays uneven development of the rostral and

caudal regions as denoted by statistically significant differences in scleral cartilage cell count and depth at both 20-dpf and 30-dpf. In all fish, these differences are characterized by deeper cartilage in the caudal portion of the scleral cartilage ring compared to the rostral portion.

2.4 Discussion

2.4.1 Restatement of Objective and Hypotheses

The objective of the research presented in this Chapter was to determine the pattern of scleral cartilage induction and growth in teleosts with different scleral cartilage morphology. It was hypothesized that scleral cartilage induction would first occur in the sclera near the anterior most extent of the optic cup tissues (ora serrata). This was found to be true. Secondly, it was hypothesized that in fish with deeper scleral cartilage rings (e.g., the Pachón cave tetra), that growth would continue in the posterior direction (towards the back of the eye) and that in species with narrow scleral cartilage rings, growth will be halted after chondrogenesis has occurred, resulting in a narrow ring of scleral cartilage. This will be discussed below.

2.4.2 Slight Differences are Present in Scleral Cartilage Development in Teleosts.

Via an analysis of scleral cartilage cell count and depth, it was found that differences exist in the timing of scleral cartilage appearance between surface tetra, cave tetra, and zebrafish. While differences between the tetra morphs and zebrafish are unsurprising due to their more distant phylogenetic relation, the apparent differences between the closely related surface and cave tetras are striking. Specifically, a delay in the development of cave tetra scleral cartilage (relative to the development of surface tetra cartilage) indicates potential differences in the timing of cartilage induction signals in the eye. Moreover, it is possible that as the cave tetra eye degenerates, inductive signaling from the degenerating eye tissues may be reduced leading to the

observed delay in scleral cartilage initiation. Additionally, it is possible that the apparent delay in cave tetra scleral cartilage development is due to acquired differences in gene expression profiles over time. Such differences have been indicated as potential causes of eye degeneration and lack of ossification in the ocular skeleton in the cave tetra. (McGaugh et al., 2014; O'Quin et al., 2015).

While the scleral cartilage of the surface tetra appears earlier in development (and therefore is deeper at earlier timepoints) compared to its blind counterpart, by 30-dpf, both the cell-count and depth of cave tetra scleral cartilage increase to equal the measurements taken in surface tetra. However, when scleral cartilage depth is considered relative to the eye size of each tetra morph, the cave tetra cartilage by far exceeds the surface tetra in (relative) cartilage depth. In addition, the scleral cartilage depth and cell count of the surface tetra plateaus between 20-dpf and 30-dpf, while there is no evidence of a plateau in cave tetra scleral cartilage growth in the timepoints examined and growth may still be proceeding. The deep, cup-like scleral cartilage observed in Pachón cave tetra adults is likely the result of both decreased eye size and prolonged cartilage growth, compared to the surface tetra. The signals to stop cartilage growth in the posterior direction appear to be missing in the cavefish, despite advanced eye degeneration.

Interestingly, our analysis shows that zebrafish have scleral cartilage that has a greater depth and cell-count compared to both tetra morphs (Figures 2.2, 2.3). However, when considered relative to eye size, the scleral cartilage of zebrafish covers a similar (though slightly greater) proportion of the eye's depth to the surface tetra (Figure 2.4). Thus, the apparent difference in depth between the surface tetra and cave tetra scleral cartilage was mainly accounted for by eye size.

While the overall depth and cell-count of surface tetra and cave tetra scleral cartilage were shown to be similar by 30-dpf, a difference in scleral cartilage chondrocyte size was demonstrated via analysis of scleral cartilage chondrocyte cross-sectional area (Figure 2.5). Interestingly, this analysis suggested that cave tetra possess larger scleral cartilage chondrocytes than surface tetra at the 20-dpf and 30-dpf timepoints (Figure 2.6). Additionally, increased variation in chondrocyte size was observed for cave tetras. These results suggest potential differences in the regulation of chondrocyte differentiation, specifically in an increased proliferative phase in the cave tetra. Similar to the observed temporal differences in scleral cartilage development between the morphs, differential regulation of chondrocyte proliferation and hypertrophy may be the result of recently acquired differences in gene expression (O'Quin et al., 2015). In order to further understand the mechanism responsible for this difference, a RT-qPCR study examining temporal changes in proliferation and hypertrophy regulating genes such as BMPs, FGFs, and WNT/ß-catenin could be conducted (Cole, 2011; Li & Dong, 2016).

2.4.3 Scleral Cartilage Position is Highly Conserved Amongst Teleosts

Based on the results collected from the histological analysis of scleral cartilage development in the surface tetra, cave tetra, and zebrafish, it is apparent that the scleral cartilage is first apparent near the ora serrata (Figure 2.6). However, a closer analysis of scleral cartilage positioning illustrated that the anterior aspect of the scleral cartilage differentially abuts the ora serrata depending on the portion of the scleral cartilage in question (Figure 2.7). Specifically, in sighted fish (surface tetra and zebrafish) the rostral portion of the scleral cartilage ring was positioned very close to the ora serrata, while the caudal portion of the scleral cartilage ring was position more anteriorly (towards the cornea). Interestingly, the scleral cartilage of cave tetras was positioned anteriorly to the ora serrata in both regions analyzed. However, similar to the

sighted fish, the anterior extend of the caudal region extends more anteriorly towards the cornea than the rostral region. This divergent cave tetra phenotype is likely due to degeneration of the cave tetra eye early in development, resulting in increased separation of the scleral cartilage and retinal tissues. That is, it is possible that an inductive signal is produced transiently near the ora serrata at a point in development, but as the eye degenerates, the developing scleral cartilage and ora serrata may become physically separated. In order to verify this, an eye-rescue experiment could be conducted in which the degenerating lens of the cave tetra eye is surgically replaced with the lens of a similarly aged surface tetra as previously demonstrated in the literature (Jeffery, 2001; Yamamoto & Jeffery, 2002). This experiment would allow for comparisons to be made between the tetra morphs, along with cave tetras with non-degenerate eye morphology, similar to the comparisons made in this study. Conversely, lens ablation has previously been shown to cause eye degeneration in sighted tetra (Dufton et al., 2012). Therefore, the scleral cartilage of lens ablated surface tetra and zebrafish could be examined for a similar phenotype to that found in the cave tetra.

2.4.4 Non-uniformity of the Scleral Cartilage Due to Periocular Mesenchyme Heterogeneity

No previous studies have examined or considered the potential of non-uniform development of the teleost scleral cartilage ring. This study demonstrates that the scleral cartilage of the surface tetra, cave tetra, and zebrafish differs in terms of depth and cell-count between the rostral and caudal portions of the ring, with a tendency towards a deeper caudal segment (Figures 2.8, 2.9, 2.10). The dorsal and ventral regions of the scleral cartilage ring were not examined in this study, though it is possible that differences exist in these regions as well. This result, in addition to the differential positioning of the scleral cartilage with respect to the optic cup tissues (Figure 2.7), demonstrates a conserved regulatory mechanism for cartilage induction between the

fish examined in this study. That is, it is likely that the signals responsible for cartilage induction are spatially conserved between the Mexican tetra and the zebrafish.

Interestingly, the POM (which gives rise to the scleral cartilage) is populated by multiple neural crest sub-populations from the posterior diencephalon and anterior mesencephalon and provides progenitor cells for the sclera in both zebrafish (Rocha et al., 2020; Williams & Bohnsack, 2020). Thus, it is possible that differences in competency are innately present in these cells (due to differences in their anterior-posterior patterning), or perhaps differences are accrued via different signaling environments along their migration pathways as seen in neural crest cells that give rise to the skeletal elements [e.g. in the chicken mandible and pharyngeal arch derivatives in the zebrafish; (Hall, 1981; Walshe & Mason, 2003; Le Douarin et al., 2004; Williams & Bohnsack, 2020)]. In recently published studies examining anterior eye segment morphogenesis in zebrafish, regional differences in the expression of neural crest transcription factors, such as *foxc1a, foxc1b,* and *foxd3,* were observed in the POM between 18-hpf to 72-hpf (Van Der Meulen et al., 2020; Van Der Meulen, 2021). For example, *foxc1a, foxc1b,* and *foxd3* generally displayed expression in the caudal POM, but over development (from 18-hpf to 48-hpf) *foxc1a* expression spreads around the dorsal and ventral periocular regions, *foxc1b* expression is mainly localized in the caudal and ventral POM, and *foxd3* expression remains localized in the caudal POM. Expression of each of these genes is necessary for the initiation of chondrogenesis (Lister et al., 2006; Cole, 2011; Xu et al., 2021), and thus, differences in their spatio-temporal expression pattern in the POM may relate to the observed regional differences in scleral cartilage positioning and depth during its development.

2.4.5 Conclusion

In conclusion, the research presented in this chapter has illustrated several differences in the pattern of teleost scleral cartilage development between the surface tetra, cave tetra, and zebrafish. These differences consist of differential timing of scleral cartilage emergence and growth, as well as in the relative depth of scleral cartilage, and chondrocyte size. However, several similarities were also shown. These include similar tendencies towards deeper scleral cartilage in the caudal segment of the cartilage ring in all fish examined, as well as a similar offset of the scleral cartilage with respect to the optic cup tissues. Overall, this research provides much needed foundational understanding of teleost scleral cartilage development and morphology.

Chapter 3: Assessing the Roles of TGF-ß and FGF Signaling via Intravitreal Injection

3.1 Introduction

Cartilage development initiates due to reciprocal inter-tissue signaling known as an epithelial-mesenchymal interaction (Hall, 1981). While much of the later signaling in cartilage development involved in differentiation, pre-chondrocyte proliferation, and hypertrophy has been documented (Murtaugh et al., 1999; Yan et al., 2002; Cole, 2011; Lim et al., 2015; Li & Dong, 2016 for review), little is known about the earliest inductive signals. Previous research has demonstrated a role for FGF signalling in the development of zebrafish cranial cartilages (Walshe & Mason, 2003). Additionally, TGF-ß signaling has been indicated in the regulation of adherence and cell-cell communication in the early mesenchymal condensation and involve such proteins as NCAM and N-Cadherin (Hall & Miyake, 2000; Cole, 2011). Moreover, previous research on scleral cartilage induction in the chicken, *Gallus gallus*, suggests that the RPE may be involved in the inductive epithelial-mesenchymal interaction (introduced in Chapter 1, Section 1.4). Thus, the research presented in this chapter aims to determine the role of FGFs and TGF-B in scleral cartilage development. I hypothesize that local inhibition of the FGFRs or TGF-B receptors will lead to disruption of scleral cartilage morphology.

The zebrafish FGF pathway signaling is mediated via five receptor sub-types, FGFR1a, FGFR1b, FGFR2, FGFR3, and FGFR4. Previous zebrafish knockout experiments have demonstrated the requirement of FGFR function in craniofacial cartilage development (Leerberg et al., 2019). Interestingly, a high degree of redundancy exists in the function of zebrafish FGFRs during craniofacial and neural development. Specifically, single knockouts of each FGFRs sub-

type produced relatively little effects on zebrafish development overall, but multiple knock-outs lead to severe disruption of viscerocranial and neurocranial morphology, as well as disruption to the midbrain-hindbrain boundary (Leerberg et al., 2019). The FGFR inhibitor used in this thesis, SSR128129E, functions via allosteric inhibition of FGFR1-4, preventing internalization of the receptor structure (C. Herbert et al., 2013). Previous research has demonstrated the expression of FGFs in the endoderm of the pharyngeal arches in zebrafish (Yelick & Schilling, 2002), and shown that disruption of FGF signaling via morpholino in zebrafish (specifically for *fgf8*) lead to similar effects as FGFR knockout experiments (Walshe & Mason, 2003). Previous experiments in the mouse have demonstrated that two genes downstream of FGF signaling in the chondrogenesis GRN, namely MSX1 and PAX9, are crucial in the development of cartilaginous structures of the pharyngeal arches (Peters et al., 1998; Alappat et al., 2003). Thus, inhibition of FGFR signaling via SSR128129E may cause disruption of the scleral cartilage in a MSX1 and/or PAX9 dependent manner.

TGF-ß signaling is generally mediated via three receptor sub-types, namely; TGF-ß IR (Type-I), TGF-ß IIR (Type-II), and TGF-ß IIIR (Type-III) (Massagué, 1992; Chai et al., 2003). TGF-ß signaling is mediated via heterodimerization of TGF-ß IR and IIR (while the high affinity TGF-ß IIIR is thought mainly to hold TGF-ß ligands near the cell membrane extracellularly, allowing for increased binding to the IR and IIR heterodimer) (Massagué, 1992; Chai et al., 2003). The TGF-ß signaling inhibitor used in this study, LY-364947, is a potent ATP-competitive inhibitor on TGF-ß IR, and thus is capable preventing heterodimer cross-phosphorylation, silencing all downstream effects of the TGF-ß signal cascade (Nassar et al., 2014). As such, following treatment with LY-364947, decreases in the expression of *NCAM1*

and *N-Cadherin* would be expected, which may lead to absence or morphological disruption of cartilage.

Thus, the research presented in this Chapter explores the effect that local inhibition of these signaling pathways (FGF and TGF- ß) has on scleral cartilage development via microinjections into the embryo at key time points of development (23-hpf and 26-hpf); these timepoints coincide with RPE differentiation in zebrafish (Lister, 2002; Cechmanek & McFarlane, 2017). However, scleral cartilage induction is not the only inductive process occurring near the developing eye around these timepoints. As such, it is possible that disruptions in other skeletal elements will be observed as a result of FGFR and TGF-ß inhibition, due to their involvement in the regulation of chondrogenic condensations. Thus, a suite of cartilage elements derived from distinct progenitor cell populations that develop at similar time points were also assessed (Figure 3.1). These included the epiphyseal bar, basihyal cartilage, and basicapsular cartilage. Each is justified below.

Teleost scleral cartilage is derived from the periocular mesenchyme (POM) (Kague et al., 2012). The POM is a pool of mesenchymal progenitor cells populated by diencephalic and mesencephalic cranial neural crest cells which can be first detected around the eye of zebrafish embryos by 23-hpf to 24-hpf (Klymkowsky et al., 2010). Interestingly, following establishment of the POM, a sub-population migrates to the dorsal aspect of the head in order to form the anterior portions of the neurocranium (Klymkowsky et al., 2010). In order to identify a possible disruptive effect on this POM sub-population, the epiphyseal bar was examined. The epiphyseal bar is a POM-derived cartilage in the dorsal neurocranium medial to the orbits that becomes apparent via histological section at 4.7 mm SL (Zebrafish Atlas; https://bio-

atlas.psu.edu/zf/progress.php), and is clearly visible via whole-mount staining at the 6.0 mm SL experimental endpoint (Cubbage & Mabee, 1996; Williams & Bohnsack, 2020).

The basihyal cartilage is an element of the viscerocranium located anteriorly to the ceratobrachial elements that emerges around 3.7 mm SL (Zebrafish Atlas; https://bio-atlas.psu.edu/zf/progress.php; Cubbage & Mabee, 1996). The basihyal cartilage is derived from cranial neural crest cells of the second pharyngeal arch which originate from the posterior mesencephalon and anterior rhombencephalon (Klymkowsky et al., 2010; Mongera et al., 2013; Williams & Bohnsack, 2020). Thus, the basihyal cartilage was assessed in order to identify any disruptive effects on these more posterior cranial neural crest cells.

The basicapsular cartilage is a portion of the ventral neurocranium that extends from the basal plate to the otic vesicle and emerges between 3.7 mm and 4.0 mm SL (Zebrafish Atlas; https://bio-atlas.psu.edu/zf/progress.php; Cubbage & Mabee, 1996). The basicapsular cartilage is likely derived from a combination of the most posterior cranial neural crest cells and head mesoderm (Kague et al., 2012; Mongera et al., 2013). As such, any observed disruptions of the basicapsular cartilage would indicate inhibitory effects on the posterior neural crest and mesoderm.

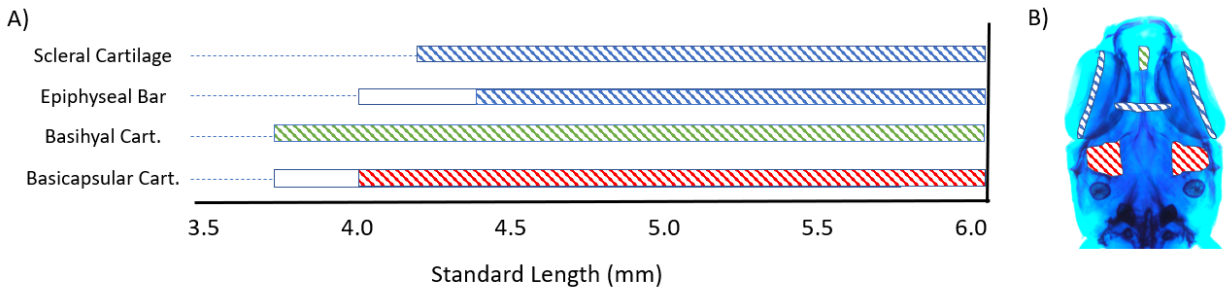

Figure 3.1. *Developmental timeline and positioning of the cartilages of interest. A, Hashed bars indicate the definitive presence of differentiated cartilage. Empty bars represent periods of uncertainty, where the structure may or may not be present (i.e., the epiphyseal bar and basicapsular cartilages are not present at the beginning of the empty bar but are definitely present by the beginning of the beginning of the hashed bars – the exact timing of emergence is unknown, but falls somewhere in the empty bars). A, B, Colours indicate the tissues of origin (blue, POM; green, pharyngeal neural crest; red, mixed neural crest and mesoderm). Data from Cubbage & Mabee, 1996; Zinck et al., 2021, as well as examination of histology in the Zebrafish Atlas; https://bio-atlas.psu.edu/zf/progress.php.*

Because of the simultaneous development of skeletal structures in and around the eye, it is necessary to consider the potential of diffuse effects (i.e., not localized to the scleral). Thus, careful examination of the chondrocranial elements will aid in identifying these potential effects and will aid in localizing any effects to specific progenitor populations.

3.2 Methods

3.2.1 Animal Husbandry

AB strain zebrafish (*D. rerio*) were provided from the Dalhousie Zebrafish Core Facility at Dalhousie University, Halifax, Nova Scotia. All processes involving zebrafish outlined below

were approved by the SMU-MSVU Animal Care Committee under protocol #20-17A1. Fish were obtained on the day of fertilization and reared at Mount Saint Vincent University. Between 10-20 zebrafish were housed glass cups containing approximately 300 mL of conditioned water maintained at 28°C via an external submersible heating unit. Water changes were performed daily of approximately 25% volume. Larvae were fed Gemma 75 following hatching (5 days post-fertilization). Once larvae were able to consume coarser grained food, they were fed Gemma 150.

3.2.2 Inhibitors

The small molecule inhibitors SSR128129E (Abcam 146107) and LY-364947 (Abcam 141890) were obtained in order to inhibit FGFR1-4 and the TGF-ß receptor, ALK-1, respectively. These inhibitors were chosen due to their previous use in zebrafish research, in which their activities were shown to sufficiently inhibit signaling from all FGFRs (SSR128129E) and all signaling downstream of TGF-ß (LY-363947) (Bono et al., 2013; De Smet et al., 2014; C. Herbert et al., 2013; Nassar et al., 2014). Throughout this Chapter, these inhibitors will be abbreviated as SSR and LY. Inhibitor stock solutions were made to a concentration of 50 mM in DMSO and stored at -80°C. A variety of injection concentrations were tested at two locations in the eye at each of the two time points (details are provided in Appendix B). On injection day, injection solutions were made via dilution of stock inhibitor solutions in zebrafish embryo medium. Injection solutions were made to concentrations of 0.25 mM and 0.50 mM. Additionally, a 5% DMSO control solution was made via dilution of 100% DMSO in zebrafish embryo medium. Phenol red was added to each injection solution at a concentration of 0.05% in order to visualize the injection bolus. These injection solutions were placed in an incubator at 28°C prior to injecting.

Prior to injections, zebrafish embryos were manually dechorionated using fine forceps. Dechorionated embryos were then housed in an incubator at 28°C. Embryos were staged using anatomical features in order to ensure they were at the proper timepoint for injections (23 hpf, 28-somite stage; 26 hpf, prim-8).

3.2.3 Intravitreal Injections

Once zebrafish were at their injection timepoints, injection needles (inner diameter 0.5 μm, outer diameter 0.7 μm) (Eppendorf 5242.957.000) were loaded with 10 μL of warm injection solution and the needle was positioned in an Eppendorf Patchman NP2 and connected with an Eppendorf Femtojet Express microinjection controller. The injection rig was tested, and the bolus of injection solution produced at the end of the injection needle was measured in order to ensure an approximate volume of 0.5 nL (calculated using a sphere-volume formula). In order to adjust bolus volume, the pressure on setting on the Femtojet unit was changed. Once all parameters were verified, a few zebrafish embryos at either 23-hpf or 26-hpf were submerged briefly 0.01% MS-222 for anesthetisation and prevention of twitching. Anesthetized embryos were then transferred a new dish containing warm embryo medium placed under a Nikon SMZ1500 dissection microscope for injection. Injections were performed in the right eyes of all anesthetized fish (Figure 3.2). Following injections, fish were transferred to an incubator set at 28°C and monitored closely to ensure recovery (indicating by resumption of twitching motions). At the end of the injection day, all fish were transferred to glass cups containing zebrafish medium and raised as per the *Animal Husbandry* section above. The total number of fish injected at each treatment and timepoint combination is summarized below in Table 3.1. Detailed step-by-step methods are provided in the Appendix E.

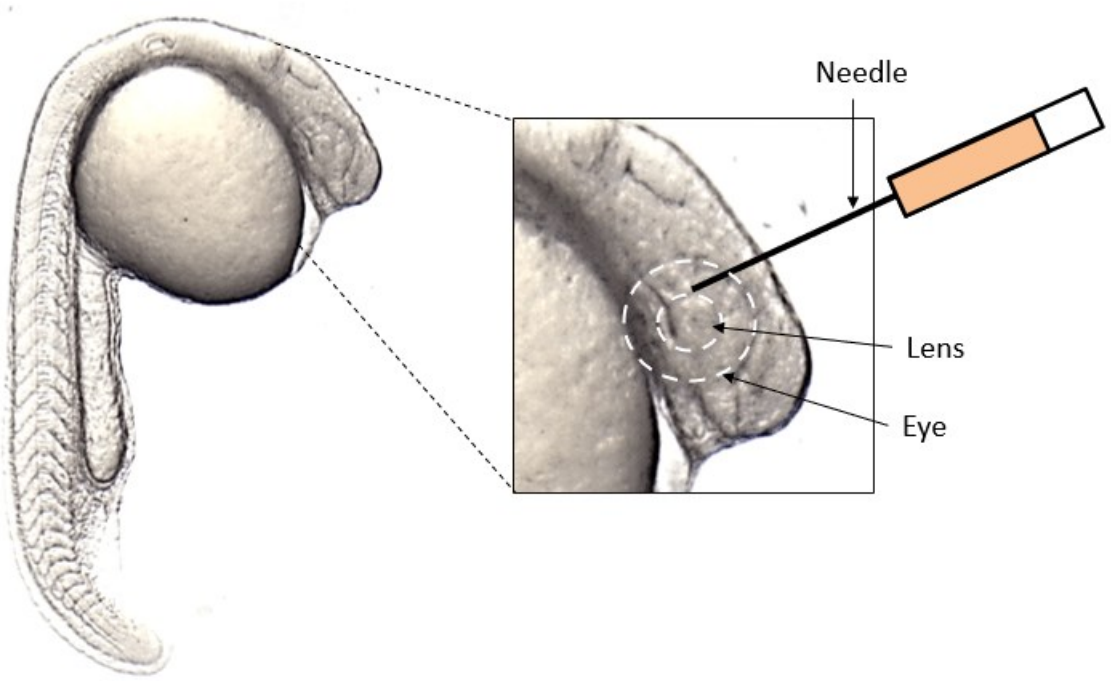

Figure 3.2. *Schematic of intravitreal injection of zebrafish at approximately 23-hpf.*

Table 3.1. *Total number of zebrafish injected at each timepoint and treatment combination. NT indicated non-treated fish, which did not receive injections (indicated by *).*

Inhibitor	Concentration	Injection Timepoint (hpf)	Number of Fish Injected (n)
NT	-	-	10*
DMSO	5%	23	12
		26	12
SSR	0.25 mM	23	20
		26	22
	0.5 mM	23	22
		26	20
LY	0.25 mM	23	20
		26	24
	0.5 mM	23	22
		26	25

3.2.4 Bone and Cartilage Staining

Upon reaching the experimental endpoint of 6.0 mm standard length (SL), injected zebrafish were euthanized via submersion in 0.1% MS-222. Tissue fixation was performed via submersion in 4% paraformaldehyde overnight at 4°C. On the following day, the fixed zebrafish were washed three times in 1X PBS and stored short-term (less than a week) in 1X PBS at 4°C.

In order to visualize both cartilage and ossified bone, doubling staining for bone and cartilage was performed (Walker & Kimmel, 2007). Zebrafish were dehydrated in 50% ethanol for 30 minutes. Following dehydration, zebrafish were submerged in a staining solution containing Alcian Blue and Alizarin Red and incubated overnight with gentle agitation. On the following day, stained fish were briefly rinsed in distilled water and bleached in a 1% potassium hydroxide, 1.5% hydrogen peroxide solution. Once the pigment of the eye was sufficiently bleached, zebrafish were processed through a series of glycerol/PBS solutions and eventually stored in 100% glycerol at room temperature. If zebrafish remained too blue (with a lot of background staining), they were allowed more time in the 50% glycerol/PBS solution for additional clearing. Detailed methods are provided in the Appendix E.

3.2.5 Scleral Cartilage and Cranial Cartilage Assessment

In order to understand the effects of intravitreal inhibitor injections on cartilages of the head, the scleral cartilage, as well as the epiphyseal bar, basihyal cartilage, and basicapsular cartilage were examined under a dissecting microscope. The scleral cartilage of each fish was assessed via examination of the ring's morphology (e.g., continuity, position, size) in comparison to non-injected eyes and the eyes of control fish. In order to verify the assessments made, a blind assessment was performed for a sub-sample of groups (i.e., n=9, non-treated; n=8, 23-hpf

DMSO; n=9, 26-hpf 0.5 mM SSR; and n=12 26-hpf 0.5 mM LY), in which another individual placed samples into petri dishes for examination by the researcher. This individual recorded the identity of each sample as the researcher made blind assessments. Blind examination data was later matched with each group examined and compared to earlier, non-blind examination data in order to assess the accuracy of the non-blind assessments (See Appendix B for details on blind assessment results). Additionally, further analysis of the epiphyseal bar was performed due to its interesting morphology when disrupted.

3.2.6 Epiphyseal Bar Morphometry

Differences in epiphyseal bar morphology were quantified using the SHAPE analysis package as previously described (Iwata & Ukai, 2002; Zinck et al., 2021). Images of the dorsal cranium of bone and cartilage-stained fish were collected using a Nikon SMZ1500 microscope equipped with a Nikon DS Fi2 camera using Nikon NIS BR software. The region of interest was outlined around the epiphyseal bar of each fish. The regions of interests were then turned into black and white 24-bitmap (.bmp) files and analyzed via Fourier shape analysis (Iwata & Ukai, 2002). Specifically, chain code (which encodes the contours of the outlined shape) was produced for each image using the ChainCoder program. Chain code was processed using the CHC2NEF program in order to generate normalized elliptical Fourier descriptors. A principal component analysis was performed with the descriptors in order to determine the major sources of morphological variation between the epiphyseal bars of the inhibitor treated and control zebrafish. Principal component analysis was conducted separately for the 23-hpf and 26-hpf injection timepoints, and thus separate principal components were obtained that account for the observed morphological differences induced via inhibitor injection.

The statistical significance of differences between principal component score clustering was assessed via one-way permutational multivariate analysis of variance (PERMANOVA) using the PAST (Paleontological Statistics) software. Scatterplots illustrating the principal component score clustering were produced using PRISM GraphPad software.

3.3. Results

3.3.1 Mortality rates are increased in inhibitor treated zebrafish.

The final survival rates of non-treated controls, DMSO injection-controls, and inhibitor-treated fish were recorded during the growth phase and are summarized below in Figure 3.3. Non-treated fish had a survival rate of 90%. Fish injected with the DMSO control solution had a final survival rate of 67 and 75% at 23-hpf and 26-hpf, respectively (Figure 3.3A, B). Fish injected with 0.25 mM LY had a final survival rate of 35% and 71% at 23-hpf and 26-hpf, respectively (Figure 3.3A, B). Fish injected with 0.5 mM LY at 23-hpf had a final survival rate of 23 and 52% at 23-hpf and 26-hpf, respectively (Figure 3.3A, B). Fish injected with 0.25 mM SSR had a final survival rate of 27 and 40% at 23-hpf and 26-hpf, respectively (Figure 3.3A, B). Finally, fish injected with 0.5 mM SSR at 23-hpf had a final survival rate of 15% and 39% at 23-hpf and 26-hpf, respectively (Figure 3.3A, B). In summary, this data illustrates an age-dependent effect on post-injection survival, as groups injected at the 26-hpf timepoint display consistently greater survival rates than their 23-hpf counterparts. Moreover, a dose-dependent effect of FGF and TGF-ß inhibition is likely at play. In most cases, groups that received the higher 0.5 mM inhibitor dose (regardless of type) had reduced survival rates within each timepoint. Overall, these results suggest that intravitreal injection had minor effects on survival relative to inhibitor treated groups, and that injection of FGFR and TGF-ß inhibitors resulted in overall decreases in survival among most groups.

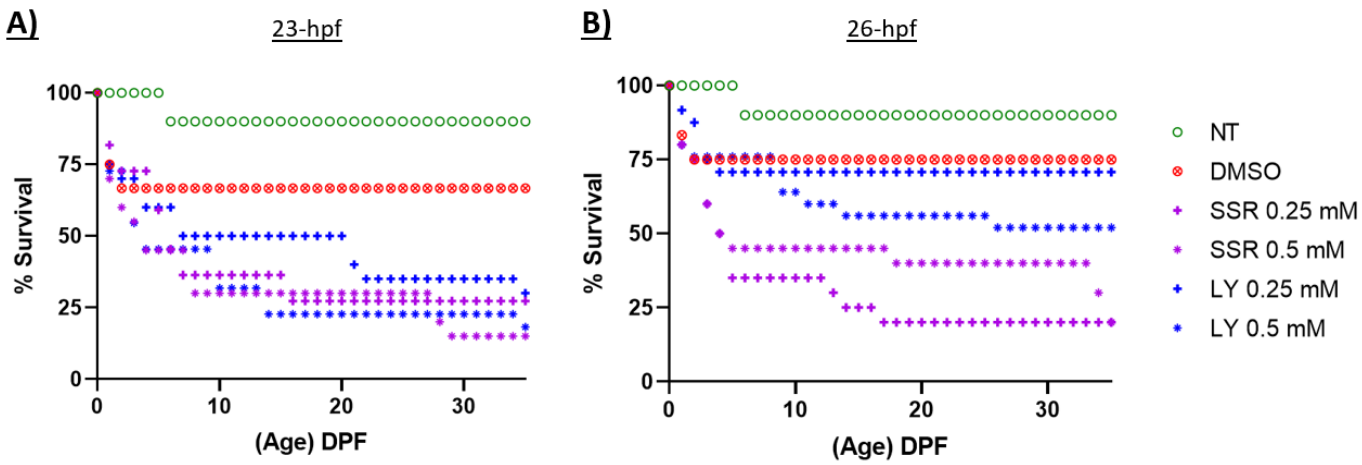

Figure 3.3. *Post-injection experiment survival rates during growth to 6.0 mm SL. A, Survival for zebrafish injected at the 23-hpf timepoint. B, Survival for zebrafish injected at the 26-hpf timepoint. NT means non-treated.*

3.3.2 Scleral cartilage morphology was unaffected by intravitreal injection.

In order to understand the roles of FGF and TGF-ß signaling in scleral cartilage induction, the scleral cartilage of fish that received intravitreal inhibitor injections was assessed. This data is shown in Figure 3.4. Interestingly, no abnormalities in scleral cartilage morphology were observed via assessment of whole-mount bone and cartilage stained zebrafish at any timepoint (Figure 3.4). The scleral cartilage of all fish that were inhibitor-treated at both 23-hpf and 26-hpf closely resembled the scleral cartilage of non-treated and DMSO control zebrafish (Figure 3.4C, D).

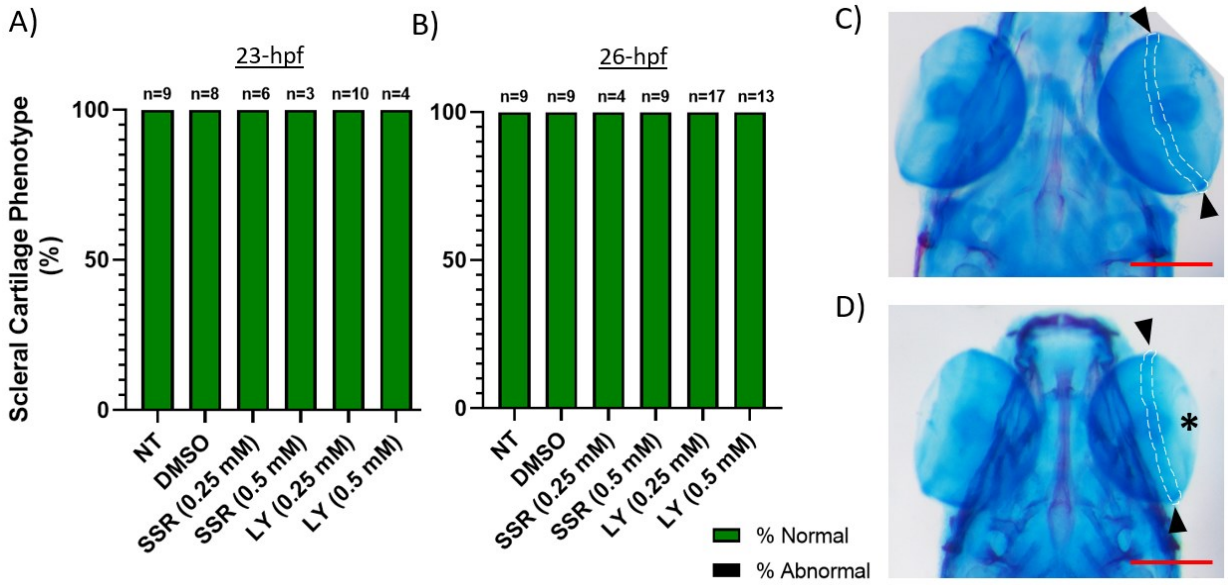

Figure 3.4. *Effects of intravitreal inhibitor injections on the scleral cartilage. A, B, percentage of zebrafish with normal vs. abnormal scleral cartilage morphology following injections at 23-hpf (A) and 26-hpf (B). Samples sizes for each treatment group are indicated above their respective bars. C, D, representative images of a non-treated zebrafish (C), and the 0.5 mM LY injection at 26-hpf (D) stained with Alcian blue and Alizarin red at 6.0 mm SL. Images show a dorsal view of the head (C, D). Injected eyes (right) are indicated by an asterisk. The scleral cartilage is indicated by an arrowhead. Scale bars (red) indicate 250 µm.*

3.3.3 Epiphyseal bar morphology was disrupted due to FGFR and TGF-ß inhibition.

In order to further understand the effects of intravitreal FGFR and TGF-ß inhibition on the POM, the morphology of the epiphyseal bar was assessed. Of the 23-hpf injection timepoint groups, 50% (n=3/6) of 0.25 mM SSR-treated fish, 100% (n=3/3) of 0.5 mM SSR-treated fish, 60% (n=6/10) of 0.25 mM LY-treated fish, and 25% (n=1/4) of 0.5 mM LY-treated fish presented abnormal epiphyseal bar morphologies compared to 0% (n=0/8) of DMSO-control zebrafish, and 11% (1/9) untreated fish (Figure 3.5A). Of the 26-hpf injection timepoint groups,

0% (n=0/4) of 0.25 mM SSR-treated fish, 44.4% (n=4/9) of 0.5 mM SSR-treated fish, 47.1% (n=8/17) of 0.25 mM LY-treated fish, and 61.5% (n=8/13) of 0.5 mM LY-treated fish presented abnormal epiphyseal bar morphologies compared to 0% (n=0/9) of DMSO-control zebrafish, and 1/9 (11%) of untreated fish (Figure 3.5B). This result demonstrates that the epiphyseal bar was affected by inhibitor injections with the most dramatic effects seen at the 23-hpf for most inhibitor concentrations. This abnormal morphology was typically denoted by asymmetrical curving of the epiphyseal bar, or a diagonal slant in orientation when viewed dorsally). Examples of normal and abnormal epiphyseal bar phenotypes can be found in Figure 3.5C, D.

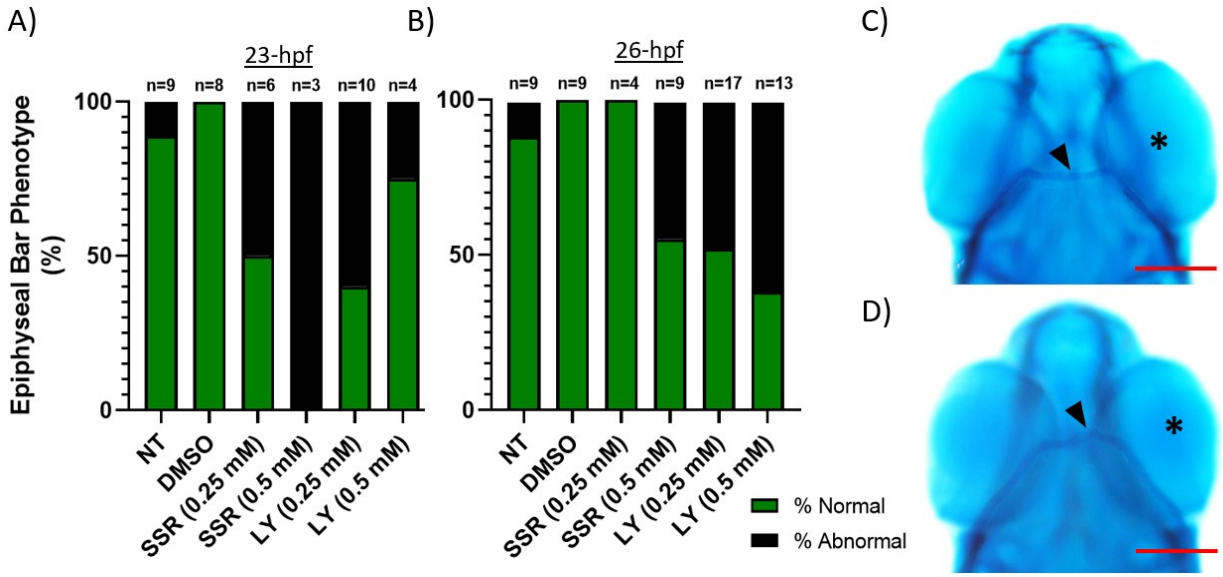

Figure 3.5. *Effects of intravitreal inhibitor injections on the epiphyseal bar. A, B, percentage of zebrafish with normal vs. abnormal epiphyseal bar morphology following injections at 23-hpf (A) and 26-hpf (B). Samples sizes for each treatment group are indicated above their respective bars. C, D, representative images of zebrafish that received the DMSO control injection at 23-hpf (C), and the 0.5 mM SSR injection at 26-hpf (D), stained with Alcian blue and Alizarin red at 6.0 mm SL. Images show a dorsal view of the head (C, D). Injected eyes (right) are indicated by*

an asterisk. The epiphyseal bar is indicated by an arrowhead. Scale bars (red) represent 250 µm.

3.3.4 Basihyal cartilage morphology is disrupted due to FGFR and TGF-ß inhibition.

In order to further understand the effects of intravitreal FGFR and TGF-ß inhibition on neural crest cells of the second pharyngeal arch, the basihyal cartilage was assessed for morphological abnormalities. Specifically, of the 23-hpf injection timepoint groups, 50% (n=3/6) of 0.25 mM SSR-treated fish, 33.3% (n=1/3) of 0.5 mM SSR-treated fish, 30% (n=3/10) of 0.25 mM LY-treated fish, and 0% (n=0/4) of 0.5 mM LY-treated fish presented abnormal basihyal cartilage morphologies compared to 12.5% (n=1/8) of DMSO-control zebrafish, and 11% (n=1/9) untreated fish (Figure 3.6A). Of the 26-hpf injection timepoint groups, 50% (n=2/4) of 0.25 mM SSR-treated fish, 33.3% (n=3/9) of 0.5 mM SSR-treated fish, 5.9% (n=1/17) of 0.25 mM LY-treated fish, and 23.1% (n=3/13) of 0.5 mM LY-treated fish presented abnormal basihyal cartilage morphologies compared to 11.1% (n=1/9) of DMSO-control zebrafish, and 11% (n=1/9) untreated fish (Figure 3.6B). Interestingly, abnormal morphologies, i.e., asymmetrical curving of the basihyal cartilage were found in DMSO controls and four of the five injection treatment groups, but at different incidence levels (Figure 3.6). The low-dose and high-dose SSR inhibitor treatment (FGFR inhibition) resulted in the highest frequency of basihyal cartilage disruption at both the 23-hpf and 26-hpf timepoints. Examples of normal and abnormal basihyal cartilage phenotypes can be found in Figure 3.6C, D.

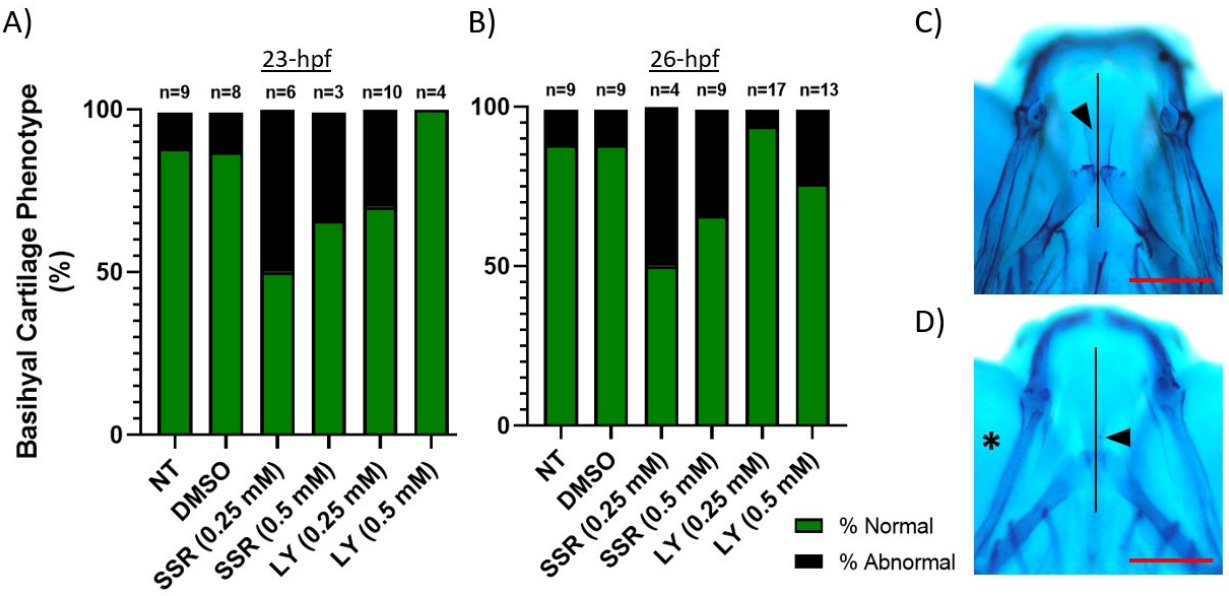

Figure 3.6. *Effects of intravitreal inhibitor injections on the basihyal cartilage. A, B, percentage of zebrafish with normal vs. abnormal basihyal cartilage morphology following injections at 23-hpf (A) and 26-hpf (B). Samples sizes for each treatment group are indicated above their respective bars. C, D, representative images of zebrafish that received no injection (C), and the 0.5 mM SSR injection at 26-hpf (D), stained with Alcian blue and Alizarin red at 6.0 mm SL. Images show a dorsal view of the head (C, D). Injected eyes (right) are indicated by an asterisk. The basihyal cartilage is indicated by an arrowhead. A vertical line indicates the center of the jaw skeleton (aligned with the ceratobrachial elements and Meckel's cartilage) in order to better illustrate the curved abnormal phenotype. Scale bars (red) indicate 150 µm.*

3.3.5 Basicapsular cartilage morphology is disrupted due to FGFR and TGF-ß inhibition.

In order to further understand the effects of intravitreal FGFR and TGF-ß inhibition the basicapsular cartilage was assessed morphological abnormalities. Specifically, of the 23-hpf injection timepoint groups, 0% (n=0/6) of 0.25 mM SSR-treated fish, 33.3% (n=1/3) of 0.5 mM SSR-treated fish, 40% (n=4/10) of 0.25 mM LY-treated fish, and 25% (n=1/4) of 0.5 mM LY-

treated fish presented abnormal basihyal cartilage morphologies compared to 12.5% (n=1/8) of DMSO-control zebrafish, and 0% (n=0/9) untreated fish (Figure 3.7A). Of the 26-hpf injection timepoint groups, 25% (n=1/4) of 0.25 mM SSR-treated fish, 0% (n=0/9) of 0.5 mM SSR-treated fish, 5.9% (n=1/17) of 0.25 mM LY-treated fish, and 15.4% (n=2/13) of 0.5 mM LY-treated fish presented abnormal basihyal cartilage morphologies compared to 11.1% (n=1/9) of DMSO-control zebrafish, and 0% (n=0/9) untreated fish (Figure 3.7B). Abnormal morphologies were denoted by asymmetry in the size of the basicapsular fenestration. Examples of normal and abnormal basihyal cartilage phenotypes can be found in Figure 3.7C, D. Interestingly, inhibitor treatment at the 23-hpf timepoint resulted in a higher frequency of basicapsular cartilage abnormalities than treatment at the 26-hpf timepoint.

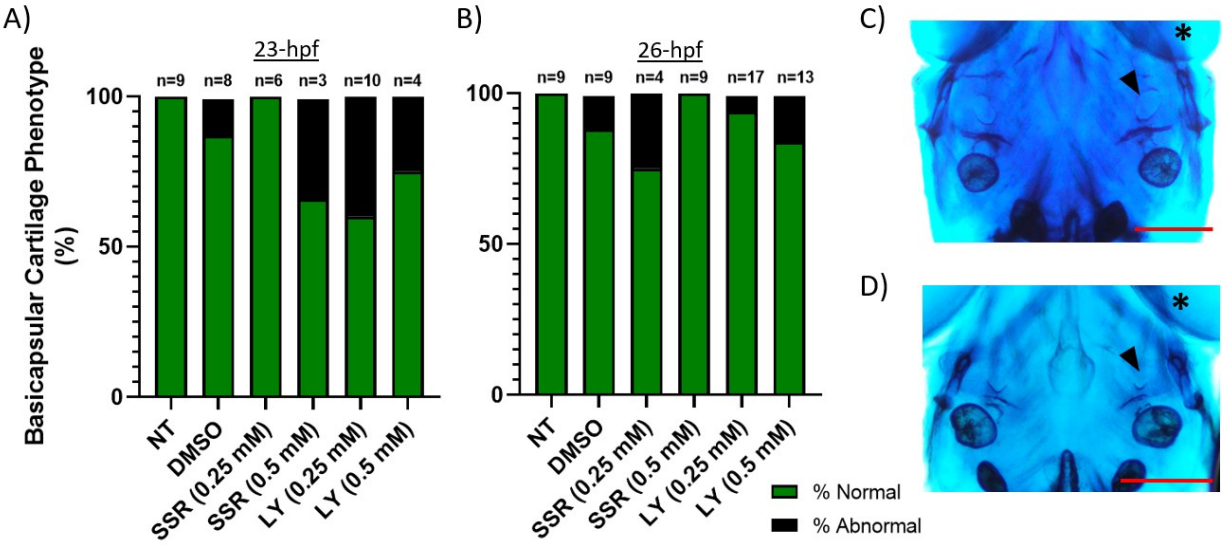

Figure 3.7. *Effects of intravitreal inhibitor injections on the basicapsular cartilage. A, B, percentage of zebrafish with normal vs. abnormal basicapsular cartilage morphology following injections at 23-hpf (A) and 26-hpf (B). Samples sizes for each treatment group are indicated above their respective bars. C, D, representative images of zebrafish that received the DMSO control injection at 26-hpf (C), and the 0.25 mM SSR injection at 23-hpf (D), stained with Alcian*

blue and Alizarin red at 6.0 mm SL. Images show a dorsal view of the head (C, D). Injected eyes (right) are indicated by an asterisk. The right basicapsular fenestration is indicated by an arrowhead. Scale bars (red) represent 200 µm.

3.3.6 Blind verification of assessments

In order to account for potential implicit biases in the cranial cartilage analysis, a sub-sample of fish, consisting of fish from the non-treated, 23-hpf DMSO control, 26-hpf 0.5 mM SSR, and 26-hpf 0.5 mM LY groups, were assessed blindly and compared to the initial assessments described above (Appendix B). No differences were found in the assessment of the scleral cartilage while some small differences in the incidence rates for the other cartilages were noted (Figure B.2, Appendix B). The nature of morphological assessments is inherently highly subjective, so this was not unexpected. These findings suggest that overall, the results presented in the above sections (non-blind assessments) are accurate and not heavily influenced by implicit biases. Thus, in order to better understand the effects of inhibitor treatment on epiphyseal bar morphology, an objective morphometric analysis was performed.

3.3.7 Intravitreal injections disrupted the epiphyseal bar differently at 23-hpf and 26-hpf.

In order to better understand the morphological abnormalities of the epiphyseal bar as a result of intravitreal inhibitor injection, a morphometric analysis was conducted for both the 23-hpf and 26-hpf treatment timepoints.

The results presented below will first summarize the findings of a morphometric principal component analysis on the 23-hpf injection timepoint groups, and then on the 26-hpf injection timepoint groups.

Seven principal components (PCs) described 92.14% of the cumulative variation in epiphyseal bar morphology of zebrafish injected at the 23-hpf timepoint (including non-treated fish) were found to be significant via PCA. The majority of this variation was described by the first four PCs (PC1, PC2, PC3, and PC4) which described 84.58% of the total cumulative variation (58.40%, 11.24%, 7.67%, and 7.06%, respectively). Thus, comparisons were made between groups using individual scores within the first four PCs.

For zebrafish injected at the 23-hpf timepoint, PC1 (58.4% of the variation) appears to describe variation in the inflexion of the epiphyseal bar. That is, variation from a straight element to either an anterior-curving (-2 SD) or posterior-curving element (+2 SD) (Figure 3.8B; x-axis) PC2 (11.24%) appears to describe the deposition of material on the posterior-medial (-2 SD) vs. the anterior-medial region (+2 SD) of the epiphyseal bar (Figure 3.8B; y-axis). When individual PC scores of controls and inhibitor-treated fish are examined in ordinate space, distinct differences in clustering can be observed (Figure 3.8C, D). Specifically, non-treated controls appear to cluster near the origin with a moderate degree of variation along the PC1 axis and relatively little variation along the PC2 axis, indicating natural variation in the curvature of the epiphyseal bar (Figure 3.8C, D; green circles). The DMSO-control injected zebrafish demonstrates similar clustering to non-treated fish, except for an individual on the negative PC1 axis (Figure 3.8C, D; red crossed-circles). Zebrafish that received either the 0.25 mM or 0.5 mM LY-364947 doses demonstrate somewhat similar clustering to non-treated controls, except that these fish display slightly greater variation along the PC2 axis than either control group. (Figure 3.8C; 0.25 mM. blue crosses; 0.5 mM blue asterisks). Finally, zebrafish that received the 0.25 mM SSR128129E treatment clustered similarly to non-treated fish, but separate from DMSO-controls, while those that received the 0.5 mM SSR128129E treatment demonstrate differential

clustering, while n=2/3 individuals clustering in the upper left quadrant (Figure 3.8D, dashed-circle). A one-way PERMANOVA used to identify statistically significant differences in PC score clustering indicated only one significant difference; between the 0.25 mM SSR treatment group and the DMSO-control group ($p<0.01$; Figure 3.8D). Exact p-values for all comparisons can be found in Appendix D. While PC1 and PC2 explain more than half of the observed variance in epiphyseal bar morphology among the 23-hpf injection timepoint groups, this variation appears to mainly be natural variation in the curvature of bar.

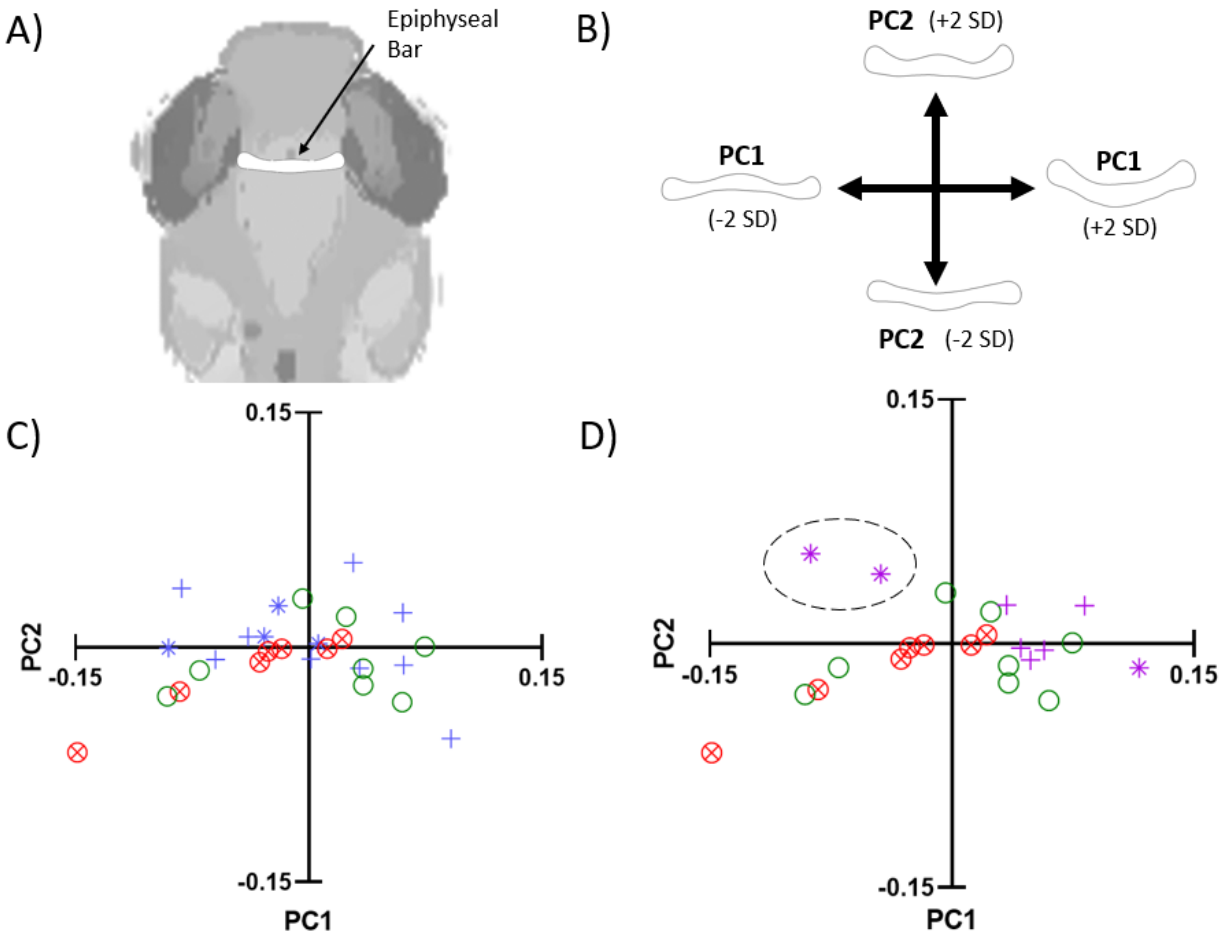

Figure 3.8. *Summary of epiphyseal bar principal component analysis for 23-hpf injection timepoint: PC1 vs. PC2. A, schematic illustrating the mean epiphyseal bar morphology of fish injected at 23-hpf (and non-treated fish). B, schematic illustrating the variation described by PC1 (x-axis) and PC2 (y-axis) within two standard deviations of the mean. C, D, scatterplots illustrating the distribution of individuals along the PC1 and PC2 axes. C, TGF-ß inhibited fish (treated with LY-364947) compared to controls. D, FGFR inhibited (treated with SSR128129E) compared to controls. Green circles indicate non-treated zebrafish, red crossed-circles indicate DMSO-controls, crosses indicate low dose (0.25 mM) treated zebrafish, and asterisks indicate high dose (0.5 mM) treated fish.*

In order to further characterize the variation in epiphyseal bar morphology of zebrafish injected at the 23-hpf timepoint, a similar analysis was performed with PC3 and PC4, which account for 7.67%, and 7.06% of the total cumulative variation, respectively (Figure 3.9). PC3 appears to describe variation in the thickness of the epiphyseal bar (Figure 3.9B, x-axis). PC4 appears to describe the presence of asymmetry in epiphyseal bar curvature (Figure 3.9B, y-axis). Similar to the analysis for PC1 and PC2, non-treated controls, DMSO-controls, and zebrafish that received either the 0.25 mM or 0.5 mM LY and SSR treatments demonstrated similar clustering about the origin (Figure 3.9C, D). However, two individuals treated with LY (one with 0.25 mM and the other with 0.5 mM) deviated from the main cluster, negatively along the PC4 axis (Figure 3.9C, dashed circle), indicating the presence of asymmetrical disruptions in epiphyseal bar morphology. Similarly, two individuals treated with 0.5 mM SSR demonstrated similar deviance from the main cluster (Figure 3.9D, dashed circle). A one-way PERMANOVA used to identify statistically significant differences in PC score clustering indicated only one significant difference: between the 0.5 mM SSR treatment group and the non-treated group

($p<0.05$). It should be noted that the difference between the 0.5 mM SSR treatment group and DMSO controls approached significance at the $\alpha=0.05$ level ($p=0.0592$). Exact p-values for all comparisons can be found in Appendix D. In summary, while the majority of inhibitor treated fish displayed epiphyseal bar morphologies similar to those of controls, this analysis demonstrates that disruptions were caused by FGFR inhibition via SSR treatment.

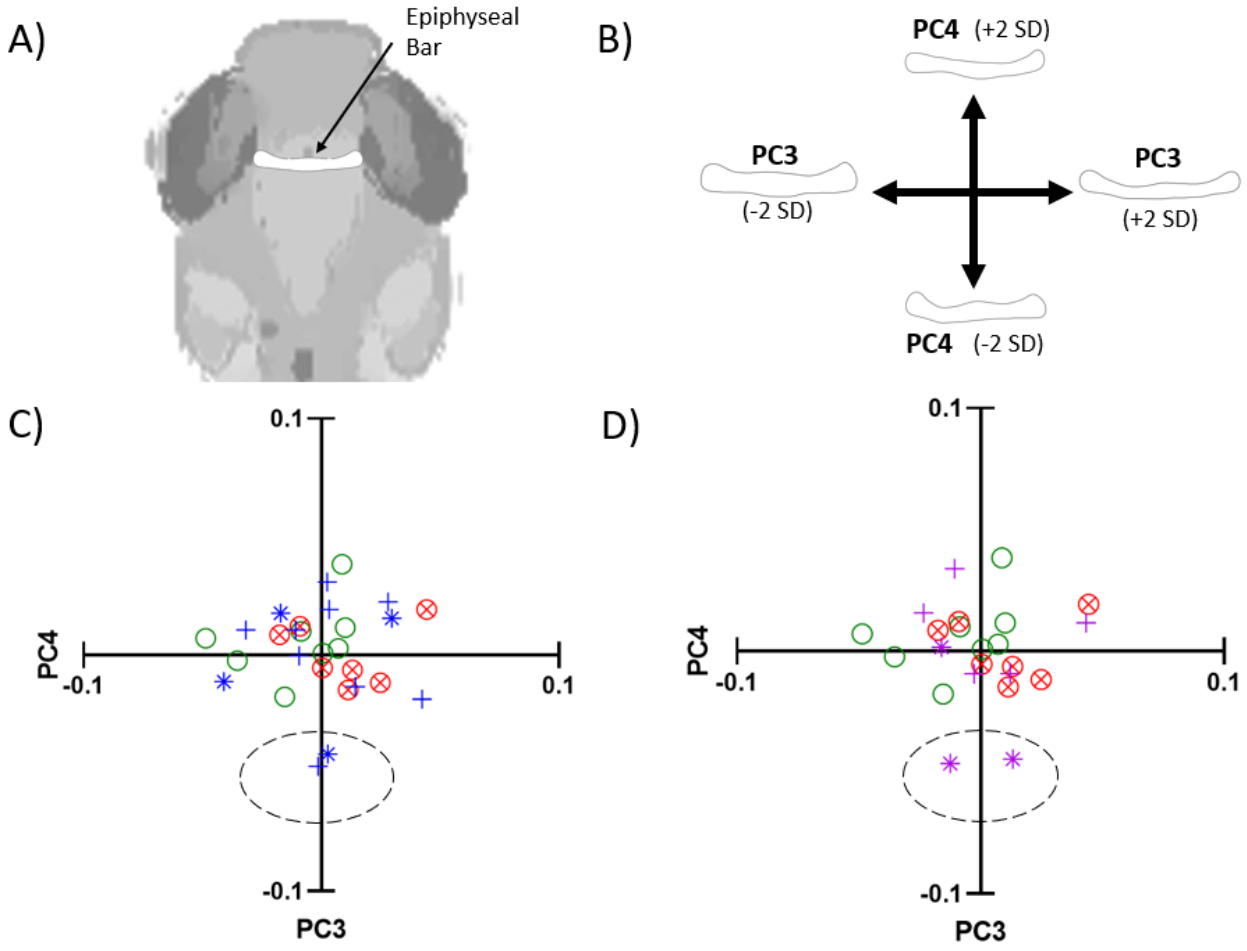

Figure 3.9. *Summary of epiphyseal bar principal component analysis for 23-hpf injection timepoint: PC3 vs. PC4. A, schematic illustrating the mean epiphyseal bar morphology of fish injected at 23-hpf (and non-treated fish). B, schematic illustrating the variation described by PC3 (x-axis) and PC4 (y-axis) within two standard deviations of the mean. C, D, scatterplots*

illustrating the distribution of individuals along the PC1 and PC2 axes. C, TGF-ß inhibited fish (treated with LY-364947) compared to controls. D, FGFR inhibited (treated with SSR128129E) compared to controls. Green circles indicate non-treated zebrafish, red crossed-circles indicate DMSO-controls, crosses indicate low dose (0.25 mM) treated zebrafish, and asterisks indicate high dose (0.5 mM) treated fish.

Seven principal components (PCs) which described 92.78% of the cumulative variation in epiphyseal bar morphology of zebrafish injected at the 26-hpf timepoint (including non-treated fish) were found to significant via PCA. The majority of this variation was described by the first four PCs (PC1, PC2, PC3, and PC4) which described 86.19% of the total cumulative variation (59.36%, 11.85%, 9.92%, and 5.06%, respectively). Thus, comparisons were made between groups using individual scores within the first four PCs.

For zebrafish injected at the 26-hpf timepoint, PC1 (59.36% of total variation) appears to describe variation in the inflexion of the epiphyseal bar. That is, variation from either a posterior-curving (-2 SD) or anterior-curving element (+2 SD) (Figure 3.10B; x-axis). PC2 (11.85%, of total variation), appears to describe variation in thickness of the epiphyseal bar (Figure 3.10B; y-axis). When individual PC scores of controls and inhibitor-treated fish are examined in ordinate space, distinct clustering patterns can be observed (Figure 3.10C, D). Specifically, non-treated controls appear to cluster near the origin with small degree of variation along the PC1 axis and little variation along the PC2 axis, indicating a small amount of natural variation in the curvature of the epiphyseal bar (Figure 3.10C, D; green circles). DMSO-control injected zebrafish demonstrates similar clustering to non-treated fish, but with a slight tendency towards the positive end of the PC1 axis (Figure 3.10C, D; red crossed-circles). Similarly, zebrafish that received either the 0.25 mM or 0.5 mM LY doses demonstrate similar clustering to control fish

but display greater variation along the PC1 axis than either of the control groups. (Figure 3.10C; 0.25 mM, blue crosses; 0.5 mM blue asterisks). Finally, zebrafish that received the 0.25 mM or 0.5 mM SSR treatment clustered similarly to both control groups but show increased variation along both the PC1 and PC2 axes are apparent for each concentration (Figure 3.10D; 0.25 mM. purple crosses; 0.5 mM purple asterisks). A one-way PERMANOVA did not identify any statistically significant differences in the PC1/PC2 clustering. Exact p-values for all comparisons can be found in Appendix D. Similar to the 23-hpf timepoints, PC1 and PC2 explain more than half of the observed variance in epiphyseal bar morphology. However, this variation appears to mainly be natural variation in the curvature of the epiphyseal bar.

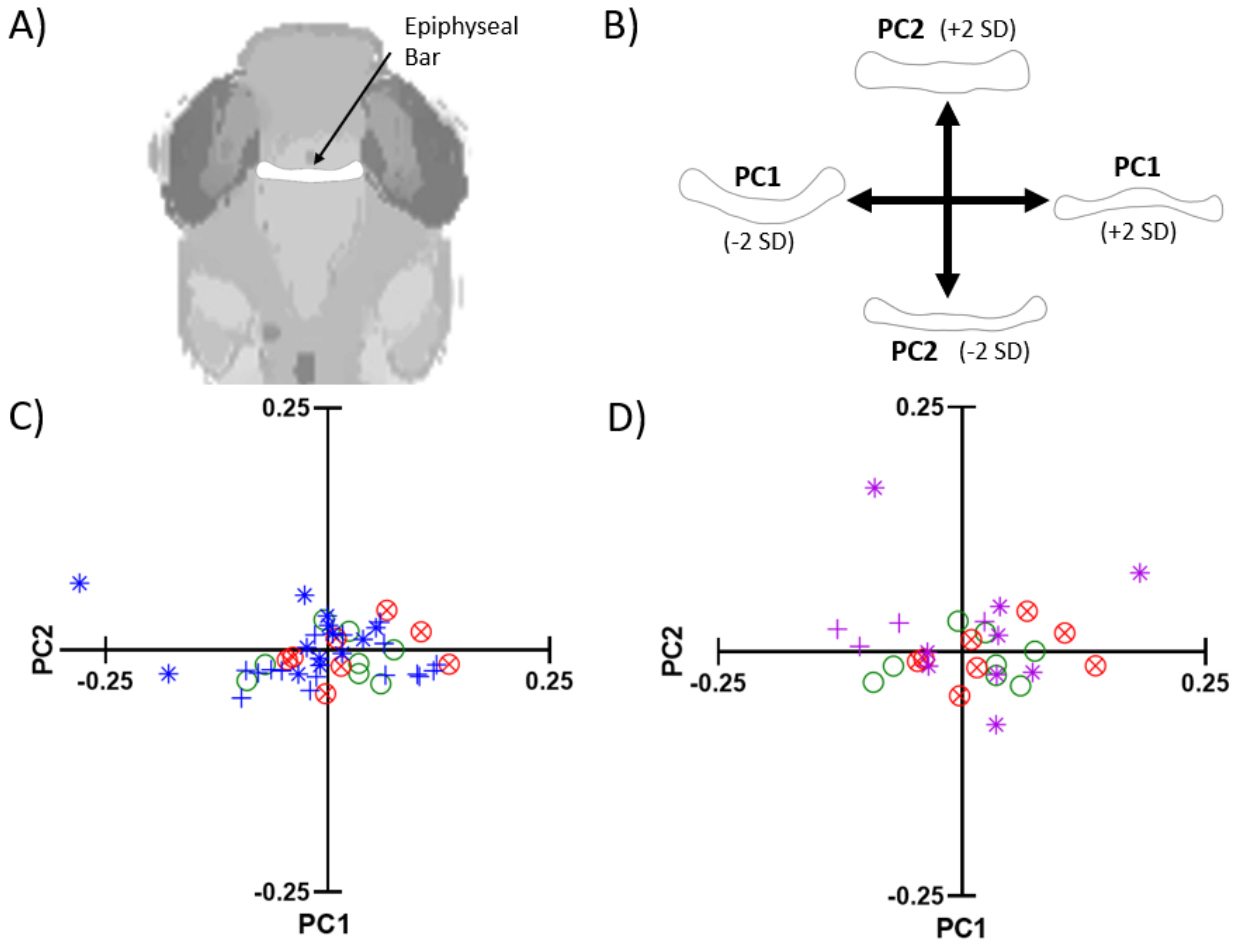

Figure 3.10. *Summary of epiphyseal bar principal component analysis for 26-hpf injection timepoint: PC1 vs. PC2. A, schematic illustrating the mean epiphyseal bar morphology of fish injected at 26-hpf (and non-treated fish). B, schematic illustrating the variation described by PC1 (x-axis) and PC2 (y-axis) within two standard deviations of the mean. C, D, scatterplots illustrating the distribution of individuals along the PC1 and PC2 axes. C, TGF-ß inhibited fish (treated with LY-364947) compared to controls. D, FGFR inhibited (treated with SSR128129E) compared to controls. Green circles indicate non-treated zebrafish, red crossed-circles indicate DMSO-controls, crosses indicate low dose (0.25 mM) treated zebrafish, and asterisks indicate high dose (0.5 mM) treated fish.*

In order to further characterize the variation in epiphyseal bar morphology of zebrafish injected at the 26-hpf timepoint, a similar analysis was performed with PC3 and PC4 (Figure 3.11). PC3 (9.92% of the total variation) appears to describe differences in thickness of the posterior-medial (-2 SD) vs. the anterior-medial region (+2 SD) of the epiphyseal bar, in addition to a slight right-unilateral bend (Figure 3.11B, x-axis). PC4 (5.06% of the total variation), appears to describe the presence of asymmetry in epiphyseal bar curvature, with variation from a left-side bend (-2 SD) to a right-side bend (+2 SD), indicating a morphological disruption caused by the unilateral injections (Figure 3.11B, y-axis). Similar to the analysis for PC1 and PC2, non-treated controls and DMSO-controls demonstrated similar clustering about the origin (Figure 3.11C, D). While the majority of zebrafish treated with LY at the 26-hpf timepoint clustered near the control groups, many individuals deviated from the main cluster towards the upper- and lower-right quadrants indicating a high degree of variation in epiphyseal bar morphology (with a tendency towards a unilateral right-bend) (Figure 3.11C; dashed circle). In contrast, SSR treated zebrafish demonstrated cluster highly similar to both control groups, with only a few individuals displaying variance along the PC3 axis. A one-way PERMANOVA identified no statistically significant differences in group clustering for PC3/PC4. While not statistically significant, it should be noted that the difference between the 0.5 mM LY treatment group and non-treated controls approached significance at the $\alpha=0.05$ level ($p=0.0664$). Exact p-values for all comparisons can be found in Appendix D.

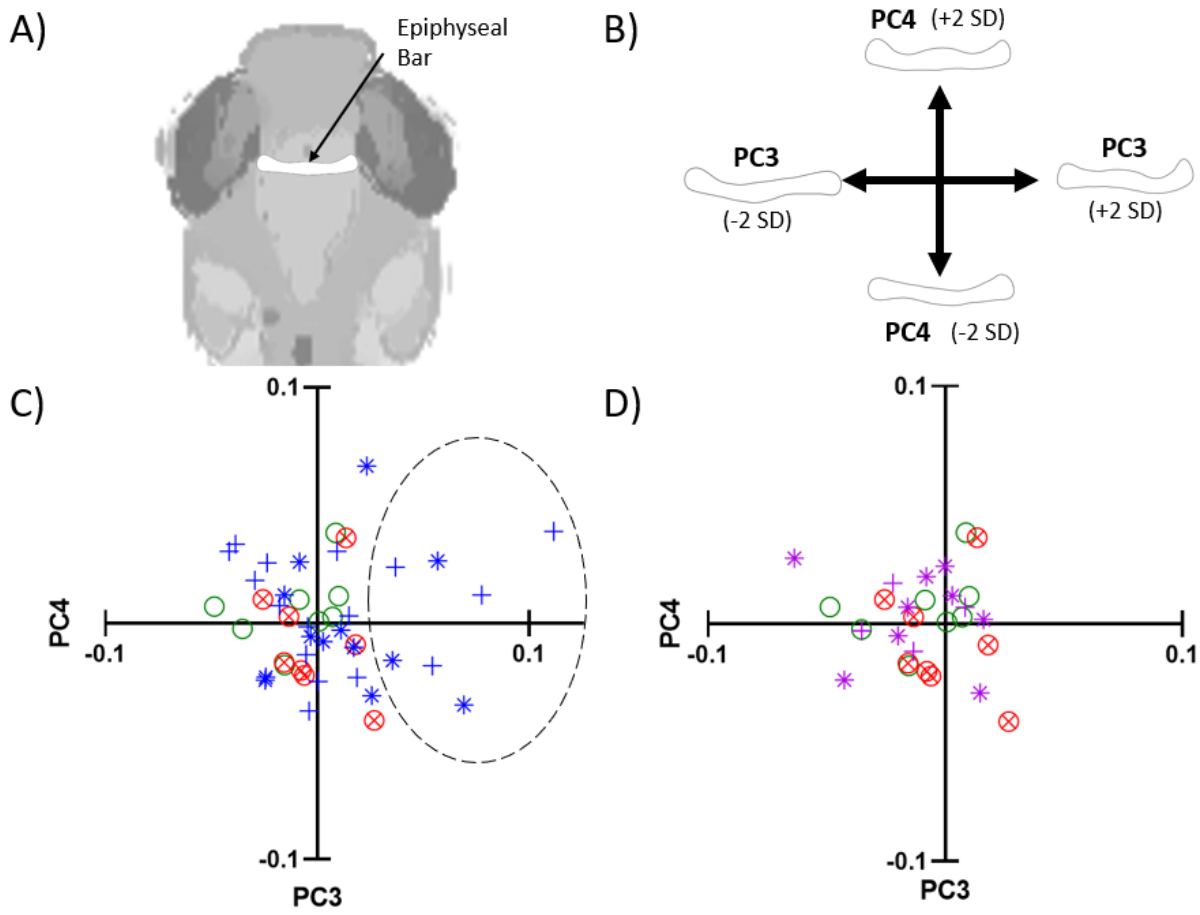

Figure 3.11. *Summary of epiphyseal bar principal component analysis for 26-hpf injection timepoint: PC3 vs. PC4. A, schematic illustrating the mean epiphyseal bar morphology of fish injected at 26-hpf (and non-treated fish). B, schematic illustrating the variation described by PC3 (x-axis) and PC4 (y-axis) within two standard deviations of the mean. C, D, scatterplots illustrating the distribution of individuals along the PC1 and PC2 axes. C, TGF-ß inhibited fish (treated with LY-364947) compared to controls. D, FGFR inhibited (treated with SSR128129E) compared to controls. Green circles indicate non-treated zebrafish, red crossed-circles indicate DMSO-controls, crosses indicate low dose (0.25 mM) treated zebrafish, and asterisks indicate high dose (0.5 mM) treated fish.*

In summary, while the majority of inhibitor treated fish displayed epiphyseal bar morphologies similar to those of controls, this morphometric analysis demonstrates a quantifiable effect on epiphyseal bar morphology due to injection with inhibitors for FGF and TGF-ß signaling. Specifically, an asymmetrical phenotype was described by PC4 in the 23-hpf analysis and PC3 in the 26-hpf analyses. The most striking result was observed in fish treated with LY (TGF-ß inhibitor) at 26-hpf (Figure 3.11C) in which several inhibited fish deviated from the main cluster along PC3.

3.4 Discussion

3.4.1 Intravitreal Injection Reduced Survival at Each Timepoint

The research presented in this chapter aimed to explore the effect of local inhibition of the FGF and TGF-ß signaling pathways on scleral cartilage development. Local inhibition was accomplished via intravitreal injections of SSR128129E and LY-364947. An increased rate of mortality was observed in each injection group in the days following injection. Overall, zebrafish injected with a DMSO control solution experienced higher rates of mortality than non-treated fish. Previous research regarding the toxicological effects of DMSO on zebrafish embryonic and larval survival have found harmful effects in terms of both survival (Schubert et al., 2014) and inflation of the anterior lobe of the swim bladder (Maes et al., 2012). However, these studies utilized a yolk microinjection (at the 1-2 cell stage) of approximately 4.0 nL of pure DMSO and a global treatment method (2.5% DMSO in the environmental water), respectively. Because of the difference in the method of administration, it is difficult to compare this with the results obtained in this study (which utilized injection of approximately 0.5 nL of 5% DMSO). Further research is needed to explore the differences between yolk microinjection and tissue microinjections of DMSO. It is hypothesized that the increased mortality rate observed in DMSO

control injection is likely due to needle penetration of the eye at very young stages. A sham-control was not conducted and should be conducted so that the effect of needle penetration (without injection of DMSO control solution) can be assessed.

Differences were noted between groups injected with a DMSO control solution and groups that received inhibitors for FGF and TGF-ß signaling. Interestingly, inhibition of FGF signaling via SSR-treatment consistently resulting in higher mortality rates than inhibition of TGF-ß signaling. SSR128129E has been shown to act as an extracellular allosteric inhibitor of FGFR1-4 function, specifically inhibiting internalization of FGFRs (Bono et al., 2013; C. Herbert et al., 2013). FGF/FGFR signaling plays a role in a myriad of non-skeletal developmental processes including vasculo- and angiogenesis (Nicoli et al., 2009; Kotini et al., 2021). Expansion of the early zebrafish vascular loop into the head region begins after approximately 24-hpf (Kaufman et al., 2015). Thus, inhibition of FGFR function at 23-hpf and 26-hpf may have disrupted the rostral expansion of vasculature. As the zebrafish's tissues become more complex, simple diffusion of yolk nutrients must be compensated by the circulatory system. Thus, it is likely that the early die-off observed after FGFR inhibition is due to disruption of vasculogenesis in the head.

TGF-ß inhibited zebrafish had similar mortality rates to FGFR/FGF inhibited zebrafish at 23-hpf but were less affected at 26-hpf. Alk-1, the TGF-ß receptor inhibited by LY-364947, plays a role in proliferation of endothelial cells during angiogenesis (Holderfield & Hughes, 2008). Thus, it is possible that the post-injection die-off causes by LY injection is similarly due to disruption of head vasculature development.

3.4.2 Inhibition produced no apparent effect on the scleral cartilage.

Previous bone morphogenetic protein inhibition experiments utilizing a global inhibition method failed to produce disruption of zebrafish scleral cartilage and concluded that a neuroprotective mechanism in the eye, namely the blood-retina barrier, may have prevented passage of inhibitor molecules to the eye from the blood (Isogai et al., 2001; Xie et al., 2010; Kaufman et al., 2015; Zinck et al., 2021). Thus, a more direct and localized approached was chosen for the current study, in the form of intravitreal injections. Surprisingly, no disruptive effects were observed in the scleral cartilage of zebrafish that underwent FGFR/FGF or TGF-ß signal inhibition. Importantly, disruptive effects were observed in other cartilages of the head, indicating the effectiveness of our inhibitor treatment. Moreover, differences in disruption frequency were observed between the 23-hpf and 26-hpf injection timepoints in both the epiphyseal bar, basihyal cartilage, and basicapsular cartilage, indicating a clear time-dependent effect. This aligns with the differential emergence timepoints for each cartilage structure (Figure 3.1). It is likely that the epiphyseal bar emerges slightly after the scleral cartilage, though this has not been confirmed. If true, it is possible that injections at earlier timepoints would produce disruption of the scleral cartilage. Earlier timepoints were attempted in optimization experiments but lead to higher rates of mortality (Appendix B). Thus, in order to explore this possibility, further optimization of injections at earlier timepoint would be required.

In addition to timing, a dosage-dependent effect was observed for inhibitor treatments at each injection timepoint. For example, such an effect suggests that the inhibitors were at an insufficient concentration to disrupt scleral cartilage induction or morphogenesis, however increasing concentrations will likely increase mortality rates. While no obvious abnormalities were apparent via whole-mount bone and cartilage staining in the scleral cartilage, it is possible

that the microscopic structure was affected. Thus, examination of the scleral cartilage via histological section paired with Hall-Brunt Quadruple staining may elucidate any potential disruptions in terms of scleral cartilage depth, cell-count, cell size, and cell morphology. In the case that no effect will be found after further analysis, which would suggest that scleral cartilage induction may be occurring at a different point in development than we had originally hypothesized (discussed below and in Chapter 4).

3.4.3 Differential effects across neural crest cell sub-populations.

Despite seemingly no effect on scleral cartilage development, distinct morphological disruptions were observed in other chondrocranial elements. The most striking of these disruptions was found in the epiphyseal bar. Interestingly, the epiphyseal bar shares a progenitor pool with the scleral cartilage, namely the POM (albeit a sub-population of the POM), and develops at approximately the time of the scleral cartilage (Figure 3.1) (Klymkowsky et al., 2010; Kague et al., 2012; Williams & Bohnsack, 2020). Moreover, visual examination paired with morphometric analysis confirmed the unilateral nature of the epiphyseal bar disruption that arose via TGF-ß inhibition (SSR or LY). This asymmetrical effect confirms that inhibition was localized unilaterally, on the side of the injection. Additionally, this result confirms that the inhibitors were able to diffuse through the optic cup tissues in order to affect the periocular mesenchyme.

The observed disruption in several chondrocranial elements provides the opportunity to discern which distinct progenitor cell populations were affected via FGF/FGFR and TGF-ß signal inhibition. As previously mentioned, the scleral cartilage and epiphyseal bar are derived from the POM (Kague et al., 2012; Williams & Bohnsack, 2020). Interestingly, only the

epiphyseal bar presented morphological disruptions following inhibitor injection. The POM makes contact with the surface of the optic cup between 23-hpf and 24-hpf. Following its establishment around the eye, a sub-population of POM migrates towards the dorsal aspect of the head in order to form many of the dorsal neurocranial elements such as the epiphyseal bar (Williams & Bohnsack, 2020). Meanwhile, a portion of the cells in the remaining POM pool will go on to condensations on the outer surface of the optic cup (i.e. lateral to the RPE), forming the sclera and later the scleral cartilage (Kague et al., 2012; Williams & Bohnsack, 2020). Thus, it is likely that the differential effects observed between the scleral cartilage and epiphyseal bar observed in this study are due to differences in the timing of signaling inducing these structures. During the continued migration of the dorsal-migratory POM, it is possible that additional inductive signals are received that further differentiate the dorsal-migratory population from the remaining POM. It is possible that our inhibition experiments disrupted these later signals involved in the induction of the epiphyseal bar, leading to the observed disruptions.

Interestingly, the murine dura mater is also known to secrete TGF-ß, FGFs, and BMPs, which are thought to regulate calvarial development (Dasgupta et al., 2019). While mammals possess meninges composed of three distinct layers around the brain, teleost fish posses only one layer known as the primitive meninx (Kondrychyn et al., 2013). Little is known about the development of the primitive meninx, including the timing of its appearance. However, it is possible that inhibition of FGF and TGF-ß signaling in the meninx during dorsal POM migration, the inhibition of which, resulted in the observed epiphyseal bar phenotype.

The basihyal cartilage is derived of slightly more posterior cranial neural crest cells, specifically of the second (hyoid) pharyngeal arch (Williams & Bohnsack, 2020). These cells originate from the posterior mesencephalon and anterior rhombencephalon (Williams &

Bohnsack, 2020). Our results indicate regulatory roles for both FGF/FGFR and TGF-ß signaling in basihyal cartilage morphogenesis. However, a more consistent effect was observed following FGFR inhibition via SSR injection. Utilizing morpholino knockdown, Walshe & Mason (2003), previously demonstrated a requirement for *FGF3* and *FGF8* signaling in the formation of the viscerocranium (Walshe & Mason, 2003). Interestingly, it was shown that *FGF3/8* transcripts were expressed in the pharyngeal endoderm associated with the developing jaw between 16-hpf and 30-hpf. In contrast to the current study, Walshe & Mason (2003) caused disruption in a majority of jaw elements derived from multiple pharyngeal arches. The differences between this previous work and the current study may be explained by the later timepoints used for injections, the local nature of the treatments, and by potential dose-dependence. The inhibitor injections performed in this study were conducted at timepoints after migration of neural crest cells into the pharyngeal arches (Yelick & Schilling, 2002; Klymkowsky et al., 2010; Williams & Bohnsack, 2020). Thus, it is likely that the morphological disruption produced in the basihyal cartilage in this study is due to later patterning processes that occur after neural crest cells reach the hyoid arch, after the cells have been induced to form cartilage.

The basicapsular cartilage is likely of mixed cranial neural crest cells and mesodermal origin (Kague et al., 2012; Mongera et al., 2013). Interestingly, more consistent disruption (typically observed as alteration in the diameter of the basicapsular fenestration) was observed in the earlier, 23-hpf timepoint groups for each inhibitor. Effects were observed at a similar frequency between the DMSO control injection group and multiple inhibitor injection groups, suggesting that the observed disruptions are likely due to or shadowed by effects due to needle penetration, or perhaps the presence of DMSO. This is a peculiar finding due to the relatively large physical separation between the eye and the basicapsular cartilage. The disruptions

observed in the basicapsular cartilage typically involve alteration of the diameter of the basicapsular fenestration, thus it is possible that a growth process such as pre-chondrocyte proliferation was disrupted due to needle penetration. However, this possibility was not further explored due to the scope of this study.

3.4.4 Epiphyseal Bar Disruption may be Useful in Studying Frontal Bone Development.

Interactions between the epiphyseal bar and frontal bone have been documented following treatment with retinoic acid (Jeradi & Hammerschmidt, 2016). Specifically, treatment with retinoic acid resulted in degeneration of the frontal bone in a region directly superior to the epiphyseal bar. Examination via tartrate-resistant acid phosphatase (TRAP) staining indicated active resorption of epiphyseal bar cartilage, in addition to the frontal bone (Jeradi & Hammerschmidt, 2016). While the research conducted by Jeradi & Hammerschmidt (2016), focused on a stage of life when the calvarium had already formed, it exemplifies the relationship between the epiphyseal bar and the frontal bone.

Ossification of the zebrafish paired frontal bones initiates bilaterally at the triangular junction of the epiphyseal bar and the anterior and posterior taeniae marginalis, resulting in a small triangle of intramembranous bone (Topczewska et al., 2016). Similarly, the ossification centre of the paired parietal bones directly overlies a region dense in cartilage, namely of the auditory capsule (Cubbage & Mabee, 1996; Topczewska et al., 2016). This close anatomical relationship between mature cartilage of the chondrocranium and the developing calvaria suggests a potential role for cartilage in the development of the calvarium. Strong evidence exists to suggest that calvarial development is dependent on inductive signaling from the meninges in mice (Jiang et al., 2002; Vivatbutsiri et al., 2008; Dasgupta et al., 2019). However, calvarial

induction is not well understood in the zebrafish, which possess only a rudimentary meninx (Kondrychyn et al., 2013). With this, it would be interesting to investigate the emergence of the frontal bones in zebrafish with disrupted epiphyseal bar morphology and position. That is, to repeat the injections conducted in this research in order to reproduce the disruption caused on the epiphyseal bar. The development of the frontal bone could then be examined using a variety of methods such as bone and cartilage staining or transgenics that allow for visualization of osteoblasts (e.g. bglap:GFP). Such an experiment could further elucidate the relationship between the epiphyseal bar and the development of the frontal bone.

3.4.5 Conclusion

In conclusion, intravitreal inhibitor injection did not produce the hypothesized disruptive effect on zebrafish scleral cartilage. However, several effects in other cranial cartilages, including the epiphyseal bar which shares origin with the scleral cartilage. Differential effects were observed between the epiphyseal bar and scleral cartilage possibly because the epiphyseal bar arises from a later-diverging POM subpopulation. Moreover, it is possible that variation in the effectiveness of inhibitor injection is due to slight differences in the placement of the injection solution within the eye (i.e., depending on the depth of needle upon insertion). In order to further understand any potential effects that were not apparent via whole-mount staining, a histological analysis of inhibitor treated scleral cartilage should be performed. Additionally, sham injections (i.e., insertion of a needle without any injection), should be performed in order to understand effects that may develop strictly from needle penetration. Such an experiment may better explain the effects observed on the basicapsular cartilage.

Chapter 4: Discussion

4.1 Summary of Research Findings.

The overall objective of this study was to understand the development and morphology of scleral cartilage in teleosts. Little research has been conducted on teleost scleral cartilage, in terms of both its morphology and development. Thus, this thesis aimed to shine a light on these factors via both descriptive and experimental methods. Before an in-depth discussion of my findings, a summary of the results of this thesis are presented.

In order to determine the pattern of scleral cartilage induction and growth in teleosts, a histological analysis was performed (Chapter 2). It was hypothesized that scleral cartilage induction would first occur in the sclera near the anterior most extent of the optic cup tissues (ora serrata) because this appeared to be the location of the SC in fish with narrow rings. It was further hypothesized that following emergence of the scleral cartilage, growth would continue in the posterior direction in fish with deeper cartilages. Results show differences in the timing of scleral cartilage emergence and growth were observed between the fish with narrow scleral cartilage rings, namely the zebrafish (*D. rerio*), and surface tetra (*A. mexicanus*), as well as the cave tetra (*A. mexicanus*), which displays a deeper ring. Theses differences in the timing of scleral cartilage emergence and growth suggest differences in the temporal regulation of scleral cartilage development amongst these fish. Interestingly, the differences observed in scleral cartilage depth closely resembled differences in the cell-count of scleral cartilage chondrocytes, indicating that scleral cartilage depth and growth is mainly a factor of cell-count and thus, proliferation. In order to understand if cell-count is the only factor with a role in scleral cartilage depth, an examination of cell-size was performed between the tetra morphs, which revealed that

the scleral cartilage chondrocytes in the cave tetra were significantly larger than those in the surface tetra. This finding indicates a divergence in the regulation of scleral cartilage chondrocyte hypertrophy during the relatively short (i.e., 20,000 year) separation of the surface and cave tetras (discussed in Section 2.4.2). Further research is required to understand how this change in cartilage patterning arose.

In addition to the differences observed between cartilage morphologies, unexpected variation in the positioning and depth of the scleral cartilage ring within these fish species/morphs were observed. Specifically, the position of the scleral cartilage ring around the optic cup differed between the rostral and caudal regions, and regional differences in scleral cartilage depth were observed between the rostral and caudal regions. These results suggest regionally specific regulation of scleral cartilage development. Such regional differences may be due to heterogeneity in the POM (in terms of the expression profile of genes involved in the mesenchymal and condensation stages of chondrogenesis) upon its establishment around the eye (Meulen, 2021; Van Der Meulen et al., 2020) as discussed in Section 2.4.4.

In order to determine the role of FGF and TGF-B signaling in scleral cartilage development, intravitreal injections were performed with inhibitors for both signaling pathways (Chapter 3). It was hypothesized that local inhibition of FGFRs or TGF-B IR (i.e., Type-I TGF-ß receptor) would lead to disruption of scleral cartilage morphology. This hypothesis was based on the possibility that an epithelial-mesenchymal interaction takes place between the RPE and the POM, leading to induction of the scleral cartilage. Results show that there are no apparent disruptions in scleral cartilage morphology after intravitreal inhibition of TGF-ß and FGF signaling (discussed in Section 3.4.2). However, striking morphological disruptions were apparent in other chondrocranial elements, as discussed in Section 3.4.3. Of particular interest

are the differential effects observed between the scleral cartilage and the epiphyseal bar caused by inhibition of either FGFRs or TGF-ß IR, due to their shared progenitor pool (i.e., the POM) as discussed in Section 3.4.3.

4.2 Scleral cartilage and the Retinal Pigment Epithelium.

Limited research on scleral cartilage induction has been conducted in any vertebrate. After understanding the morphological variation of the scleral cartilage in selected teleosts, a major goal of this project was to elucidate the potential role played by the RPE in scleral cartilage induction in teleosts. It was our goal to understand if the RPE could possibly induce the scleral cartilage after determining that the scleral cartilage grows anterior-to-posteriorly. Additionally, if the RPE induces the scleral cartilage, why is there not a uniform anatomical relationship between the scleral cartilage and RPE?

A comparative assessment of the timing of scleral cartilage induction through to differentiation in the chicken and zebrafish is important, considering in particular that these processes occur during embryogenesis in the chicken compared to post-embryogenesis in the zebrafish. In broad terms, scleral cartilage induction involves migration of cranial neural crest cell to the periocular region where they establish the POM. Upon establishment, the cells congregate to from a pre-chondrogenic condensation and differentiate to form matured cartilage (Figure 4.1A). In the chicken, scleral cartilage is first apparent at HH33 (E8), while a prechondrogenic mesenchymal condensation is apparent only at approximately HH24 (E4) (Figure 4.1B). Expression of *Aggrecan* can first be observed at HH26 (E5), which denotes the initiation of cartilage differentiation (Figure 4.1B) (Thompson et al., 2010). Thus, a period of four days is required between the aggregation of POM and the emergence of differentiated

cartilage in the chicken, and importantly, a period of approximately 24 hours elapses between condensation development and differentiation.

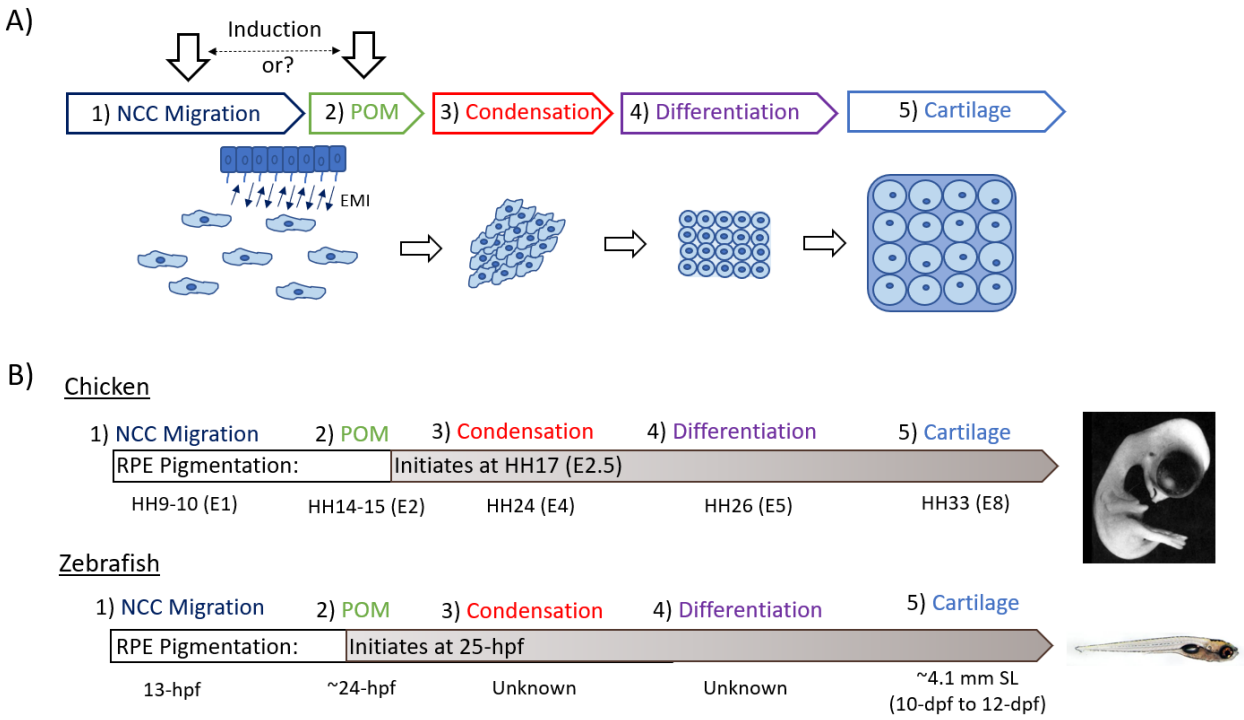

Figure 4.1. *Stages of cartilage development and their correspondence to development of the retinal pigment epithelia of chicken and zebrafish. A, Schematic illustrating the stages of scleral cartilage chondrogenesis. Potential timepoints for scleral cartilage induction indicated by black arrows. B, Timeline of scleral cartilage developmental events (associated with A), specific to the chicken and zebrafish. RPE pigmentation period is indicated by grey-brown arrows. NCC, neural crest cell; POM, periocular mesenchyme.*

Before discussing my own findings, it is important to revisit the work conducted in the chicken, *Gallus gallus*. As previously mentioned in Chapter 1, investigations using the chicken embryo have indicated a role for the retinal pigment epithelium RPE in scleral cartilage induction (Wedlock & McCallion, 1969; Newsome, 1972; Stewart & McCallion, 1975;

Thompson et al., 2010). In the latter study, conducted by Thompson et al. (2010), *in vivo* grafting experiments of chicken RPE to head mesenchyme demonstrated that RPE was sufficient for cartilage induction. Additionally, it was demonstrated that enucleation (that is, removal of the optic cup) at HH12-14 (E2), resulted in an absence of scleral cartilage in the POM (Thompson et al., 2010). It is important to note the timing of these experiments.

Typically in the chicken, RPE development occurs gradually throughout embryonic development, with specification occurring with evagination of the optic cup at HH10 (~E1) and intense pigmentation of the RPE occurring at HH25-26 (E4.5-5; Figure 4.1B) (Stroeva & Mitashov, 1983; Muller et al., 2007). Thompson et al. (2010), demonstrated *in vivo* expression of *CART1* and *SOX9* (markers of pre-committed cartilage and condensations, respectively) in the POM adjacent to the RPE beginning at HH18 (E3), several days prior to the complete differentiation of the RPE. However, *in vivo Aggrecan* expression was not identified until HH26 (E5). Aggrecan is marker of chondrocyte differentiation suggesting that scleral cartilage differentiation was initiated by this stage. Thus, it is possible that a condensation is present at HH18, while cartilage differentiation initiates at HH26 (leading to a full cup of scleral cartilage at HH33 (E8)) (Figure 4.1).

In their grafting experiments, Thompson et al. (2010), grafted HH18 and HH19 RPE to head mesenchyme (that doesn't form cartilage *in vivo*), eliciting expression of the genes mentioned above (namely, *CART1, SOX9*, and *Aggrecan*), and later, cartilage development. However, at this timepoint (approx. E3) the RPE is still in an early phase of its development and thus is still an immature epithelium that has likely not undergone a reduction of its inductive potential (Hall, 1981; Stroeva & Mitashov, 1983; Muller et al., 2007). It is not surprising that signaling from an immature epithelium early in the process of its differentiation was able to

induce chondrogenesis in cranial neural crest cells, which are generally competent to form cartilage under the direction of signals such as the BMP pathway (Hall & Tremaine, 1979; Ekanayake & Tuan, 1994; Yang et al., 2021). Therefore, while the Thompson et al. 2010 study concluded a role of the RPE in scleral cartilage induction, this interpretation may be incorrect due to the age of the grafted tissues used. In the earlier studies investigating the role of chicken RPE in scleral cartilage development *in vitro*, similarly young RPE transplants are utilized as well as older RPE, up to HH25 (Wedlock & McCallion, 1969; Newsome, 1972; Stewart & McCallion, 1975). However, these experiments paired RPE with much younger (e.g., HH17-19) POM in chorioallantoic membrane grafts and are thus not representative of *in vivo* scleral cartilage induction, which would occur between similarly aged tissues. In order to better understand the relationship between the RPE and scleral cartilage induction in chicken, an *in vivo* grafting experiment similar to that of Thompson et al. (2010), should be repeated that utilizes a series of older, and thus more differentiated RPE transplants. This would more clearly elucidate any potential role of the RPE in scleral cartilage induction. In conclusion, the interpretation that the RPE may play a role in cartilage induction in the chicken may not be correct.

As previously described in this thesis, little is known about the onset of scleral cartilage development in teleosts. Previous studies in zebrafish have suggested that scleral cartilage emergence occurs by 4.1 mm SL (Figure 4.1B), a timepoint by which the larval zebrafish is actively feeding independently (Zinck et al., 2021). The data presented in Chapter 2 of this thesis suggests that some variability is present in the timing of scleral cartilage emergence between individual zebrafish, however, scleral cartilage did appear near the 4.1 mm SL stage (or ~10-dpf to 12-dpf). It is currently unclear how long the condensation-phase is prior to this differentiated

cartilage (Figure 4.1B). An examination of *SOX9* expression in the pre-chondrogenic condensation of zebrafish prior to scleral cartilage emergence via *in situ* hybridization would be a valuable method in elucidating the timeline of zebrafish scleral cartilage development and may aid in narrowing down the timepoint at which inductive signaling is occurring. This knowledge, in conjunction with cranial neural crest cell migration data, will narrow down the developmental window in which induction is occurring. Understanding when this window occurs may suggest alternative candidate epithelia in scleral cartilage induction and will allow for future research to more closely analyze the mechanisms that regulate interspecific difference in scleral cartilage morphology.

In the teleost eye, the relationship between the RPE and scleral cartilage appears to be under intense positional regulation. The data presented in Chapter 2 of this thesis illustrates a conserved tendency for the scleral cartilage ring to abut the RPE at a slight angle, with the scleral cartilage of the caudal region extending over the anterior boundary of the optic cup tissues (i.e., the ora serrata). Assuming the scleral cartilage is induced in the anterior portion of the eye where it emerges, the non-uniform relationship between teleost scleral cartilage and the RPE suggests that the RPE may not be the inducing epithelium involved in scleral cartilage development, as uniform development of the scleral cartilage would be expected around the anterior RPE. Additionally, we must consider interspecific differences in scleral cartilage depth as a function of growth. This study identified that scleral cartilage grows in an anterior-to-posterior manner. If induction occurs only in the anterior region (perhaps due to a specific signaling environment near the ora serrata), depth may increase via unidirectional expansion, characteristic of chondrocyte proliferation. However, if the scleral cartilage is induced via inductive signals that emanate from the RPE uniformly, an inhibitory signal would be required to restrict the scleral cartilage to

emerge from the anterior region. In order to clarify the relationship between the teleost RPE and scleral cartilage, a grafting experiment could potentially be performed with teleost RPE, similar to those conducted in the chicken embryo (Newsome, 1972; Stewart & McCallion, 1975; Thompson et al., 2010). However, this is unlikely feasible with currently accessible technologies, given the small size of the teleost eye during these early developmental stages (e.g., ~400 µm in diameter at the time of scleral cartilage emergence). Moreover, the tilt of the scleral cartilage ring in teleosts may be related to heterogeneity in the expression profiles of the POM subpopulation upon their establishment around the optic cup (Section 3.2.4 which discusses the heterogeneity of POM gene expression).

4.3 TGF-ß and FGF Signaling Inhibition in the Periocular Mesenchyme.

TGF-ß and FGF signaling pathways have been indicated in skeletogenic epithelial-mesenchymal interactions involving the cranial neural crest of chicken, mice, and zebrafish (introduced in Section 3.1) (Hall, 1992; Chai et al., 1994; Rice et al., 2003; Walshe & Mason, 2003; Lai & Mitchell, 2005). As shown in Chapter 3, intravitreal injection of inhibitors for both TGF-ß and FGF signaling produced differential effects on derivatives of the POM, namely the scleral cartilage and epiphyseal bar (discussed in Section 3.4.3). In this section, I will further discuss why the scleral cartilage was unaffected, with respect to neural crest cell migration.

As previously introduced and discussed in Chapter 3, the POM is populated by cranial neural crest cells from the diencephalon and anterior mesencephalon (Williams & Bohnsack, 2020). Neural crest cells of the future POM delaminate and go on to migrate from the neural tube at approximately 14-hpf to 16-hpf in zebrafish (Klymkowsky et al., 2010). Later, by 23-hpf to 24-hpf, the neural crest cells reach the lateral surface of the optic cup (adjacent to the developing

RPE) and become established as the POM (Williams & Bohnsack, 2020). While it is possible that reciprocal signaling between the POM and RPE results in scleral cartilage induction as discussed above (Section 4.2), it is also possible that induction is due to signals received by the neural crest cells during their migration. Similar processes have previously been implicated in the development of many skeletal structures (e.g. the cartilages of the viscerocranium in zebrafish and chicken: Hall, 1986; Walshe & Mason, 2003). Migration of neural crest cells to the periocular region takes place along two routes: dorsal to the optic stalk, or ventral to the optic stalk (Langenberg et al., 2008; Williams & Bohnsack, 2020). During this migratory period signaling may be received from other tissues, such as the developing brain, optic stalk, or head endoderm, similar to the signaling received by migrating cranial neural crest from the surface ectoderm in the formation of the chicken mandible (Hall, 1986). The inhibition experiments performed in this study (Chapter 3) were conducted at 23-hpf and 26-hpf via intravitreal injection. At these timepoints, the POM becomes established around the optic cup, and therefore, inhibition of FGFRs and TGF-ß IR would have prevented mesenchymal reception of these signals if secreted from the RPE. Thus, I hypothesize that signaling from an alternative source (such as the neural tissues of the developing central nervous system, or the anterior-most endoderm) is likely responsible for induction of the scleral cartilage in zebrafish.

In order to further our understanding of this process, a spatiotemporal analysis of the expression of factors downstream in the TGF-ß and FGF signaling pathways (such as transcripts for *MSX1*, which is typically upregulated via FGF signaling, and *NCAM1, N-Cadherin* which are both upregulated via TGF-ß signaling during the development of chondrogenic condensations) could be performed via *in situ* hybridization. By performing such an experiment with control and

inhibitor injected-zebrafish at timepoints surrounding and shortly after inhibitor injection, a better understanding of where and when signaling is inhibited would be obtained.

4.4 Final Conclusions

Teleost scleral cartilage is an under studied skeletal element with fascinating developmental and morphological characteristics. Previous studies have examined the teleost ocular skeleton in regard to the scleral ossicles with relatively little attention paid to the scleral cartilage, save for a brief mention (Franz-Odendaal, 2008a; Franz-Odendaal et al., 2007; O'Quin et al., 2015). This thesis aimed to characterize the scleral cartilage in terms of both its morphological variation across teleost fish (discussed in Section 2.4), and in the mechanisms that result in its development. Overall, characterization of the scleral cartilage across zebrafish, the surface tetra, and cave tetra revealed differences in the time course of scleral cartilage development and growth between the fish. However, striking similarities were found in differential positioning of the scleral cartilage ring around the eye's circumference. Additionally, similar tendencies were observed in the differential growth rate of scleral cartilage in different regions of the eye. While some differences exist, these similarities indicate a high degree of conservation in the mechanisms that regulate scleral cartilage development amongst teleosts.

Moreover, inhibition of the TGF-ß and FGF signaling pathways upon the establishment of the POM was found to be ineffective in disrupting the scleral cartilage ring. Yet, they did disrupt other cartilage elements of the head that emerge at similar times (discussed in Section 3.4). In addition, previous studies demonstrated that global BMP inhibition was insufficient to disrupt scleral cartilage development or morphology (Zinck et al., 2021). Many studies have shown that these signaling pathways are indispensable for cartilage development, specifically in

the earliest stages of mesenchymal aggregation (Lough et al., 1996; Jung et al., 1999; Chai et al., 2003; Shimizu et al., 2007; Li & Dong, 2016). Thus, one can conclude that the teleost scleral cartilage is highly robust, considering its conserved morphology between fish and its tendency to resist perturbation.

Robust elements, such as this one, indicate a deep evolutionary history characterized by phenotypic stability in light of genetic and environmental variation (Félix & Wagner, 2008). The robustness of the scleral cartilage has been exemplified in the presence and morphology of the ring in across teleosts. However, the one factor varies is its depth. Based on the observed variation in scleral cartilage depth, with increased depth typically denoted by a benthic lifestyle (Franz-Odendaal & Hall, 2006; Franz-Odendaal et al., 2007) it stands to reason that variation in scleral cartilage depth is advantageous depending on the life-style or habitat, with many derived teleosts (such as the zebrafish and Mexican tetra) adopting the narrow phenotype, while many other derived teleosts adopt a deeper phenotype. It is possible that the increased mechanical strength provided by a deep cartilage is advantageous in deeper, benthic habitats, where water pressures are higher, while a lighter, narrowing ring, is advantageous in pelagic habitats where speed elicits ossification of the cartilage (Franz-Odendaal, 2018). However, benthic fish are known to generate increased intraocular pressure via fluid regulation in the choroid *rete* in order to withstand the ambient pressure of benthic environments (Herbert et al., 2004). Thus, the relationship between increased scleral cartilage depth in benthic environments may be multifaceted. As previously described, the scleral cartilage of terrestrial animals such as reptiles and avian forms a deep cup. Despite a lack of understanding regarding scleral cartilage development, it has been postulated that reptilian and teleost scleral cartilage share common ancestry (i.e., are evolutionarily homologous), due their consistent presence throughout

vertebrate phylogeny and highly similar placement within the sclera (Franz-Odendaal, 2018). The current study does not indicate the RPE as the inducer of scleral cartilage development despite the previous research described in the chicken. However, as discussed, the previous chicken RPE work may have been misinterpreted (Section 4.2). Therefore, it could be that the scleral cartilage of all vertebrates is induced by an alterative epithelial tissue (i.e., epithelia along the migratory pathway including the neural ectoderm or head endoderm), or perhaps, the neural crest cells of the presumptive POM are pre-determined to form cartilage prior to migration.

In conclusion, this thesis has provided an increased understanding of scleral cartilage morphology and development in teleosts and serves as a foundation for future research on the mechanisms regulating teleost scleral cartilage induction.

References

Abudayyeh, O. O., Gootenberg, J. S., Essletzbichler, P., Han, S., Joung, J., Belanto, J. J., Verdine, V., Cox, D. B. T., Kellner, M. J., Regev, A., Lander, E. S., Voytas, D. F., Ting, A. Y., & Zhang, F. (2017). RNA targeting with CRISPR-Cas13. *Nature*, *550*(7675), 280–284. https://doi.org/10.1038/nature24049

Alappat, S., Zhang, Z. Y., & Chen, Y. P. (2003). Msx homeobox gene family and craniofacial development. *Cell Research*, *13*(6), 429–442. https://doi.org/10.1038/sj.cr.7290185

Aranda, P. S., Lajoie, D. M., & Jorcyk, C. L. (2012). Bleach Gel: A Simple Agarose Gel for Analyzing RNA Quality. *Electrophoresis*, *33*(2), 366–369. https://doi.org/10.1002/elps.201100335

Atkins, J. B., & Franz-Odendaal, T. A. (2016). The sclerotic ring of squamates: an evo-devo-eco perspective. *Journal of Anatomy*, *229*(4), 503–513. https://doi.org/10.1111/joa.12498

Benjamin, M. (1990). *The cranial cartilages of teleosts and their classification*. 153–172.

Bi, W., Deng, J. M., Zhang, Z., Behringer, R. R., & de Crombrugghe, B. (1999). Sox9 is Required for Cartilage Formation. *Nature Genetics*, *22*(May), 85–89. https://doi.org/10.5771/9783845220314-31

Bird, N. C., & Mabee, P. M. (2003). Developmental Morphology of the Axial Skeleton of the Zebrafish, Danio rerio (Ostariophysi: Cyprinidae). *Developmental Dynamics*, *228*(3), 337–357. https://doi.org/10.1002/dvdy.10387

Blum, M., De Robertis, E. M., Wallingford, J. B., & Niehrs, C. (2015). Morpholinos: Antisense and Sensibility. *Developmental Cell*, *35*(2), 145–149. https://doi.org/10.1016/j.devcel.2015.09.017

Bok, D. (1993). The retinal pigment epithelium: A versatile partner in vision. *Journal of Cell Science*, *106*(SUPPL. 17), 189–195. https://doi.org/10.1242/jcs.1993.supplement_17.27

Bono, F., De Smet, F., Herbert, C., De Bock, K., Georgiadou, M., Fons, P., Tjwa, M., Alcouffe, C., Ny, A., Bianciotto, M., Jonckx, B., Murakami, M., Lanahan, A. A., Michielsen, C., Sibrac, D., Dol-Gleizes, F., Mazzone, M., Zacchigna, S., Herault, J. P., … Carmeliet, P. (2013). Inhibition of tumor angiogenesis and growth by a small-molecule multi-FGF receptor blocker with allosteric properties. *Cancer Cell*, *23*(4), 477–488. https://doi.org/10.1016/j.ccr.2013.02.019

Borowsky, R. (2008). Astyanax mexicanus, the blind Mexican cave fish: A model for studies in development and Morphology. *Cold Spring Harbor Protocols*, *3*(11). https://doi.org/10.1101/pdb.emo107

Brown, J. D., Dutta, S., Bharti, K., Bonner, R. F., Munson, P. J., Dawid, I. B., Akhtar, A. L., Onojafe, I. F., Alur, R. P., Gross, J. M., Hejtmancik, J. F., Jiao, X., Chan, W. Y., & Brooks, B. P. (2009). Expression profiling during ocular development identifies 2 NIz genes with a critical role in optic fissure closure. *Proceedings of the National Academy of Sciences of the United States of America*, *106*(5), 1462–1467. https://doi.org/10.1073/pnas.0812017106

Cavodeassi, F. (2018). Dynamic Tissue Rearrangements during Vertebrate Eye Morphogenesis: Insights from Fish Models. *Journal of Developmental Biology*, *6*(1), 4. https://doi.org/10.3390/jdb6010004

Cechmanek, P. B., & McFarlane, S. (2017). Retinal pigment epithelium expansion around the neural retina occurs in two separate phases with distinct mechanisms. *Developmental Dynamics*, *246*(8), 598–609. https://doi.org/10.1002/dvdy.24525

Chai, Y, Ito, Y., & Han, J. (2003). TGF-ß Signaling and its Functional Significance in Regulating the Fate of Cranial Neural Crest Cells. *Crit Rev Oral Biol Med*, *14*(2), 78–88.

Chai, Yang, Mah, A., Crohin, C., Groff, S., Bringas, P., Le, T., Santos, V., & Slavkin, H. (1994). Specific Transforming Growh Factor-ß Subtypes Regulate Embryonic Mouse Meckel's Cartilage and Tooth Development. *Developmental Biology*, *162*(1), 85–103.

Chauhan, B., Plageman, T., Lou, M., & Lang, R. (2015). Epithelial Morphogenesis: The Mouse Eye as a Model System. *Curr Top Dev Biol*, *111*(1), 375–399. https://doi.org/10.1016/bs.ctdb.2014.11.011.Epithelial

Cole, A. G. (2011). A review of diversity in the evolution and development of cartilage: the search for the origin of the chondrocyte. *European Cells & Materials*, *21*(May), 122–129. https://doi.org/10.22203/eCM.v021a10

Coulombre, A. J. (1961). Cytology of the Developing Eye. *International Review of Cytology*, *11*(C), 161–194. https://doi.org/10.1016/S0074-7696(08)62715-1

Couly, G. F., Coltey, P. M., & Le Douarin, N. M. (1993). The triple origin of skull in higher vertebrates: A study in quail-chick chimeras. *Development*, *117*(2), 409–429. https://doi.org/10.1242/dev.117.2.409

Cox, D. B. T., Gootenberg, J. S., Abudayyeh, O. O., Franklin, B., Kellner, M. J., Joung, J., & Zhang, F. (2017). RNA editing with CRISPR-Cas13. *Science*, *358*(6366), 1019–1027. https://doi.org/10.1126/science.aaq0180

Cubbage, C. C., & Mabee, P. M. (1996). Development of the cranium and paired fins in the zebrafish Danio rerio (Ostariophysi, Cyprinidae). *Journal of Morphology*, *229*(2), 121–160. https://doi.org/10.1002/(SICI)1097-4687(199608)229:2<121::AID-JMOR1>3.0.CO;2-4

Cunningham, C. M. P., Bellipanni, G., Habas, R., & Balciunas, D. (2020). Deletion of morpholino binding sites (DeMOBS) to assess specificity of morphant phenotypes. *Scientific Reports*, *10*(1), 1–7. https://doi.org/10.1038/s41598-020-71708-1

Dasgupta, K., Jeong, J., & Biology, C. (2019). Developmental Biology of the Meninges. *Genesis*, *57*(5), 1–26. https://doi.org/10.1002/dvg.23288.Developmental

De Smet, F., Tembuyser, B., Lenard, A., Claes, F., Zhang, J., Michielsen, C., Van Schepdael, A., Herbert, J. M., Bono, F., Affolter, M., Dewerchin, M., & Carmeliet, P. (2014). Fibroblast growth factor signaling affects vascular outgrowth and is required for the maintenance of blood vessel integrity. *Chemistry and Biology*, *21*(10), 1310–1317. https://doi.org/10.1016/j.chembiol.2014.07.018

Delatte, M., Von Den Hoff, J. W., Van Rheden, R. E. M., & Kuijpers-Jagtman, A. M. (2004). Primary and secondary cartilages of the neonatal rat: The femoral head and the mandibular condyle. *European Journal of Oral Sciences*, *112*(2), 156–162. https://doi.org/10.1111/j.0909-8836.2004.00108.x

DeLise, A. M., Fischer, L., & Tuan, R. S. (2000). Cellular interactions and signaling in cartilage development. *Osteoarthritis and Cartilage*, *8*(5), 309–334. https://doi.org/10.1053/joca.1999.0306

Dufton, M. (2013). *Early lens ablation causes dramatic long term effects on the bones of the craniofacial skeleton of the mexican tetra,*. *April*.

Dufton, M., Hall, B. K., & Franz-Odendaal, T. A. (2012). Early Lens Ablation Causes Dramatic Long-Term Effects on the Shape of Bones in the Craniofacial Skeleton of Astyanax mexicanus. *PLoS ONE*, *7*(11). https://doi.org/10.1371/journal.pone.0050308

Dutta, S., Sriskanda, S., Boobalan, E., Alur, R. P., Elkahloun, A., & Brooks, B. P. (2015). Nlz1 is required for cilia formation in zebrafish embryogenesis. *Developmental Biology*, *406*(2), 203–211. https://doi.org/10.1016/j.ydbio.2015.08.019

Eames, B. F., Sharpe, P. T., & Helms, J. A. (2004). Hierarchy revealed in the specification of three skeletal fates by Sox9 and Runx2. *Developmental Biology*, *274*(1), 188–200. https://doi.org/10.1016/j.ydbio.2004.07.006

Eisen, J. S., & Smith, J. C. (2008). Controlling morpholino experiments: Don't stop making antisense. *Development*, *135*(10), 1735–1743. https://doi.org/10.1242/dev.001115

Ekanayake, S., & Tuan, R. S. (1994). Chondrogenesis of neural crest cells: Effect of poly-l-lysine and bone extract. *Differentiation*, *58*(1), 19–27. https://doi.org/10.1046/j.1432-0436.1994.5810019.x

England, S. J., Blanchard, G. B., Mahadevan, L., & Adams, R. J. (2006). A dynamic fate map of the forebrain shows how vertebrate eyes form and explains two causes of cyclopia. *Development*, *133*(23), 4613–4617. https://doi.org/10.1242/dev.02678

Félix, M. A., & Wagner, A. (2008). Robustness and evolution: Concepts, insights and challenges from a developmental model system. *Heredity*, *100*(2), 132–140. https://doi.org/10.1038/sj.hdy.6800915

Franz-Odendaal, T. A. (2008a). Scleral ossicles of teleostei: Evolutionary and developmental trends. *Anatomical Record*, *291*(2), 161–168. https://doi.org/10.1002/ar.20639

Franz-Odendaal, T. A. (2008b). Toward understanding the development of scleral ossicles in the chicken, Gallus gallus. *Developmental Dynamics*, *237*(11), 3240–3251. https://doi.org/10.1002/dvdy.21754

Franz-Odendaal, T. A. (2011). The ocular skeleton through the eye of evo-devo. *Journal of Experimental Zoology Part B: Molecular and Developmental Evolution*, *316 B*(6), 393–401. https://doi.org/10.1002/jez.b.21415

Franz-Odendaal, T. A. (2018). Skeletons of the Eye: An Evolutionary and Developmental Perspective. *Anatomical Record*, *697*(October 2017), 1–10. https://doi.org/10.1002/ar.24043

Franz-Odendaal, T. A., & Hall, B. K. (2006). Skeletal Elements Within Teleost Eyes and a Discussion of Their Homology. *Journal of Morphology*, *267*, 1326–1337. https://doi.org/10.1002/jmor

Franz-Odendaal, T. A., Ryan, K., & Hall, B. K. (2007). Developmental and morphological variation in the teleost craniofacial skeleton reveals an unusual mode of ossification. *Journal of Experimental Zoology Part B: Molecular and Developmental Evolution*, *308*(6), 709–721. https://doi.org/10.1002/jez.b.21185

Franz-Odendaal, T. A., & Vickaryous, M. K. (2006). Skeletal elements in the vertebrate eye and adnexa: Morphological and developmental perspectives. *Developmental Dynamics*, *235*(5), 1244–1255. https://doi.org/10.1002/dvdy.20718

Fuhrmann, S. (2010). Eye morphogenesis and patterning of the optic vesicle. In *Current Topics in Developmental Biology* (Vol. 93, Issue C). Elsevier Inc. https://doi.org/10.1016/B978-0-12-385044-7.00003-5

Gage, P. J., Rhoades, W., Prucka, S. K., & Hjalt, T. (2005). Fate maps of neural crest and mesoderm in the mammalian eye. *Investigative Ophthalmology and Visual Science*, *46*(11), 4200–4208. https://doi.org/10.1167/iovs.05-0691

Gentili, C., & Cancedda, R. (2009). Cartilage and bone extracellular matrix. *Current Pharmaceutical Design*, *15*(12), 1334–1348. https://doi.org/10.2174/138161209787846739

Gentsch, G. E., Spruce, T., Monteiro, R. S., Owens, N. D. L., Martin, S. R., & Smith, J. C. (2018). Innate Immune Response and Off-Target Mis-splicing Are Common Morpholino-Induced Side Effects in Xenopus. *Developmental Cell*, *44*(5), 597-610.e10. https://doi.org/10.1016/j.devcel.2018.01.022

Gerety, S. S., & Wilkinson, D. G. (2011). Morpholino artifacts provide pitfalls and reveal a novel role for pro-apoptotic genes in hindbrain boundary development. *Developmental Biology*, *350*(2), 279–289. https://doi.org/10.1016/j.ydbio.2010.11.030

Gestri, G., Link, B. A., & Neuhauss, S. C. F. (2012). The visual system of zebrafish and its use to model human ocular Diseases. *Developmental Neurobiology*, *72*(3), 302–327. https://doi.org/10.1002/dneu.20919

Giffin, J. L., Gaitor, D., & Franz-Odendaal, T. A. (2019). The Forgotten Skeletogenic Condensations: A Comparison of Early Skeletal Development Amongst Vertebrates. *Journal of Developmental Biology*, *7*(1), 4. https://doi.org/10.3390/jdb7010004

Gonzalez-Fernandez, F., & Healy, J. I. (1990). Early expression of the gene of interphotoreceptor retinol-binding protein during photoreceptor differentiation suggests a critical role for the interphotoreceptor matrix and retinal development. *Journal of Cell Biology*, *111*(6 I), 2775–2784. https://doi.org/10.1083/jcb.111.6.2775

Hall, B K. (1986). The role of movement and tissue interactions in the development and growth of bone and secondary cartilage in the clavicle of the embryonic chick. *Journal of Embryology and Experimental Morphology*, *93*, 133–152. http://www.ncbi.nlm.nih.gov/pubmed/3734681

Hall, B K. (1992). Cell-cell interactions in craniofacial growth and development. *The Biological Mechanisms of Tooth Movement and Craniofacial Adaptation*, *January 1992*, 11–17.

Hall, B. K., & Miyake, T. (2000). All for one and one for all: Condensations and the initiation of skeletal development. *BioEssays*, *22*(2), 138–147. https://doi.org/10.1002/(SICI)1521-1878(200002)22:2<138::AID-BIES5>3.0.CO;2-4

Hall, B. K., & Tremaine, R. (1979). Ability of neural crest cells from the embryonic chick to differentiate into cartilage before their migration away from the neural tube. *The Anatomical Record*, *194*(3), 469–475. https://doi.org/10.1002/ar.1091940312

Hall, B. K. (1981). The induction of neural crest-derived cartilage and bone by embryonic epithelia: an analysis of the mode of action of an epithelial- mesenchymal interaction. *J. Embryol. Exp. Morph*, *6*(1975), 305–320.

Hall, B. K. (1986). The role of movement and tissue interactions in the development and growth of bone and secondary cartilage in the clavicle of the embryonic chick. *Journal of Embryology and Experimental Morphology*, *93*(May), 133–152. http://www.ncbi.nlm.nih.gov/pubmed/3734681

Hall, B. K. (2015). Bones and Cartilage. In *Bones and Cartilage* (pp. 515–527). https://doi.org/10.1016/B978-0-12-416678-3.00033-1

Herbert, C., Schieborr, U., Saxena, K., Juraszek, J., De Smet, F., Alcouffe, C., Bianciotto, M., Saladino, G., Sibrac, D., Kudlinzki, D., Sreeramulu, S., Brown, A., Rigon, P., Herault, J. P., Lassalle, G., Blundell, T. L., Rousseau, F., Gils, A., Schymkowitz, J., … Bono, F. (2013). Molecular mechanism of SSR128129E, an extracellularly acting, small-molecule, allosteric inhibitor of fgf receptor signaling. *Cancer Cell*, *23*(4), 489–501. https://doi.org/10.1016/j.ccr.2013.02.018

Herbert, N. A., Steffensen, J. F., & Jordan, A. D. (2004). The interrelated effects of body size and choroid rete development on the ocular O2 partial pressure of Atlantic (Gadus morhua) and Greenland cod (Gadus ogac). *Polar Biology*, *27*(12), 748–752. https://doi.org/10.1007/s00300-004-0657-6

Holderfield, M. T., & Hughes, C. C. W. (2008). Crosstalk between vascular endothelial growth factor, notch, and transforming growth factor-β in vascular morphogenesis. *Circulation Research*, *102*(6), 637–652. https://doi.org/10.1161/CIRCRESAHA.107.167171

Horakova, D., Cela, P., Krejci, P., Balek, L., Moravcova Balkova, S., Matalova, E., & Buchtova, M. (2014). Effect of FGFR inhibitors on chicken limb development. *Development Growth and Differentiation*, *56*(8), 555–572. https://doi.org/10.1111/dgd.12156

Isogai, S., Horiguchi, M., & Weinstein, B. M. (2001). The vascular anatomy of the developing zebrafish: An atlas of embryonic and early larval development. *Developmental Biology*, *230*(2), 278–301. https://doi.org/10.1006/dbio.2000.9995

Iwata, H., & Ukai, Y. (2002). SHAPE: a computer program package for quantitative evaluation of biological shapes based on elliptic Fourier descriptors. *The Journal of Heredity*, *93*(5), 384–385. https://doi.org/10.1093/jhered/93.5.384

Jeffery, W. R. (2001). Cavefish as a model system in evolutionary developmental biology. *Developmental Biology*, *231*(1), 1–12. https://doi.org/10.1006/dbio.2000.0121

Jeffery, W. R., Strickler, A. G., & Yamamoto, Y. (2003). To see or not to see: Evolution of eye degeneration in Mexican blind cavefish. *Integrative and Comparative Biology*, *43*(4), 531–541. https://doi.org/10.1093/icb/43.4.531

Jeradi, S., & Hammerschmidt, M. (2016). Retinoic acid-induced premature osteoblast-to-preosteocyte transitioning has multiple effects on calvarial development. *Development (Cambridge)*, *143*(7), 1205–1216. https://doi.org/10.1242/dev.129189

Jiang, X., Iseki, S., Maxson, R. E., Sucov, H. M., & Morriss-Kay, G. M. (2002). Tissue origins and interactions in the mammalian skull vault. *Developmental Biology*, *241*(1), 106–116. https://doi.org/10.1006/dbio.2001.0487

Johnston, M. C., Noden, D. M., Hazelton, R. D., Coulombre, J. L., & Coulombre, A. J. (1979). Origins of avian ocular and periocular tissues. *Experimental Eye Research*, *29*(1), 27–43. https://doi.org/10.1016/0014-4835(79)90164-7

Jung, H. S., Oropeza, V., & Thesleff, I. (1999). Shh, Bmp-2, Bmp-4 and Fgf-8 are associated with initiation and patterning of mouse tongue papillae. *Mechanisms of Development*, *81*(1–2), 179–182. https://doi.org/10.1016/S0925-4773(98)00234-2

Kague, E., Gallagher, M., Burke, S., Parsons, M., Franz-Odendaal, T. A., & Fisher, S. (2012). Skeletogenic Fate of Zebrafish Cranial and Trunk Neural Crest. *PLoS ONE*, *7*(11), 1–13. https://doi.org/10.1371/journal.pone.0047394

Kaufman, R., Weiss, O., Sebbagh, M., Ravid, R., Gibbs-Bar, L., Yaniv, K., & Inbal, A. (2015). Development and origins of Zebrafish ocular vasculature. *BMC Developmental Biology*, *15*(1), 1–9. https://doi.org/10.1186/s12861-015-0066-9

Kimmel, C. B., Miller, C. T., Kruze, G., Ullmann, B., Bremiller, R. A., Larison, K. D., & Snyder, H. C. (1998). The shaping of pharyngeal cartilages during early development of the zebrafish. *Developmental Biology*, *203*(2), 245–263. https://doi.org/10.1006/dbio.1998.9016

Kindl, G. H., & O'Quin, K. E. (2019). On Intraspecific and Interspecific Variation in Teleost Scleral Ossification. *Anatomical Record*, *302*(7), 1238–1249. https://doi.org/10.1002/ar.24080

Klymkowsky, M. W., Rossi, C. C., & Artinger, K. B. (2010). Mechanisms driving neural crest induction and migration in the zebrafish and Xenopus laevis. *Cell Adhesion and Migration*, *4*(4), 595–608. https://doi.org/10.4161/cam.4.4.12962

Kondrychyn, I., Teh, C., Sin, M., & Korzh, V. (2013). Stretching Morphogenesis of the Roof Plate and Formation of the Central Canal. *PLoS ONE*, *8*(2), 1–12. https://doi.org/10.1371/journal.pone.0056219

Konermann, S., Lotfy, P., Brideau, N. J., Oki, J., Shokhirev, M. N., & Hsu, P. D. (2018). Transcriptome Engineering with RNA-Targeting Type VI-D CRISPR Effectors. *Cell*, *173*(3), 665-676.e14. https://doi.org/10.1016/j.cell.2018.02.033

Kotini, M. P., Bachmann, F., Spickermann, J., McSheehy, P. M., & Affolter, M. (2021). Probing the effects of the FGFR-inhibitor derazantinib on vascular development in Zebrafish embryos. *Pharmaceuticals*, *14*(1), 1–13. https://doi.org/10.3390/ph14010025

Kushawah, G., Abugattas-Nuñez del Prado, J., Martinez-Morales, J. R., DeVore, M., Guelfo, J. R., Brannan, E. O., Wang, W., Corbin, T. J., Moran, A. M., Alvarado, A. S., Málaga-Trillo, E., Takacs, C. M., Bazzini, A. A., & Moreno-Mateos, M. A. (2020). CRISPR-Cas13d induces efficient mRNA knock-down in animal embryos. *BioRxiv*, 1–7. https://doi.org/10.1101/2020.01.13.904763

Kwan, K. M., Otsuna, H., Kidokoro, H., Carney, K. R., Saijoh, Y., & Chien, C.-B. (2012). A Complex Choreography of Cell Movements Shapes the Vertebrate Eye. *Development*, *139*(2), 359–372. https://doi.org/10.1242/dev.071407

Lai, L. P., & Mitchell, J. (2005). Indian hedgehog: Its roles and regulation in endochondral bone development. *Journal of Cellular Biochemistry*, *96*(6), 1163–1173. https://doi.org/10.1002/jcb.20635

Langenberg, T., Kahana, A., Wszalek, J. A., & Halloran, M. C. (2008). *The Eye Organizes Neural Crest Cell Migration*. *237*(6), 1645–1652. https://doi.org/10.1002/dvdy.21577.The

Le Douarin, N. M., Creuzet, S., Couly, G., & Dupin, E. (2004). Neural crest cell plasticity and its limits. *Development*, *131*(19), 4637–4650. https://doi.org/10.1242/dev.01350

Leerberg, D. M., Hopton, R. E., & Draper, B. W. (2019). Fibroblast growth factor receptors function redundantly during zebrafish embryonic development. *Genetics*, *212*(4), 1301–1319. https://doi.org/10.1534/genetics.119.302345

Lefebvre, V, Huang, W., Harley, V. R., Goodfellow, P. N., & de Crombrugghe, B. (1997). SOX9 is a potent activator of the chondrocyte-specific enhancer of the pro alpha1(II) collagen gene. *Molecular and Cellular Biology*, *17*(4), 2336–2346. https://doi.org/10.1128/mcb.17.4.2336

Lefebvre, Véronique, & Dvir-Ginzberg, M. (2017). SOX9 and the many facets of its regulation in the chondrocyte lineage. *Connective Tissue Research*, *58*(1), 2–14. https://doi.org/10.1080/03008207.2016.1183667

Li, J., & Dong, S. (2016). The signaling pathways involved in chondrocyte differentiation and hypertrophic differentiation. *Stem Cells International*, *2016*, 1–13. https://doi.org/10.1155/2016/2470351

Li, Z., Joseph, N. M., & Easter, S. S. (2000). The morphogenesis of the zebrafish eye, including a fate map of the optic vesicle. *Developmental Dynamics*, *218*(1), 175–188. https://doi.org/10.1002/(SICI)1097-0177(200005)218:1<175::AID-DVDY15>3.0.CO;2-K

Lim, J., Tu, X., Choi, K., Akiyama, H., Mishina, Y., & Long, F. (2015). BMP-Smad4 signaling is required for precartilaginous mesenchymal condensation independent of Sox9 in the mouse. *Developmental Biology*, *400*(1), 132–138. https://doi.org/10.1016/j.ydbio.2015.01.022

Lingam, G., Sen, A. C., Lingam, V., Bhende, M., Padhi, T. R., & Xinyi, S. (2021). Ocular coloboma—a comprehensive review for the clinician. *Eye (Basingstoke)*. https://doi.org/10.1038/s41433-021-01501-5

Lister, J. A. (2002). Development of pigment cells in the zebrafish embryo. *Microscopy Research and Technique*, *58*(6), 435–441. https://doi.org/10.1002/jemt.10161

Lister, J. A., Cooper, C., Nguyen, K., Modrell, M., Grant, K., & Raible, D. W. (2006). Zebrafish Foxd3 is required for development of a subset of neural crest derivatives. *Developmental Biology*, *290*(1), 92–104. https://doi.org/10.1016/j.ydbio.2005.11.014

Lough, J., Barron, M., Brogley, M., Sugi, Y., Bolender, D. L., & Zhu, X. (1996). Combined BMP-2 and FGF-4, but neither factor alone, induces cardiogenesis in non-precardiac embryonic mesoderm. *Developmental Biology*, *178*(1), 198–202. https://doi.org/10.1006/dbio.1996.0211

Maes, J., Verlooy, L., Buenafe, O. E., de Witte, P. A. M., Esguerra, C. V., & Crawford, A. D. (2012). Evaluation of 14 Organic Solvents and Carriers for Screening Applications in Zebrafish Embryos and Larvae. *PLoS ONE*, *7*(10), 1–9. https://doi.org/10.1371/journal.pone.0043850

Martínez-Morales, J. R., Dolez, V., Rodrigo, I., Zaccarini, R., Leconte, L., Bovolenta, P., & Saule, S. (2003). OTX2 activates the molecular network underlying retina pigment epithelium differentiation. *Journal of Biological Chemistry*, *278*(24), 21721–21731. https://doi.org/10.1074/jbc.M301708200

Massagué, J. (1992). Receptors for the TGF-β family. *Cell*, *69*(7), 1067–1070. https://doi.org/10.1016/0092-8674(92)90627-O

McGaugh, S. E., Gross, J. B., Aken, B., Blin, M., Borowsky, R., Chalopin, D., Hinaux, H., Jeffery, W. R., Keene, A., Ma, L., Minx, P., Murphy, D., O'Quin, K. E., Rétaux, S., Rohner, N., Searle, S. M. J., Stahl, B. A., Tabin, C., Volff, J. N., … Warren, W. C. (2014). The cavefish genome reveals candidate genes for eye loss. *Nature Communications*, *5*. https://doi.org/10.1038/ncomms6307

Meulen, K. L. Van Der. (2021). *PERIOCULAR MESENCHYME HETEROGENEITY DURING MORPHOGENESIS OF THE VERTEBRATE OCULAR ANTERIOR SEGMENT*.

Mongera, A., Singh, A. P., Levesque, M. P., Chen, Y. Y., Konstantinidis, P., & Nüsslein-Volhard, C. (2013). Genetic lineage labeling in zebrafish uncovers novel neural crest contributions to the head, including gill pillar cells. *Development (Cambridge)*, *140*(4), 916–925. https://doi.org/10.1242/dev.091066

Muller, F., Rohrer, H., & Vogel-Hopker, A. (2007). Bone morphogenetic proteins specify the retinal pigment epithelium in the chick embryo. *Development*, *134*(19), 3483–3493. https://doi.org/10.1242/dev.02884

Murtaugh, L. C., Chyung, J. H., & Lassar, A. B. (1999). Sonic hedgehog promotes somitic chondrogenesis by altering the cellular response to BMP signaling. *Genes and Development*, *13*(2), 225–237. https://doi.org/10.1101/gad.13.2.225

Nassar, K., Grisanti, S., Tura, A., Lüke, J., Lüke, M., Soliman, M., & Grisanti, S. (2014). A TGF-β receptor 1 inhibitor for prevention of proliferative vitreoretinopathy. *Experimental Eye Research*, *123*, 72–86. https://doi.org/10.1016/j.exer.2014.04.006

Newsome, D. A. (1972). Cartilage induction by retinal pigmented epithelium of chick embryo. *Developmental Biology*, *27*(4), 575–579. https://doi.org/10.1016/0012-1606(72)90194-7

Nicoli, S., De Sena, G., & Presta, M. (2009). Fibroblast growth factor 2-induced angiogenesis in zebrafish: The zebrafish yolk membrane (ZFYM) angiogenesis assay. *Journal of Cellular and Molecular Medicine*, *13*(8 B), 2061–2068. https://doi.org/10.1111/j.1582-4934.2008.00432.x

O'Quin, K. E., Doshi, P., Lyon, A., Hoenemeyer, E., Yoshizawa, M., & Jeffery, W. R. (2015). Complex Evolutionary and Genetic Patterns Characterize the Loss of Scleral Ossification in the Blind Cavefish Astyanax mexicanus. *PLoS ONE*, *10*(12), 1–19. https://doi.org/10.1371/journal.pone.0142208

Parichy, D. M., Elizondo, M. R., Mills, M. G., Gordon, T. N., & Engeszer, E. (2011). Normal Table of Post-Embryonic Zebrafish Development: Staging by Externally Visible Anatomy of the Living Fish. *Devolopmental Dynamics*, *238*(12), 2975–3015. https://doi.org/10.1002/dvdy.22113.Normal

Park, C. Y., Marando, C. M., Liao, J. A., Lee, J. K., Kwon, J., & Chuck, R. S. (2016). Details of the collagen and elastin architecture in the human limbal conjunctiva, tenon's capsule and sclera revealed by two-photon excited fluorescence microscopy. *Investigative Ophthalmology and Visual Science*, *57*(13), 5602–5610. https://doi.org/10.1167/iovs.16-19706

Peters, H., Neubüser, A., Kratochwil, K., & Balling, R. (1998). Pax9-deficient mice lack pharyngeal pouch derivatives and teeth and exhibit craniofacial and limb abnormalities. *Genes and Development*, *12*(17), 2735–2747. https://doi.org/10.1101/gad.12.17.2735

Protas, M., Conrad, M., Gross, J. B., Tabin, C., & Borowsky, R. (2007). Regressive Evolution in the Mexican Cave Tetra, Astyanax mexicanus. *Current Biology*, *17*(5), 452–454. https://doi.org/10.1016/j.cub.2007.01.051

Rajaram, S., Patel, S., Uggini, G. K., Desai, I., & Balakrishnan, S. (2017). BMP signaling regulates the skeletal and connective tissue differentiation during caudal fin regeneration in sailfin molly (Poecilia latipinna). *Development Growth and Differentiation*, *59*(8), 629–638. https://doi.org/10.1111/dgd.12392

Retting, K. N., Song, B., Yoon, B. S., & Lyons, K. M. (2009). BMP canonical Smad signaling through Smad1 and Smad5 is required for endochondral bone formation. *Development*, *136*(7), 1093–1104. https://doi.org/10.1242/dev.029926

Rice, D. P. C., Rice, R., & Thesleff, I. (2003). Molecular mechanisms in calvarial bone and suture development, and their relation to craniosynostosis. *European Journal of Orthodontics*, *25*(2), 139–148. https://doi.org/10.1093/ejo/25.2.139

Rocha, M., Singh, N., Ahsan, K., Beiriger, A., & Prince, V. E. (2020). Neural crest development: insights from the zebrafish. *Developmental Dynamics*, *249*(1), 88–111. https://doi.org/10.1002/dvdy.122

Sanvitale, C. E., Kerr, G., Chaikuad, A., Ramel, M. C., Mohedas, A. H., Reichert, S., Wang, Y., Triffitt, J. T., Cuny, G. D., Yu, P. B., Hill, C. S., & Bullock, A. N. (2013). A New Class of Small Molecule Inhibitor of BMP Signaling. *PLoS ONE*, *8*(4). https://doi.org/10.1371/journal.pone.0062721

Schubert, S., Keddig, N., Hanel, R., & Kammann, U. (2014). Microinjection into zebrafish embryos (Danio rerio) - a useful tool in aquatic toxicity testing? *Environmental Sciences Europe*, *26*(1). https://doi.org/10.1186/s12302-014-0032-3

Sekiya, I., Tsuji, K., Koopman, P., Watanabe, H., Yamada, Y., Shinomiya, K., Nifuji, A., & Noda, M. (2000). SOX9 enhances aggrecan gene promoter/enhancer activity and is up-regulated by retinoic acid in a cartilage-derived cell line, TC6. *Journal of Biological Chemistry*, *275*(15), 10738–10744. https://doi.org/10.1074/jbc.275.15.10738

Shimizu, H., Yokoyama, S., & Asahara, H. (2007). Growth and differentiation of the developing limb bud from the perspective of chondrogenesis. *Development Growth and Differentiation*, *49*(6), 449–454. https://doi.org/10.1111/j.1440-169X.2007.00945.x

Southern, E. M. (2002). Denaturing Gel Electrophoresis of DNA in Alkaline Agarose Gels. *Encyclopedia of Life Sciences*, 1–4. https://doi.org/10.1038/npg.els.0003758

Stead, A. H., & Moffat, A. C. (1983). Quantification of the interaction between barbiturates and alcohol and interpretation of fatal blood concentrations. *Human Toxicology*, *2*(1), 5–14. https://doi.org/10.1177/096032718300200101

Stewart, P. A., & McCallion, D. J. (1975). Establishment of the scleral cartilage in the chick. *Developmental Biology*, *46*(2), 383–389. https://doi.org/10.1016/0012-1606(75)90114-1

Strauss, O. (2005). The Retinal Pigment Epithelium in Visual Function. *Physiological Reviews*, *85*(3), 845–881. https://doi.org/10.1152/physrev.00021.2004.

Stroeva, O. G., & Mitashov, V. I. (1983). Retinal Pigment Epithelium: Proliferation and Differentiation during Development and Regeneration. In *International Review of Cytology* (Vol. 83, Issue C). https://doi.org/10.1016/S0074-7696(08)61689-7

Take-uchi, M., Clarke, J. D. W., & Wilson, S. W. (2003). Hedgehog signalling maintains the optic stalk-retinal interface through the regulation of Vax gene activity. *Development*, *130*(5), 955–968. https://doi.org/10.1242/dev.00305

Thompson, H., Griffiths, J. S., Jeffery, G., & McGonnell, I. M. (2010). The retinal pigment epithelium of the eye regulates the development of scleral cartilage. *Developmental Biology*, *347*(1), 40–52. https://doi.org/10.1016/j.ydbio.2010.08.006

Topczewska, J. M., Shoela, R. A., Tomaszewski, J. P., Mirmira, R. B., & Gosain, A. K. (2016). The Morphogenesis of Cranial Sutures in Zebrafish. *PLoS ONE*, 1–23. https://doi.org/10.1371/journal.pone.0165775

Torres-Paz, J., Hyacinthe, C., Pierre, C., & Rétaux, S. (2018). Towards an integrated approach to understand Mexican cavefish evolution. *Biology Letters*, *14*(8). https://doi.org/10.1098/rsbl.2018.0101

Tsonis, P. A., Rio-Tsonis, K. D., Millan, J. L., & Wheelock, M. J. (1994). Expression of N-Cadherin and Alkaline Phosphatase in Chick Limb Bud Mesenchymal Cells: Regulation by 1,25-Dihydroxyvitamin D3 or TGF-ß1. *Experimental Cell Research*, *213*, 433–437.

Tubbs, R. S., Bosmia, A. N., & Cohen-Gadol, A. A. (2012). The human calvaria: A review of embryology, anatomy, pathology, and molecular development. *Child's Nervous System*, *28*(1), 23–31. https://doi.org/10.1007/s00381-011-1637-0

Van Der Meulen, K. L., Vöcking, O., Weaver, M. L., Meshram, N. N., & Famulski, J. K. (2020). Spatiotemporal Characterization of Anterior Segment Mesenchyme Heterogeneity During Zebrafish Ocular Anterior Segment Development. *Frontiers in Cell and Developmental Biology*, *8*(May), 1–16. https://doi.org/10.3389/fcell.2020.00379

Veldman, M. B., & Lin, S. (2008). Zebrafish as a Developmental Model Organism for. *Pediatric Research*, *64*(5), 470–476.

Vivatbutsiri, P., Ichinose, S., Hytönen, M., Sainio, K., Eto, K., & Iseki, S. (2008). Impaired meningeal development in association with apical expansion of calvarial bone osteogenesis in the Foxc1 mutant. *Journal of Anatomy*, *212*(5), 603–611. https://doi.org/10.1111/j.1469-7580.2008.00893.x

Walker, M. B., & Kimmel, C. B. (2007). A two-color acid-free cartilage and bone stain for zebrafish larvae. *Biotechnic and Histochemistry*, *82*(1), 23–28. https://doi.org/10.1080/10520290701333558

Walshe, J., & Mason, I. (2003). Fgf signalling is required for formation of cartilage in the head. *Developmental Biology*, *264*(2), 522–536. https://doi.org/10.1016/j.ydbio.2003.08.010

Wedlock, D. E., & McCallion, D. J. (1969). Induction of scleral cartilage in the chorioallantois of the chick embryo. *Canadian Journal of Zoology*, *47*(1), 142–143. https://doi.org/10.1139/z69-026

Williams, A. L., & Bohnsack, B. L. (2020). The Ocular Neural Crest: Specification, Migration, and Then What? *Frontiers in Cell and Developmental Biology*, *8*(December). https://doi.org/10.3389/fcell.2020.595896

Wu, X., Shi, W., & Cao, X. (2007). Multiplicity of BMP signaling in skeletal development. *Annals of the New York Academy of Sciences*, *1116*(205), 29–49. https://doi.org/10.1196/annals.1402.053

Xie, J., Farage, E., Sugimoto, M., & Anand-Apte, B. (2010). A novel transgenic zebrafish model for blood-brain and blood-retinal barrier development. *BMC Developmental Biology*, *10*. https://doi.org/10.1186/1471-213X-10-76

Xu, P., Yu, H. V., Tseng, K. C., Flath, M., Fabian, P., Segil, N., & Crump, J. G. (2021). Foxc1 establishes 1 enhancer accessibility for craniofacial cartilage differentiation. *ELife*, *10*, 1–50. https://doi.org/10.7554/eLife.63595

Yamamoto, Y., & Jeffery, W. R. (2002). Probing teleost eye development by lens transplantation. *Methods*, *28*(4), 420–426. https://doi.org/10.1016/S1046-2023(02)00261-X

Yan, Y.-L. (2005). A pair of Sox: distinct and overlapping functions of zebrafish sox9 co-orthologs in craniofacial and pectoral fin development. *Development*, *132*(5), 1069–1083. https://doi.org/10.1242/dev.01674

Yan, Y. L., Miller, C. T., Nissen, R. M., Singer, A., Liu, D., Kirn, A., Draper, B., Willoughby, J., Morcos, P. A., Amsterdam, A., Chung, B. C., Westerfield, M., Haffter, P., Hopkins, N., Kimmel, C., & Postlethwait, J. H. (2002). A zebrafish sox9 gene required for cartilage morphogenesis. *Development*, *129*(21), 5065–5079. http://www.ncbi.nlm.nih.gov/pubmed/12397114%5Cnhttp://dev.biologists.org/content/129/21/5065.full.pdf

Yang, J., Kitami, M., Pan, H., Nakamura, M. T., Zhang, H., Liu, F., Zhu, L., Komatsu, Y., & Mishina, Y. (2021). Augmented BMP signaling commits cranial neural crest cells to a chondrogenic fate by suppressing autophagic β-catenin degradation. *Science Signaling*, *14*(665), 1–19. https://doi.org/10.1126/SCISIGNAL.AAZ9368

Yelick, P. C., & Schilling, T. F. (2002). *Molecular Dissection of Craniofacial Development Using Zebrafish*. *13*(4), 308–322.

Yi SE, Daluiski A, Pederson R, Rosen V, L. K. (2000). The type I BMP receptor BMPRIB is required for chondrogenesis in the mouse limb. *Development*, *127*, 621–630. https://doi.org/10.1002/jbmr.2385

Yin, A., Korzh, S., Winata, C. L., Korzh, V., & Gong, Z. (2011). Wnt signaling is required for early development of zebrafish swimbladder. *PLoS ONE*, *6*(3). https://doi.org/10.1371/journal.pone.0018431

Zinck, N. W., Jeradi, S., & Franz-Odendaal, T. A. (2021). Elucidating the early signaling cues involved in zebrafish chondrogenesis and cartilage morphology. *Journal of Experimental Zoology Part B: Molecular and Developmental Evolution*, *336*(1), 18–31. https://doi.org/10.1002/jez.b.23012

Appendix A:

Progress Towards Investigating the Role of the Retinal Pigment Epithelium via Induced Ocular Coloboma.

A.1. Brief Synopsis:

During my research, I explored the possibility of using CRISPR-Cas13 to generate a knockout zebrafish with disrupted RPE in order to explore whether these knockout fish would have disrupted scleral cartilage. As indicated in Section 1.5 (Objectives and Hypotheses), one of my objectives was to investigate the involvement of the RPE in scleral cartilage induction and morphogenesis. I hypothesized that scleral cartilage morphology will be altered in CRISPR-zebrafish with disrupted RPE development. Thus, if the knockout fish displayed a scleral cartilage phenotype, this would provide evidence that the RPE may be an important inducing epithelium for cartilage induction in the zebrafish eye. This objective was ultimately aborted for a variety of reasons (discussed below) as well as due to time constraints imposed by the global COVID-19 pandemic of 2020-2021.

A.2 Rationale:

Research in the chicken, *Gallus gallus*, has suggested that the retinal pigmented epithelium (RPE) may play a role in scleral cartilage induction (Newsome, 1972; Thompson et al., 2010). However, no evidence currently exists to support this hypothesis in the zebrafish.

Ocular coloboma is a malformation of the ventral eye in which the embryonic optic fissure fails to close, leaving a gap in the optic cup derived tissues on the eye (Lingam et al., 2021). In zebrafish, a transient disruption of *VAX1* signaling via morpholino knockdown is sufficient to led to incomplete closure of the optic fissure as denoted by a permanent ventral gap

in the optic cup tissues (specifically in the RPE and NR), at 30 and 60 hpf (Take-uchi et al., 2003). Prevention of optic fissure closure may be useful in elucidating the role of the RPE in scleral cartilage induction. Therefore, in order to investigate the RPE's potential role in the induction of the zebrafish scleral cartilage, a knock-down induced ocular coloboma model was generated to cause the incomplete fusion of the RPE in the ventral eye.

A.3 Approach:

Recently, Kushawah et al., (2020) adapted the CRISPR/Cas13d gene knockdown method for use in embryonic zebrafish. Cas13d knockdown, similar to the commonly used Cas9 knockout, utilizes a Cas protein paired with a guide RNA (gRNA) designed to target a specific nucleotide sequence for cleavage. However in contrast to Cas9, CRISPR/Cas13d acts via mRNA cleaves, leading to subsequent degradation (Abudayyeh et al., 2017; Kushawah et al., 2020). Further, it has been demonstrated that CRISPR-Cas13 method produces a more specific effect than other mRNA-targeting knockdown methods in mammalian cell culture (e.g. RNAi, morpholino) (Abudayyeh et al., 2017; Cox et al., 2017; Konermann et al., 2018). While the CRISPR-Cad13 system has only recently been adopted for use in zebrafish, it shows promise as a cost effective and precise alternative to morpholino mediated knockdown.

Objective and hypothesis: To investigate the involvement of the RPE in scleral cartilage induction and morphogenesis, the CRISPR-Cas13d knockdown method was used to induce ocular coloboma in zebrafish embryos. I hypothesized that knockdown of *Vax1* signaling via CRISPR-Cas13 would lead to ocular coloboma in zebrafish, and that incomplete fusion on the ventral optic cup will lead to morphological disruption of the adjacent scleral cartilage.

A.4 Methods

A.4.1 Generation of Cas13d mRNA Template

In order to generate Cas13d mRNA for injection, the pET-28b-RfxCas13d-His plasmid previously synthesized by Kushawah et al., (2020) was procured (Addgene 141322). The pET-28b-RfxCas13d-His plasmid was housed in DH5α competent cells. In order to isolate DH5α *E. coli* containing pET-28b-RfxCas13d-His, cells were streaked on kanamycin+ 1% agarose plates and incubated overnight at 37°C. Following incubation, cells from a single isolated colony were used to inoculate 100 mL of liquid LB broth. The inoculated broth was incubated overnight, at which point noticeable proliferation of pET-28b-RfxCas13d-His DH5α cells had occurred. For a detailed protocol, see Appendix C.1.

In order to isolate the pET-28b-RfxCas13d-His plasmid, the overnight culture broth was divided into 2 mL aliquots for miniprep. For the full miniprep protocol, see Appendix X.2. Purified plasmid was reconstituted in TE buffer and stored at -20°C following miniprep. The identity of the plasmid was verified via restriction enzyme digest and subsequent agarose gel electrophoresis. Specifically, the pET-28b-RfxCas13d-His plasmid was digested with BGLII and NotI enzymes, to produce two predicted plasmid fragments of approximately 3000 and 5000 base pairs (Appendix E for full protocol). Gel imaging and analysis were conducted using a Gel-Doc and ImageLab software (Bio-Rad), and plasmid fragment length was determined via comparison to Promega 1 kb Step Ladder (Promega G6941). Plasmid sequencing was conducted by the Sanger Sequencing Institute at the Sick Kids Hospital (Toronto, Ontario) using primers for the T7 promotor and T7 terminal regions.

A.4.2 Guide RNA Design and Template Synthesis

In order to produce guide RNA oligos (gRNA) suitable for CRISPR/Cas13d knockdown of *Vax1,* gRNA templates were designed as previously described (Kushawah et al., 2020). The *vax1-201* transcript secondary structure was analyzed *in silico* using RNAfold Software (http://rna.tbi.univie.ac.at//cgibin/RNAWebSuite/RNAfold.cgi). Two protospacers of 22 nucleotides with low base-pairing probability from minimum free energy predictions (and thus highly accessible) were chosen as targets within the *vax1-201* transcript. DNA templates were created via fill-in PCR, using a universal Cas13d primer (RfxCas13d_universal, Table x), and a primer designed specifically for *vax1-201* degradation (*Vax1-201*_288-310, Table x). The universal Cas13d primer contained a T7 promotor for downstream transcription (Table A.1, italics), while the two specific primers contained the 22 nucleotide protospacers determined via secondary structure analysis (Table A.1, italics). The primers were designed to anneal at a direct repeat for RfxCas13d gRNAs (Table A.1, non-italics), at which extension would occur.

Table A.1. *Primer sequences for gRNA template synthesis. Bold text indicates T7 promotor and 22 base pair protospacer in RfxCas13d_universal and vax1-201_288-310 primer, respectively. Non-bold text indicates annealing (direct repeat) region (Kushawah et al., 2020).*

Primer	Sequence (5' – 3')
RfxCas13d_universal	**TAATACGACTCACTATA**GGAACCCCTACCAACTGGTCGGGGTTTGAAAC
Vax1-201_288-310	**AAAGAGGGGAAAGAGGGAAA***GG*GTTTCAAACCCCGACCAGTT

Fill-in PCR was performed in order to generate gRNA for *vax1-201* degradation as previously described (Kushawah et al., 2020). The reaction utilized 5X GoTaq PCR buffer

(Promega M791A), GoTaq DNA polymerase (Promega M300A), Promega PCR Nucleotide Mix, 10 mM (Promega U144A), and each of the designed primers (Appendix X.4 for details). PCR was conducted using an Eppendorf Mastercycler personal thermocycler, with the following program: initial denaturation at 94°C for 4 minutes; 30 cycles of 94°C for 30 seconds, 60°C for 40 seconds, 72°C for 30 seconds; final extension at 72°C for 10 minutes (Appendix E for full protocol).

PCR products were verified via electrophoresis using a 2% agarose TAE gel and a 2% agarose, 1% bleach TAE gel, each run at 80V for 90 minutes (See Appendix E for details on gel preparation and electrophoresis). Gel imaging and analysis were done using a Gel-Doc EZ Imager and ImageLab software (Bio-Rad). Estimations of PCR product length and concentration were done via comparison to Promega 50 base pair DNA ladder (Promega G452A). gRNA templates were purified via emulsion in Roche High Pure PCR Product Purification Kit (Sigma 11732668001) binding buffer, and subsequent ethanol precipitation of DNA from the emulsified gel. Precipitated DNA was then reconstituted in nuclease free water (IDT 11-05-01-14). For the purification protocol see Appendix E. Sequencing of the gRNA templates was done with help from the Sanger Sequencing Institute at the Sick Kids Hospital (Toronto, Ontario).

A.5 Results

A.5.1 pET-28b-RfxCas13d-His Restriction Digest and Sequencing

In order to confirm the identity of the isolated plasmid, a double restriction enzyme digest using both BGLII and NotI was performed. With a total length of 8160 base pairs (bp), it was predicted that double digestion with BGLII and NotI would produce two fragments of approximately 5 kilobase pairs (kb) and 3 kb (via restriction at 2695 and 5728 positions),

respectively. Following electrophoresis, the digested sample presented two distinct bands at approximately 5 kb and 3kb (Figure A.1), providing evidence that the isolated plasmid was indeed pET-28b-RfxCas13d-His.

A sequencing output provided by the Sick Kids Hospital further supported this evidence. Sequencing utilizing primers for the promotor regions flanking the RfxCas13d-His insert (T7 and T7 terminator) indicated a high degree of similarity between the submitted plasmid and the sequence that was submitted in the Addgene database (Kushawah et al., 2020). Specifically, nucleotide BLAST indicated a 98.01% and 98.40% base pair similarity for 1251 base and 1225 base spans of the RfxCas13d-His insert originating from the T7 and T7-terminator promotors, respectively (Figure A.2). Sequence quality plots for both reactions are shown, indicating higher quality in sequencing proximal to the promotor regions with quality tapering off at the distal extent of the sequenced portion (Figure A.2 A, B). In addition to restriction enzyme digestion, the results generated from sequencing suggest successful isolate of the pET-28b-RfxCas13d-His plasmid.

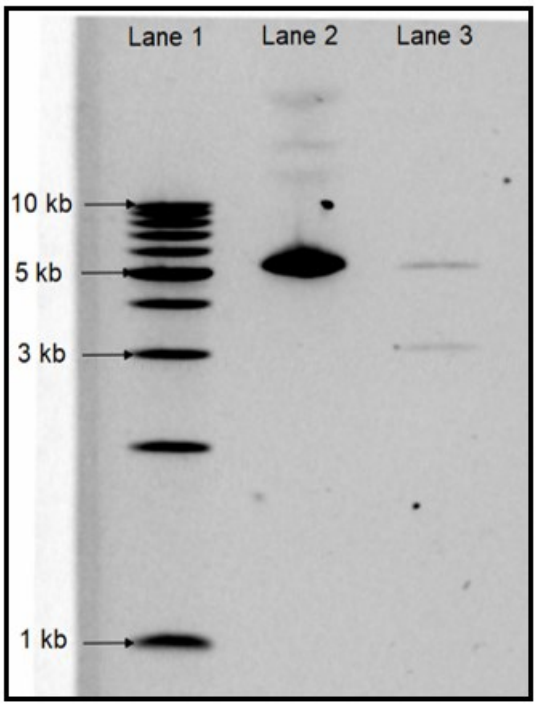

Figure A.1. *pET-28b-RfxCas13d-His BGLII and NotI double digest. Lane 1, 1 kb DNA ladder with 10 kb, 5 kb, 3 kb, and 1kb steps indicated. Lane 2, unrestricted pET-28b-RfxCas13d-His plasmid. Lane 3, pET-28b-RfxCas13d-His plasmid digested with BGLII and NotI. Multiple bands in Lane 2 indicate various plasmid conformations, with the majority taking on a supercoiled confirmation at approximately 5.5 kb. Two bands can be seen in Lane 3, indicating 5 kb and 3 kb fragments.*

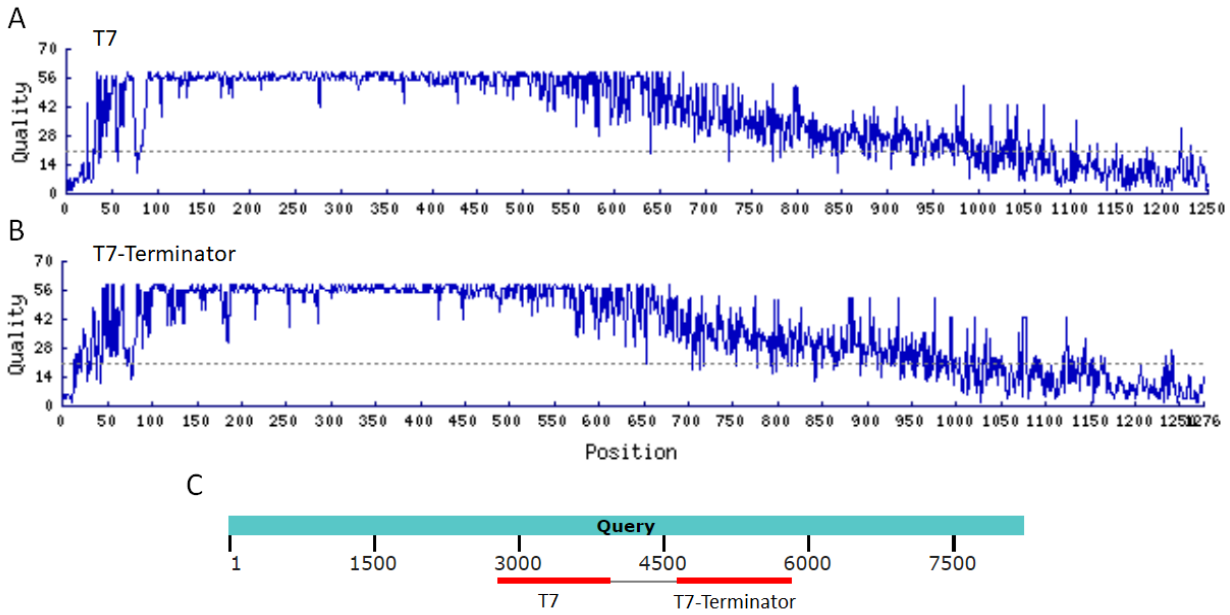

Figure A.2. *Sequencing quality and BLASTn alignment for T7 and T7-terminator primer sequencing reactions. A, B, Sequence quality plots for T7 and T7-terminator primer reactions, respectively. Dotted line indicates Q20 (quality of 20) threshold. C, BLASTn alignment for T7 and T7-terminator primer reaction sequences, indicating high-similarity alignment of generated sequences to database pET-28b-RfxCas13d-His sequence, along with predicted positioning (i.e. flanking the RfxCas13d-His insert which approximately spans bases 2715-5830. Teal bar represents pET-28b-RfxCas13d-His sequence, red bars indicate generated sequences.*

A.5.2 gRNA Template Design

In order to generate gRNA suitable for *Vax1* knockdown, the secondary structure of the *vax1-201* transcript (GenBank: BC065951) was visualized using RNAfold software, and a protospacer region target was chosen due to low base pairing probability. The target region spanned bases 288-310. The sequence can be found below in Table A.1. Based on the low probability of secondary structure binding, the 288-310 region of the *vax1-201* transcript

provides a suitable target site for CRISPR-Cas13d degradation. Thus, primers were designed for gRNA template synthesis (Table A.1).

A.5.3 gRNA Template Synthesis

PCR was performed using the primers shown in Table 5.1 to generate gRNA templates for cleavage of the 288-310 region of the *vax1-201* transcript (Appendix E for detailed protocol). Electrophoresis of the synthesized gRNA template indicated the presence of a PCR product of approximately 50 base pairs under non-reducing conditions, and 70 base pairs under reducing conditions (Figure A.3). This difference is likely due to the presence of a highly-probably hair-pin secondary structure in the gRNA template within the direct-repeat region (Figure A.3). Thus, it is highly likely that the gRNA template was successfully synthesized.

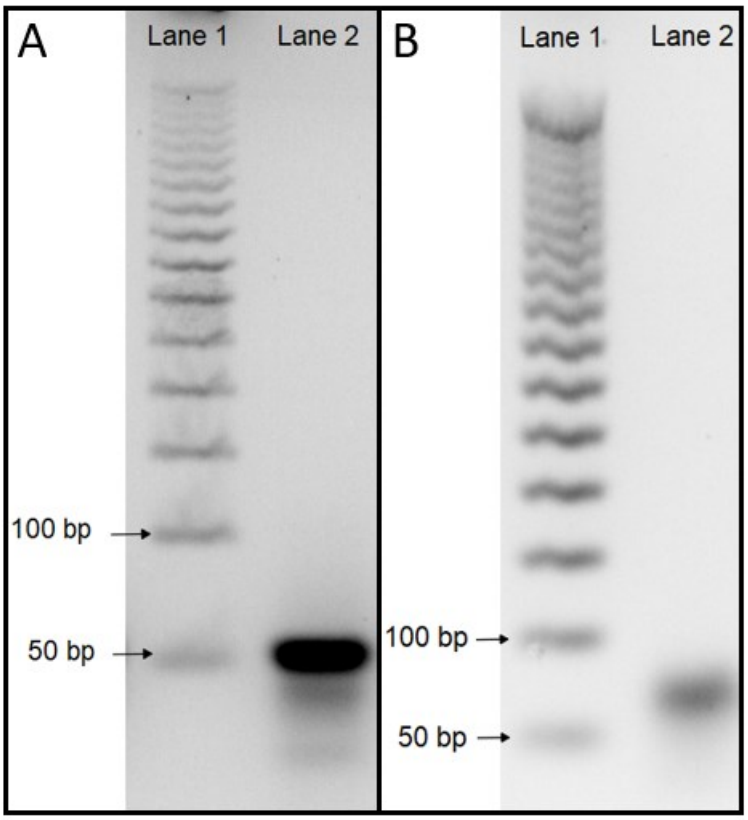

Figure A.3. *Vax1-201_288-310 gRNA template synthesis verification. A, gel electrophoresis verification with 2% agarose TAE gel; product band indicated at approximately 50 base pairs. B, gel electrophoresis verification with 2% agarose, 1% bleach TAE gel; product band indicated at approximately 70 base pairs.*

The synthesized gRNA template was sent to the Sanger Sequencing Institute at the Sick Kids Hospital (Toronto, Ontario) for sequencing. However, this was unsuccessful, likely due to the short length of the product. Due to time constraints, further workup to successfully sequence the product was not attempted.

A.6 Discussion

In order to investigate the involvement of the RPE in scleral cartilage induction and morphogenesis, the CRISPR-Cas13d knockdown method was conducted in order to induce ocular coloboma via microinjection in zebrafish embryos. I had hypothesized that knockdown of *vax1* signaling via CRISPR-Cas13 will lead to ocular coloboma in zebrafish, and that incomplete fusion on the ventral optic cup will lead to morphological disruption of the adjacent scleral cartilage. Knockdown of *vax1* transcripts via morpholino treatment had previously been used to produce such an effect (Take-uchi et al., 2003). However, due to potential off-target effects with morpholino usage, such as non-specific binding and toxicological effects (Gerety & Wilkinson, 2011; Gentsch et al., 2018; Cunningham et al., 2020), CRISPR-Cas13d knockdown was opted for as a more specific method (Kushawah et al., 2020). While significant progress has been made towards this objective, a shift in effort was made towards the other objectives in this thesis.

The utility of morpholino based knock-downs to study gene signaling during development has been the subject of question since its inception (Eisen & Smith, 2008). While knock-downs can be confirmed via downstream methods such as RT-qPCR or western blot, researchers remain weary of potential non-specific or off-target effects (Eisen & Smith, 2008; Blum et al., 2015). Recent studies have substantiated this possibility, demonstrating that off-target and toxicological effects could result from morpholino treatment (Gerety & Wilkinson, 2011; Gentsch et al., 2018; Cunningham et al., 2020). While the use of morpholinos has been indispensable to developmental research, these factors must be taken into consideration when interpreting results of morpholino experiments.

CRISPR-Cas13d knockdown, similarly to CRISPR-Cad9 knockout, functions via nuclease activity at a site designated by conjugated gRNA. Thus, preparation for microinjection

consists of synthesis of *cas13d* mRNA, and a gRNA designed to bind the transcript of interest. In this case, a gRNA was designed to target the zebrafish *vax1-201* transcript. A DNA template was synthesized via fill-in PCR and verified via agarose gel electrophoresis. Interestingly, initial verification indicated a product smaller than the predicted length. (50 bp instead of 70 bp). However, Cas protein gRNA contains a direct-repeat conjugation region which takes on a hairpin secondary structure. Thus, it was hypothesized that this structure would also exist in the complementary DNA template. Indeed, this was confirmed by running the template on a bleach gel (Aranda et al., 2012), which denatured the DNA and caused the product band to run at 70 bp as predicted (Figure A.3). Interestingly, this technique was originally designed to be used for RNA electrophoresis, and searches for its use with DNA denaturation in the literature have been unsuccessful. While this method of DNA denaturation was successful, other methods exist in the literature such as denaturation via addition of NaOH and EDTA in gel preparation (Southern, 2002).

This work demonstrates the foundational steps in CRISPR-Cas13d experimental preparation. That is, preparation of the pET-28b-RfxCas13d-His plasmid and synthesis of a gRNA template. In order to complete this work, better characterization of the synthesized gRNA template would be necessary (i.e., successful sequencing), followed by preparation of RNA from both the plasmid insert and gRNA template would be necessary. In order to successfully sequence the gRNA template, it could be transformed into a vector, which would greatly increase the overall size of the product. Issues with sequencing arise when a molecule is under 100 bp, thus transform the gRNA into a vector would likely allow for efficient sequencing. Following mRNA synthesis, the products would be quantified, and injections could be performed. Injection RNA concentrations could initially be derived from the literature for zebrafish embryo injection

(Kushawah et al., 2020) and further optimized if necessary. Coloboma phenotype verification could be done with live fish at a timepoint later than 30-hpf (e.g., 48-hpf). After this timepoint, the optic fissure of zebrafish with typical development should be closed (Take-uchi et al., 2003; Brown et al., 2009; Kwan et al., 2012). For this experiment, both wildtype (non-injected) fish and fish injected with $gRNA^-$ solution, or Cas13d $mRNA^-$ solution should be included as controls. In doing so, any effects caused by either of the injection components would be apparent, due to the transparency of the zebrafish embryo. That is, a gap in the ventral RPE (which should accumulate a small degree of pigmentation) would be clearly visible in contrast to the largely transparent embryo.

A.6.1 Assessment.

In order to assess the effects of ocular coloboma on scleral cartilage morphology, bone and cartilage staining could be performed. Bone and cartilage staining could be performed at 6.0 mm SL, at which time the scleral cartilage ring is clearly visible in zebrafish. This would allow for an assessment of scleral cartilage morphology in the ventral portion of the eye, where disruptions would be expected.

Appendix B: Supplementary Information

Appendix B.1. Summary of Injection Optimization Experiments.

Background: In order to determine an appropriate timepoint and location for inhibitor injections (in Chapter 3), a trial experiment was performed in which fish were injected at 17-hpf, 20-hpf, 23-hpf, and 26-hpf. In addition to the intravitreal injections presented in this thesis, injections into the periocular region were performed at early timepoints in order to target migrating neural crest cells. Specifically, intravitreal injections were performed at 20-hpf, 23-hpf, and 26-hpf, while periocular injections were performed at 17-hpf and 20-hpf. Injections were done with the 0.25 mM and 0.5 mM concentrations of the LY-364947 inhibitor and 5% DMSO control solution. The number of embryos injected at each timepoint-treatment combination are shown in Table B.1. Overall, survival at 17-hpf and 20-hpf was very poor for both injection locations. Survival was slightly better with 23-hpf and 26-hpf intravitreal injections, thus these timepoints were chosen for use in later experiments (Chapter 3).

Table B.1. *Summary of trial injection experiments with LY-364947 and 5% DMSO at 17-hpf, 20-hpf, 23-hpf and 26-hpf. The number of embryos injected are indicated in the rows LY (n) and DMSO (n). The percentage of fish that survived to 5-dpf (~4 days post injection) are given LY (%) and DMSO (%).*

Timepoint	17 hpf				20 hpf				23 hpf				26 hpf			
Injection Site	Periocular		Intravitreal		Periocular		Intravitreal		Periocular		Intravitreal		Periocular		Intravitreal	
Concentration (mM)	0.25	0.5	0.25	0.5	0.25	0.5	0.25	0.5	0.25	0.5	0.25	0.5	0.25	0.5	0.25	0.5
LY (n)	5	12	-	-	12	9	10	9	-	-	16	12	-	-	17	10
DMSO (n)	10		-	-	10		10		-	-	10		-	-	8	10
LY (%)	0.0	0.0	-	-	0.0	0.0	0.0	11.1	-	-	0.0	8.3	-	-	41.2	10.0
DMSO (%)	0.0		-	-	0.0		20.0		-	-	10.0		-	-	50.0	10.0

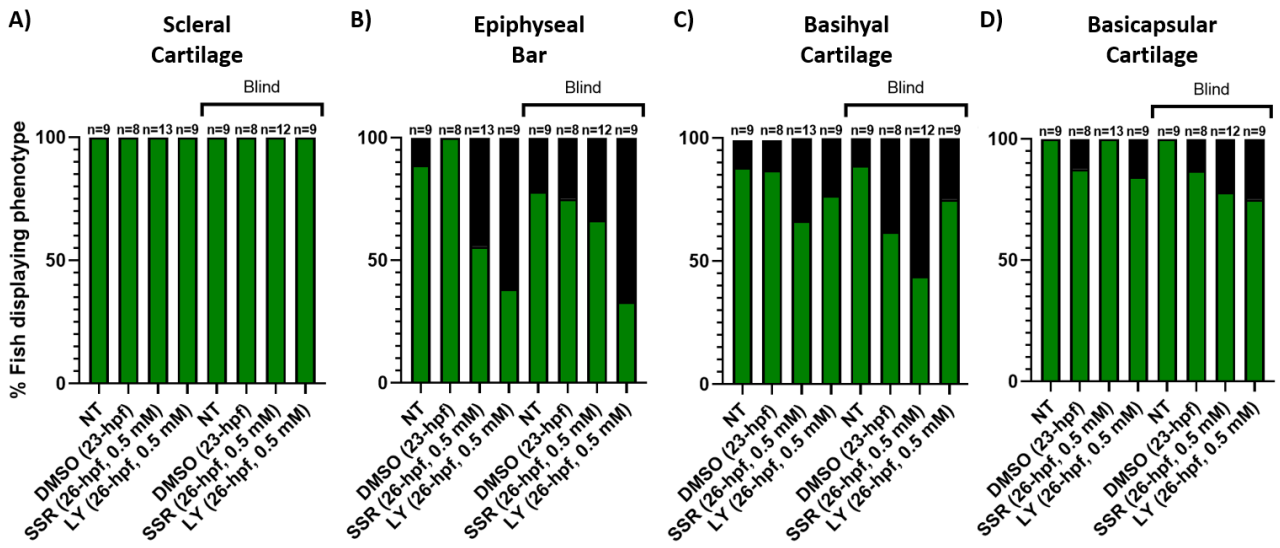

Figure B.1. *Sub-sample comparisons of initial and blind assessments of the scleral cartilage (A), epiphyseal bar (B), basihyal cartilage (C), and basicapsular cartilage (D). Blind assessments are indicated by a label above their respective bars. Samples sizes for each treatment group are indicated above their respective bars. Green bars represent the proportion of fish with normal morphology. Black bars represent the proportion of fish with abnormal or disrupted morphology. Blind bracket indicates observations that were made while blind to treatment groups.*

Appendix C: Raw Data

Appendix C.1: Raw eye width and eye depth data for surface tetras at 10-, 15-, 20-, and 30-dpf. Measurements were taken on three consecutive sections are for each fish. Surface T., Surface tetra.

Eye ID				Eye Measures (µm)					
Age	Type	Sample	Slide	Eye Width (section 1)	Eye Width (section 2)	Eye Width (section 3)	Eye Depth (section 1)	Eye Depth (section 2)	Eye Depth (section 3)
10	Surface T.	1	5	218.67	218.20	202.97	100.76	96.24	105.47
10	Surface T.	1	6	225.28	222.93	213.25	109.18	104.16	109.89
10	Surface T.	2	3	287.07	261.29	281.74	125.23	106.34	120.67
10	Surface T.	2	4	266.38	251.30	264.41	128.88	121.29	126.42
10	Surface T.	3	4	214.27	213.44	212.44	107.96	108.52	109.17
10	Surface T.	4	5	230.91	227.44	222.44	101.82	103.16	105.86
10	Surface T.	4	6	210.77	203.66	208.77	136.76	130.42	131.59
10	Surface T.	5	3	241.73	239.95	239.51	115.21	116.83	118.58
10	Surface T.	5	3	230.14	229.78	228.97	121.30	116.28	114.46
10	Surface T.	6	4	225.58	222.97	222.46	107.91	105.73	106.33
10	Surface T.	7	2	231.41	227.07	231.24	111.32	106.77	118.02
10	Surface T.	7	3	235.24	229.04	228.05	121.01	119.49	125.86
15	Surface T.	1	6	308.91	308.03	308.50	135.10	141.75	131.10
15	Surface T.	1	6	313.74	312.31	312.60	122.57	122.12	119.39
15	Surface T.	2	3	345.49	345.05	343.56	166.85	166.82	160.79
15	Surface T.	3	4	322.63	316.54	321.42	140.17	141.42	145.09
15	Surface T.	3	4	323.04	316.80	319.98	135.77	135.12	140.85
15	Surface T.	4	5	325.41	321.02	321.74	167.04	168.54	166.33
15	Surface T.	4	6	327.42	324.84	329.32	157.68	152.91	156.86
15	Surface T.	5	4	348.09	332.69	337.91	158.56	152.65	156.78
15	Surface T.	5	4	333.00	332.22	330.14	154.49	152.36	151.48
15	Surface T.	6	3	354.58	347.91	341.09	150.15	157.06	148.32
15	Surface T.	6	4	348.40	337.71	335.35	152.67	141.67	147.22
15	Surface T.	7	7	329.34	323.10	319.74	116.84	125.73	124.67
20	Surface T.	1	6	326.82	-	317.63	113.78	-	113.46
20	Surface T.	2	4	330.19	327.47	321.43	133.65	132.87	135.07
20	Surface T.	2	6	327.17	312.37	323.97	145.01	118.49	135.61
20	Surface T.	3	6	392.14	379.01	381.08	162.15	157.19	160.62
20	Surface T.	3	6	380.45	379.56	379.10	151.15	147.36	150.74
20	Surface T.	4	6	374.96	372.46	374.27	175.14	159.05	168.82
20	Surface T.	4	6	369.69	365.50	362.08	167.47	158.88	161.83
20	Surface T.	5	5	421.28	420.68	416.09	150.36	146.34	152.98
20	Surface T.	5	5	430.78	426.55	420.38	143.13	146.59	140.61
20	Surface T.	6	5	391.22	390.90	390.27	168.41	155.09	171.57
20	Surface T.	7	2	386.38	377.73	384.10	156.17	153.55	148.75
20	Surface T.	7	4	379.59	370.94	376.84	153.25	155.76	152.18
30	Surface T.	1	7	419.57	401.00	403.52	188.97	179.45	186.00
30	Surface T.	1	7	393.79	392.32	382.35	186.81	192.02	187.29
30	Surface T.	2	4	398.76	389.72	390.71	165.95	159.79	156.84
30	Surface T.	2	4	389.30	387.98	373.60	181.18	180.44	182.86

Appendix C.2: Raw eye width and eye depth data for cave tetras at 10-, 15-, 20-, and 30-dpf. Measurements were taken on three consecutive sections are for each fish. Cave T., cavefish (blind Pachón cave morph of tetra).

Eye ID				Eye Measures (µm)					
Age	Type	Sample	Slide	Eye Width (section 1)	Eye Width (section 2)	Eye Width (section 3)	Eye Depth (section 1)	Eye Depth (section 2)	Eye Depth (section 3)
10	Cave T.	1	8	119.38	126.09	-	50.27	55.45	-
10	Cave T.	3	3	147.99	138.43	141.79	69.21	51.57	61.17
10	Cave T.	3	4	148.18	142.89	139.28	62.25	56.44	56.57
10	Cave T.	5	2	157.70	156.92	150.19	47.40	45.50	45.80
10	Cave T.	5	2	150.36	146.94	149.56	56.05	39.16	42.12
10	Cave T.	6	7	164.60	150.75	156.83	39.53	30.77	45.69
10	Cave T.	6	8	140.44	135.19	-	70.05	45.19	-
15	Cave T.	3	8	137.70	119.83	146.41	59.62	46.83	67.37
15	Cave T.	3	9	136.55	130.57	133.64	63.01	53.95	58.06
15	Cave T.	4	3	128.31	111.96	125.20	50.40	43.42	43.55
15	Cave T.	4	4	127.78	115.23	127.20	42.86	37.50	40.58
15	Cave T.	5	5	112.79	116.57	109.79	51.61	50.21	57.34
20	Cave T.	2	7	155.44	146.59	152.71	43.89	38.71	38.08
20	Cave T.	2	7	121.36	107.41	-	57.51	54.73	-
20	Cave T.	3	8	147.97	148.91	146.31	58.92	63.88	66.57
20	Cave T.	3	9	166.78	165.35	167.48	83.15	74.33	80.96
20	Cave T.	4	7	124.45	130.35	120.99	66.69	59.95	58.37
20	Cave T.	4	8	142.22	137.36	131.31	60.92	61.13	55.02
20	Cave T.	5	4	149.02	142.65	154.76	73.83	61.53	73.67
20	Cave T.	5	5	166.75	163.25	162.28	72.69	76.84	74.18
30	Cave T.	1	6	153.22	163.90	138.23	58.22	50.88	68.21
30	Cave T.	2	6	164.28	164.73	147.10	59.99	58.21	69.96
30	Cave T.	2	7	172.55	181.29	164.97	65.04	56.65	52.95

Appendix C.3: Raw eye width and eye depth data for zebrafish at 10-, 15-, 20-, and 30-dpf. Measurements were taken on three consecutive sections are for each fish. Zebra, zebrafish.

Eye ID				Eye Measures (µm)					
Age	Type	Sample	Slide	Eye Width (section 1)	Eye Width (section 2)	Eye Width (section 3)	Eye Depth (section 1)	Eye Depth (section 2)	Eye Depth (section 3)
10	Zebra	1	2	271.85	260.83	273.08	126.98	134.77	124.13
10	Zebra	1	2	256.46	272.24	266.59	140.66	130.25	131.05
10	Zebra	2	3	246.16	249.61	249.08	113.37	111.35	119.45
10	Zebra	2	3	234.73	234.53	245.23	122.60	125.60	119.62
10	Zebra	3	1	267.73	259.66	255.45	133.76	129.16	131.04
10	Zebra	3	2	254.38	257.45	262.55	135.41	128.10	129.93
10	Zebra	5	1	262.37	250.16	249.90	137.08	157.50	154.64
10	Zebra	5	2	285.48	282.34	280.67	125.98	126.37	129.86
10	Zebra	6	3	250.98	247.01	243.97	117.36	115.49	115.80
10	Zebra	6	3	254.82	231.63	239.26	121.25	132.42	131.44
10	Zebra	7	3	251.10	253.72	246.06	120.93	132.98	126.34
10	Zebra	7	3	259.14	250.84	264.48	109.05	119.36	111.63
15	Zebra	1	2	314.44	317.58	325.41	139.99	137.56	147.76
15	Zebra	1	3	322.48	331.64	349.89	144.99	145.53	165.96
15	Zebra	2	2	294.60	287.04	293.85	133.43	124.60	128.25
15	Zebra	2	3	291.16	306.29	295.45	135.60	138.73	134.24
15	Zebra	3	4	327.58	330.39	327.49	131.66	139.65	138.11
15	Zebra	3	4	320.13	324.54	324.48	158.49	154.37	154.75
15	Zebra	4	3	326.69	324.75	319.69	147.16	152.80	160.75
15	Zebra	4	3	310.36	317.17	310.51	153.02	160.31	152.83
15	Zebra	5	3	352.51	361.32	348.52	147.46	154.06	155.24
15	Zebra	5	4	346.18	351.03	348.12	160.88	175.25	165.98
15	Zebra	6	5	326.08	320.23	321.34	133.45	134.04	124.91
15	Zebra	6	5	310.45	309.86	312.59	138.87	137.37	131.23
15	Zebra	7	1	290.91	289.29	291.02	132.85	118.02	127.29
20	Zebra	1	4	371.23	369.84	370.75	179.78	180.04	186.46
20	Zebra	1	5	360.64	354.55	352.79	167.58	171.92	163.13
20	Zebra	2	2	365.00	365.10	372.54	164.71	159.68	174.67
20	Zebra	2	3	365.64	362.07	362.91	162.62	159.84	162.27
20	Zebra	3	3	452.70	448.53	446.40	199.46	191.69	197.14
20	Zebra	3	4	455.32	451.54	455.82	178.41	179.20	174.20
20	Zebra	5	3	438.31	432.97	439.88	201.43	196.84	205.23
20	Zebra	5	3	448.74	450.50	450.07	197.04	191.49	194.15
20	Zebra	6	2	442.93	442.30	439.48	187.44	188.74	181.72
20	Zebra	6	2	449.61	436.06	439.35	162.24	168.63	166.77
20	Zebra	7	3	408.89	402.56	405.31	185.92	187.08	177.83
20	Zebra	7	3	420.04	428.51	422.75	170.29	167.53	168.37
20	Zebra	8	3	386.49	381.86	381.95	174.31	172.17	179.45
20	Zebra	8	3	407.82	395.64	402.38	179.04	170.01	178.44
30	Zebra	1	3	497.43	500.78	490.27	207.32	198.51	211.44
30	Zebra	1	3	503.35	489.26	486.74	209.90	226.61	226.98
30	Zebra	2	7	449.23	441.42	458.45	171.61	159.92	159.33
30	Zebra	2	8	464.50	454.62	451.77	198.91	197.93	195.47
30	Zebra	3	2	440.14	437.54	449.25	198.44	208.32	209.49
30	Zebra	3	3	445.50	446.05	440.16	188.51	187.44	192.31
30	Zebra	4	3	422.87	438.90	414.64	169.01	160.20	163.76
30	Zebra	4	4	424.44	418.94	425.92	182.00	175.18	176.50
30	Zebra	5	2	422.39	425.73	419.33	191.02	179.76	188.50
30	Zebra	5	3	413.19	403.21	397.20	172.84	184.85	179.12

Appendix C.4: Raw scleral cartilage depth data for surface tetras at 10-, 15-, 20-, and 30-dpf. Measurements were taken on three consecutive sections are for each fish in the rostral and caudal regions of the eye. Surface T., Surface tetra.

Eye ID				Scleral Cartilage Depth Measurments (µm)					
Age	Type	Sample	Slide	Rostral Depth (section 1)	Rostral Depth (section 2)	Rostral Depth (section 3)	Caudal Depth (section 1)	Caudal Depth (section 2)	Caudal Depth (section 3)
10	Surface T.	1	5	-	-	-	-	-	-
10	Surface T.	1	6	-	-	-	-	-	-
10	Surface T.	2	3	-	-	-	-	-	-
10	Surface T.	2	4	-	-	-	-	-	-
10	Surface T.	3	4	-	-	-	-	-	-
10	Surface T.	4	5	-	-	-	-	-	-
10	Surface T.	4	6	-	-	-	-	-	-
10	Surface T.	5	3	-	-	-	-	-	-
10	Surface T.	5	3	-	-	-	-	-	-
10	Surface T.	6	4	-	-	-	-	-	-
10	Surface T.	7	2	-	-	-	-	-	-
10	Surface T.	7	3	-	-	-	-	-	-
15	Surface T.	1	6	-	10.46	14.79	22.90	19.82	20.40
15	Surface T.	1	6	-	-	-	29.68	24.57	21.97
15	Surface T.	2	3	-	-	-	23.38	14.01	16.04
15	Surface T.	3	4	9.95	19.94	9.17	18.15	15.95	12.30
15	Surface T.	3	4	12.46	11.76	12.02	11.71	7.48	14.50
15	Surface T.	4	5	12.97	12.97	19.62	9.80	16.67	13.87
15	Surface T.	4	6	18.29	22.90	17.31	24.47	27.81	24.04
15	Surface T.	5	4	-	-	-	13.22	21.11	26.43
15	Surface T.	5	4	-	-	-	25.21	29.62	18.69
15	Surface T.	6	3	25.80	25.13	16.69	24.89	28.13	24.74
15	Surface T.	6	4	23.22	16.69	18.34	29.00	24.33	29.00
15	Surface T.	7	7	16.91	20.04	-	21.88	19.93	20.45
20	Surface T.	1	6	15.07	-	-	24.59	-	21.69
20	Surface T.	2	4	23.29	16.62	12.13	32.36	26.74	19.02
20	Surface T.	2	6	14.84	10.39	16.94	24.61	26.34	24.05
20	Surface T.	3	6	15.26	30.07	27.06	35.04	36.03	43.10
20	Surface T.	3	6	30.28	23.31	25.11	23.22	32.33	30.11
20	Surface T.	4	6	21.85	23.48	29.62	30.30	22.96	27.43
20	Surface T.	4	6	38.22	28.92	35.04	15.92	22.07	30.85
20	Surface T.	5	5	36.68	26.03	31.66	32.11	28.50	34.92
20	Surface T.	5	5	34.46	40.89	33.07	36.47	40.80	40.80
20	Surface T.	6	5	21.36	34.72	43.39	30.34	26.93	32.33
20	Surface T.	7	2	33.88	24.71	31.08	34.53	33.36	22.96
20	Surface T.	7	4	34.29	23.48	29.88	27.72	25.49	42.46
30	Surface T.	1	7	24.95	20.41	21.85	35.28	35.32	33.95
30	Surface T.	1	7	34.64	33.42	35.66	34.32	31.53	36.47
30	Surface T.	2	4	25.32	26.96	24.08	29.99	27.06	37.46
30	Surface T.	2	4	38.74	28.92	40.92	38.48	32.52	42.30

Appendix C.5: Raw scleral cartilage depth data for cave tetras at 10-, 15-, 20-, and 30-dpf. Measurements were taken on three consecutive sections are for each fish in the rostral and caudal regions of the eye. Cave T., cavefish (blind Pachón cave morph of tetra).

Eye ID				Scleral Cartilage Depth Measurments (µm)					
Age	Type	Sample	Slide	Rostral Depth (section 1)	Rostral Depth (section 2)	Rostral Depth (section 3)	Caudal Depth (section 1)	Caudal Depth (section 2)	Caudal Depth (section 3)
10	Cave T.	1	8	-	-	-	-	-	-
10	Cave T.	3	3	-	-	-	-	-	-
10	Cave T.	3	4	-	-	-	-	-	-
10	Cave T.	5	2	-	-	-	-	-	-
10	Cave T.	5	2	-	-	-	-	-	-
10	Cave T.	6	7	-	-	-	-	-	-
10	Cave T.	6	8	-	-	-	-	-	-
15	Cave T.	3	8	-	-	-	-	-	-
15	Cave T.	3	9	-	-	-	-	-	-
15	Cave T.	4	3	-	14.87	-	13.05	17.99	14.20
15	Cave T.	4	4	-	-	-	20.87	17.37	10.25
15	Cave T.	5	5	-	-	-	11.74	14.05	-
20	Cave T.	2	7	-	-	-	-	-	-
20	Cave T.	2	7	-	-	-	25.56	26.19	-
20	Cave T.	3	8	-	-	-	23.51	20.06	25.14
20	Cave T.	3	9	-	-	-	-	-	-
20	Cave T.	4	7	-	-	16.83	25.19	33.16	18.56
20	Cave T.	4	8	-	-	-	40.00	20.06	37.28
20	Cave T.	5	4	31.28	16.45	12.18	27.20	32.46	13.70
20	Cave T.	5	5	15.17	20.30	-	28.87	26.20	24.15
30	Cave T.	1	6	47.68	41.51	57.01	42.86	40.09	56.10
30	Cave T.	2	6	29.35	29.40	33.48	43.15	49.19	52.03
30	Cave T.	2	7	58.86	9.93	46.51	50.41	53.27	39.61

Appendix C.6: Raw scleral cartilage depth data for zebrafish at 10-, 15-, 20-, and 30-dpf. Measurements were taken on three consecutive sections are for each fish in the rostral and caudal regions of the eye. Zebra, zebrafish.

Eye ID				Scleral Cartilage Depth Measurments (µm)					
Age	Type	Sample	Slide	Rostral Depth (section 1)	Rostral Depth (section 2)	Rostral Depth (section 3)	Caudal Depth (section 1)	Caudal Depth (section 2)	Caudal Depth (section 3)
10	Zebra	1	2	-	-	-	-	-	-
10	Zebra	1	2	-	-	-	-	-	-
10	Zebra	2	3	-	-	-	-	-	-
10	Zebra	2	3	-	-	-	-	-	-
10	Zebra	3	1	-	-	-	-	-	-
10	Zebra	3	2	-	-	-	-	-	-
10	Zebra	5	1	-	-	-	-	-	-
10	Zebra	5	2	-	-	-	-	-	-
10	Zebra	6	3	-	-	-	-	-	-
10	Zebra	6	3	-	-	-	-	-	-
10	Zebra	7	3	-	-	-	-	-	-
10	Zebra	7	3	-	-	-	-	-	-
15	Zebra	1	2	21.94	18.98	22.92	22.80	16.17	19.26
15	Zebra	1	3	20.34	25.57	20.80	24.94	20.80	20.37
15	Zebra	2	2	-	-	-	-	-	-
15	Zebra	2	3	-	-	-	-	-	-
15	Zebra	3	4	-	-	-	20.41	21.83	19.68
15	Zebra	3	4	-	-	-	16.53	-	18.27
15	Zebra	4	3	-	-	-	-	-	22.18
15	Zebra	4	3	20.20	24.17	16.32	11.13	18.00	16.95
15	Zebra	5	3	24.11	20.44	13.69	22.96	15.97	28.67
15	Zebra	5	4	17.93	20.28	27.17	27.56	33.60	43.87
15	Zebra	6	5	-	-	-	14.89	-	15.17
15	Zebra	6	5	-	-	-	-	-	-
15	Zebra	7	1	-	-	-	-	-	-
20	Zebra	1	4	19.37	27.54	21.74	31.19	25.13	33.90
20	Zebra	1	5	25.48	25.83	23.39	27.68	27.28	28.61
20	Zebra	2	2	-	-	-	49.60	48.21	41.09
20	Zebra	2	3	16.34	16.48		47.19	57.34	38.74
20	Zebra	3	3	53.72	43.46	48.77	60.52	59.63	54.38
20	Zebra	3	4	40.05	37.48	40.25	46.36	45.96	46.64
20	Zebra	5	3	40.18	38.52	45.64	56.79	58.31	51.42
20	Zebra	5	3	34.54	40.53	37.03	69.05	71.23	70.06
20	Zebra	6	2	31.97	33.15	31.96	43.85	41.58	39.64
20	Zebra	6	2	40.05	37.25	34.00	36.73	44.10	37.39
20	Zebra	7	3	29.57	24.61	32.04	37.12	38.32	42.80
20	Zebra	7	3	33.69	30.24	30.83	43.01	40.89	44.03
20	Zebra	8	3	27.01	23.18	23.88	34.76	35.27	29.23
20	Zebra	8	3	14.34	17.11	11.22	51.89	46.13	49.13
30	Zebra	1	3	65.83	71.85	57.23	75.11	66.98	75.77
30	Zebra	1	3	48.28	55.34	50.92	82.89	86.03	79.84
30	Zebra	2	7	55.41	50.55	54.13	73.90	74.03	67.00
30	Zebra	2	8	54.69	52.32	55.22	82.60	77.13	76.68
30	Zebra	3	2	54.01	49.05	55.65	62.77	66.00	62.90
30	Zebra	3	3	48.93	44.86	52.01	76.26	79.61	78.66
30	Zebra	4	3	44.74	43.92	38.33	55.94	52.52	53.82
30	Zebra	4	4	40.34	42.10	43.03	53.51	56.78	49.81
30	Zebra	5	2	45.44	41.71	49.44	56.19	60.26	58.54
30	Zebra	5	3	46.65	41.03	49.80	68.50	62.49	60.78

Appendix C.7: Raw scleral cartilage cell count data for surface tetras at 10-, 15-, 20-, and 30-dpf. Counts were taken on three consecutive sections are for each fish in the rostral and caudal regions of the eye. Surface T., Surface tetra.

Eye ID				Scleral Cartilage Cell Count (# of cells)					
Age	Type	Sample	Slide	Rostral Count (section 1)	Rostral Count (section 2)	Rostral Count (section 3)	Caudal Count (section 1)	Caudal Count (section 2)	Caudal Count (section 3)
10	Surface T.	1	5	-	-	-	-	-	-
10	Surface T.	1	6	-	-	-	-	-	-
10	Surface T.	2	3	-	-	-	-	-	-
10	Surface T.	2	4	-	-	-	-	-	-
10	Surface T.	3	4	-	-	-	-	-	-
10	Surface T.	4	5	-	-	-	-	-	-
10	Surface T.	4	6	-	-	-	-	-	-
10	Surface T.	5	3	-	-	-	-	-	-
10	Surface T.	5	3	-	-	-	-	-	-
10	Surface T.	6	4	-	-	-	-	-	-
10	Surface T.	7	2	-	-	-	-	-	-
10	Surface T.	7	3	-	-	-	-	-	-
15	Surface T.	1	6	-	1	1	2	2	2
15	Surface T.	1	6	-	-	-	3	2	3
15	Surface T.	2	3	-	-	-	2	1	2
15	Surface T.	3	4	1	2	1	3	2	1
15	Surface T.	3	4	2	1	1	2	1	1
15	Surface T.	4	5	2	1	2	1	2	2
15	Surface T.	4	6	1	1	2	2	2	2
15	Surface T.	5	4	-	-	-	1	2	3
15	Surface T.	5	4	-	-	-	3	4	2
15	Surface T.	6	3	3	3	2	3	3	3
15	Surface T.	6	4	3	2	2	3	4	4
15	Surface T.	7	7	3	3	-	3	2	3
20	Surface T.	1	6	2	-	-	3	-	3
20	Surface T.	2	4	4	3	2	5	3	3
20	Surface T.	2	6	2	2	3	3	4	3
20	Surface T.	3	6	2	4	4	4	4	5
20	Surface T.	3	6	4	4	5	3	5	5
20	Surface T.	4	6	3	4	5	4	4	4
20	Surface T.	4	6	5	4	6	3	5	4
20	Surface T.	5	5	6	3	4	6	5	5
20	Surface T.	5	5	6	6	6	6	5	6
20	Surface T.	6	5	4	5	6	4	4	6
20	Surface T.	7	2	5	3	6	4	4	4
20	Surface T.	7	4	5	3	4	4	2	6
30	Surface T.	1	7	3	2	4	5	4	6
30	Surface T.	1	7	4	5	4	5	4	5
30	Surface T.	2	4	3	3	3	4	4	5
30	Surface T.	2	4	6	5	6	5	5	5

Appendix C.8: Raw scleral cartilage cell count data for surface tetras at 10-, 15-, 20-, and 30-dpf. Counts were taken on three consecutive sections are for each fish in the rostral and caudal regions of the eye. Cave T., cavefish (blind Pachón cave morph of tetra).

Eye ID				Scleral Cartilage Cell Count (# of cells)					
Age	Type	Sample	Slide	Rostral Count (section 1)	Rostral Count (section 2)	Rostral Count (section 3)	Caudal Count (section 1)	Caudal Count (section 2)	Caudal Count (section 3)
10	Cave T.	1	8	-	-	-	-	-	-
10	Cave T.	3	3	-	-	-	-	-	-
10	Cave T.	3	4	-	-	-	-	-	-
10	Cave T.	5	2	-	-	-	-	-	-
10	Cave T.	5	2	-	-	-	-	-	-
10	Cave T.	6	7	-	-	-	-	-	-
10	Cave T.	6	8	-	-	-	-	-	-
15	Cave T.	3	8	-	-	-	-	-	-
15	Cave T.	3	9	-	-	-	-	-	-
15	Cave T.	4	3	-	2	-	2	2	2
15	Cave T.	4	4	-	-	-	3	2	2
15	Cave T.	5	5	-	-	-	1	2	-
20	Cave T.	2	7	-	-	-	-	-	-
20	Cave T.	2	7	-	-	-	3	3	-
20	Cave T.	3	8	-	-	-	3	4	4
20	Cave T.	3	9	-	-	-	-	-	-
20	Cave T.	4	7	-	-	2	3	5	2
20	Cave T.	4	8	-	-	-	5	2	4
20	Cave T.	5	4	4	2	2	4	5	1
20	Cave T.	5	5	3	3	-	5	4	3
30	Cave T.	1	6	5	4	9	6	5	8
30	Cave T.	2	6	4	3	6	6	7	9
30	Cave T.	2	7	8	2	8	8	8	6

Appendix C.9: Raw scleral cartilage cell count data for zebrafish at 10-, 15-, 20-, and 30-dpf. Counts were taken on three consecutive sections are for each fish in the rostral and caudal regions of the eye. Zebra, zebrafish.

Eye ID				Scleral Cartilage Cell Count (# of cells)					
Age	Type	Sample	Slide	Rostral Count (section 1)	Rostral Count (section 2)	Rostral Count (section 3)	Caudal Count (section 1)	Caudal Count (section 2)	Caudal Count (section 3)
10	Zebra	1	2	-	-	-	-	-	-
10	Zebra	1	2	-	-	-	-	-	-
10	Zebra	2	3	-	-	-	-	-	-
10	Zebra	2	3	-	-	-	-	-	-
10	Zebra	3	1	-	-	-	-	-	-
10	Zebra	3	2	-	-	-	-	-	-
10	Zebra	5	1	-	-	-	-	-	-
10	Zebra	5	2	-	-	-	-	-	-
10	Zebra	6	3	-	-	-	-	-	-
10	Zebra	6	3	-	-	-	-	-	-
10	Zebra	7	3	-	-	-	-	-	-
10	Zebra	7	3	-	-	-	-	-	-
15	Zebra	1	2	3	3	4	4	2	3
15	Zebra	1	3	4	4	4	4	4	4
15	Zebra	2	2	-	-	-	-	-	-
15	Zebra	2	3	-	-	-	-	-	-
15	Zebra	3	4	-	-	-	4	4	4
15	Zebra	3	4	-	-	-	3	-	3
15	Zebra	4	3	-	-	-	-	-	4
15	Zebra	4	3	3	4	2	2	3	2
15	Zebra	5	3	4	3	2	5	3	5
15	Zebra	5	4	4	4	5	5	6	8
15	Zebra	6	5	-	-	-	2	-	2
15	Zebra	6	5	-	-	-	-	-	-
15	Zebra	7	1	-	-	-	-	-	-
20	Zebra	1	4	2	4	3	6	4	6
20	Zebra	1	5	6	4	4	4	4	4
20	Zebra	2	2	-	-	-	9	8	8
20	Zebra	2	3	3	3		9	9	7
20	Zebra	3	3	8	8	9	11	11	11
20	Zebra	3	4	7	6	6	7	8	8
20	Zebra	5	3	6	7	6	12	11	12
20	Zebra	5	3	7	6	7	13	15	15
20	Zebra	6	2	7	6	5	7	8	8
20	Zebra	6	2	7	7	5	8	7	8
20	Zebra	7	3	5	5	6	6	7	7
20	Zebra	7	3	6	6	5	6	7	8
20	Zebra	8	3	5	4	3	6	5	5
20	Zebra	8	3	3	2	2	11	7	11
30	Zebra	1	3	11	13	11	11	12	11
30	Zebra	1	3	7	9	9	15	15	18
30	Zebra	2	7	9	9	10	14	12	12
30	Zebra	2	8	10	9	9	12	14	12
30	Zebra	3	2	8	8	9	10	10	10
30	Zebra	3	3	9	6	10	13	13	13
30	Zebra	4	3	6	7	4	8	9	8
30	Zebra	4	4	7	8	6	10	8	8
30	Zebra	5	2	7	7	8	10	9	9
30	Zebra	5	3	7	7	8	13	10	9

Appendix C10: Averaged eye width, eye depth, scleral cartilage depth, cell count and relative depth, for surface tetras at 10-, 15-, 20-, and 30-dpf. Averages were calculated with measurements from three consecutive sections are for each fish in the rostral and caudal regions of the eye. Values in the average columns were determined by taking the average of the rostral and caudal values. Relative scleral cartilage depth was determined using the following formula [(average scleral cartilage depth / average eye depth) * 100%].

Eye ID				Eye Size Averages (µm)		Scleral Cartilage Cell Count Averages (# of cells)			Scleral Cartilage Depth Averages (µm)			Relative Scleral Cartilage Depth
Age	Type	Sample	Slide	Eye Width	Eye Depth	Rostral	Caudal	Average	Rostral	Caudal	Average	(%)
10	Surface T.	1	5	213.3	100.8	0.0	0.0	0.0	0.0	0.0	0.0	0.0
10	Surface T.	1	6	220.5	107.7	0.0	0.0	0.0	0.0	0.0	0.0	0.0
10	Surface T.	2	3	276.7	117.4	0.0	0.0	0.0	0.0	0.0	0.0	0.0
10	Surface T.	2	4	260.7	125.5	0.0	0.0	0.0	0.0	0.0	0.0	0.0
10	Surface T.	3	4	213.4	108.6	0.0	0.0	0.0	0.0	0.0	0.0	0.0
10	Surface T.	4	5	226.9	103.6	0.0	0.0	0.0	0.0	0.0	0.0	0.0
10	Surface T.	4	6	207.7	132.9	0.0	0.0	0.0	0.0	0.0	0.0	0.0
10	Surface T.	5	3	240.4	116.9	0.0	0.0	0.0	0.0	0.0	0.0	0.0
10	Surface T.	5	3	229.6	117.3	0.0	0.0	0.0	0.0	0.0	0.0	0.0
10	Surface T.	6	4	223.7	106.7	0.0	0.0	0.0	0.0	0.0	0.0	0.0
10	Surface T.	7	2	229.9	112.0	0.0	0.0	0.0	0.0	0.0	0.0	0.0
10	Surface T.	7	3	230.8	122.1	0.0	0.0	0.0	0.0	0.0	0.0	0.0
15	Surface T.	1	6	308.5	136.0	0.7	2.0	1.3	8.4	21.0	14.7	10.8
15	Surface T.	1	6	312.9	121.4	0.0	2.7	1.3	0.0	25.4	12.7	10.5
15	Surface T.	2	3	344.7	164.8	0.0	1.7	0.8	0.0	17.8	8.9	5.4
15	Surface T.	3	4	320.2	142.2	1.3	2.0	1.7	13.0	15.5	14.2	10.0
15	Surface T.	3	4	319.9	137.2	1.3	1.3	1.3	12.1	11.2	11.7	8.5
15	Surface T.	4	5	322.7	167.3	1.7	1.7	1.7	15.2	13.4	14.3	8.6
15	Surface T.	4	6	327.2	155.8	1.3	2.0	1.7	19.5	25.4	22.5	14.4
15	Surface T.	5	4	339.6	156.0	0.0	2.0	1.0	0.0	20.3	10.1	6.5
15	Surface T.	5	4	331.8	152.8	0.0	3.0	1.5	0.0	24.5	12.3	8.0
15	Surface T.	6	3	347.9	151.8	2.7	3.0	2.8	22.5	25.9	24.2	16.0
15	Surface T.	6	4	340.5	147.2	2.3	3.7	3.0	19.4	27.4	23.4	15.9
15	Surface T.	7	7	324.1	122.4	3.0	2.7	2.8	12.3	20.8	16.5	13.5
20	Surface T.	1	6	214.8	75.7	1.0	3.0	2.0	5.0	15.4	10.2	13.5
20	Surface T.	2	4	326.4	133.9	3.0	3.7	3.3	17.3	26.0	21.7	16.2
20	Surface T.	2	6	321.2	133.0	2.3	3.3	2.8	14.1	25.0	19.5	14.7
20	Surface T.	3	6	384.1	160.0	3.3	4.3	3.8	24.1	38.1	31.1	19.4
20	Surface T.	3	6	379.7	149.8	4.3	4.3	4.3	26.2	28.6	27.4	18.3
20	Surface T.	4	6	373.9	167.7	4.0	4.0	4.0	25.0	26.9	25.9	15.5
20	Surface T.	4	6	365.8	162.7	5.0	4.0	4.5	34.1	22.9	28.5	17.5
20	Surface T.	5	5	419.4	149.9	4.3	5.3	4.8	31.5	31.8	31.7	21.1
20	Surface T.	5	5	425.9	143.4	6.0	5.7	5.8	36.1	39.4	37.7	26.3
20	Surface T.	6	5	390.8	165.0	5.0	4.7	4.8	33.2	29.9	31.5	19.1
20	Surface T.	7	2	382.7	152.8	4.7	4.0	4.3	29.9	30.3	30.1	19.7
20	Surface T.	7	4	375.8	153.7	4.0	4.0	4.0	29.2	31.9	30.6	19.9
30	Surface T.	1	7	408.0	184.8	3.0	5.0	4.0	22.4	34.9	28.6	15.5
30	Surface T.	1	7	389.5	188.7	4.3	4.7	4.5	34.6	34.1	34.3	18.2
30	Surface T.	2	4	393.1	160.9	3.0	4.3	3.7	25.5	31.5	28.5	17.7
30	Surface T.	2	4	383.6	181.5	5.7	5.0	5.3	36.2	37.8	37.0	20.4

Appendix C.11: Averaged eye width, eye depth, scleral cartilage depth, cell count and relative depth, for cave tetras at 10-, 15-, 20-, and 30-dpf. Averages were calculated with measurements from three consecutive sections are for each fish in the rostral and caudal regions of the eye. Values in the average columns were determined by taking the average of the rostral and caudal values. Relative scleral cartilage depth was determined using the following formula [(average scleral cartilage depth / average eye depth) * 100%].

Eye ID				Eye Size Averages (µm)		Scleral Cartilage Cell Count Averages (# of cells)			Scleral Cartilage Depth Averages (µm)			Relative Scleral Cartilage Depth
Age	Type	Sample	Slide	Eye Width	Eye Depth	Rostral	Caudal	Average	Rostral	Caudal	Average	(%)
10	Cave T.	1	8	81.8	35.2	0.0	0.0	0.0	0.0	0.0	0.0	0.0
10	Cave T.	3	3	142.7	60.7	0.0	0.0	0.0	0.0	0.0	0.0	0.0
10	Cave T.	3	4	143.5	58.4	0.0	0.0	0.0	0.0	0.0	0.0	0.0
10	Cave T.	5	2	154.9	46.2	0.0	0.0	0.0	0.0	0.0	0.0	0.0
10	Cave T.	5	2	149.0	45.8	0.0	0.0	0.0	0.0	0.0	0.0	0.0
10	Cave T.	6	7	157.4	38.7	0.0	0.0	0.0	0.0	0.0	0.0	0.0
10	Cave T.	6	8	91.9	57.6	0.0	0.0	0.0	0.0	0.0	0.0	0.0
15	Cave T.	3	8	134.6	57.9	0.0	0.0	0.0	0.0	0.0	0.0	0.0
15	Cave T.	3	9	133.6	58.3	0.0	0.0	0.0	0.0	0.0	0.0	0.0
15	Cave T.	4	3	121.8	45.8	0.7	2.0	1.3	5.0	15.1	10.0	21.9
15	Cave T.	4	4	123.4	40.3	0.0	2.3	1.2	0.0	16.2	8.1	20.0
15	Cave T.	5	5	113.1	53.1	0.0	1.0	0.5	0.0	8.6	4.3	8.1
20	Cave T.	2	7	151.6	40.2	0.0	0.0	0.0	0.0	0.0	0.0	0.0
20	Cave T.	2	7	76.3	37.4	0.0	2.0	1.0	0.0	17.3	8.6	23.1
20	Cave T.	3	8	147.7	63.1	0.0	3.7	1.8	0.0	22.9	11.5	18.1
20	Cave T.	3	9	166.5	79.5	0.0	0.0	0.0	0.0	0.0	0.0	0.0
20	Cave T.	4	7	125.3	61.7	0.7	3.3	2.0	5.6	25.6	15.6	25.3
20	Cave T.	4	8	137.0	59.0	0.0	3.7	1.8	0.0	32.4	16.2	27.5
20	Cave T.	5	4	148.8	69.7	2.7	3.3	3.0	20.0	24.5	22.2	31.9
20	Cave T.	5	5	164.1	74.6	2.0	4.0	3.0	11.8	26.4	19.1	25.6
30	Cave T.	1	6	151.8	59.1	6.0	6.3	6.2	48.7	46.4	47.5	80.4
30	Cave T.	2	6	158.7	62.7	4.3	7.3	5.8	30.7	48.1	39.4	62.9
30	Cave T.	2	7	172.9	58.2	6.0	7.3	6.7	38.4	47.8	43.1	74.0

Appendix C.12: Averaged eye width, eye depth, scleral cartilage depth, cell count and relative depth, for zebrafish at 10-, 15-, 20-, and 30-dpf. Averages were calculated with measurements from three consecutive sections are for each fish in the rostral and caudal regions of the eye. Values in the average columns were determined by taking the average of the rostral and caudal values. Relative scleral cartilage depth was determined using the following formula [(average scleral cartilage depth / average eye depth) * 100%].

Eye ID				Eye Size Averages (µm)		Scleral Cartilage Cell Count Averages (# of cells)			Scleral Cartilage Depth Averages (µm)			Relative Scleral Cartilage Depth (%)
Age	Type	Sample	Slide	Eye Width	Eye Depth	Rostral	Caudal	Average	Rostral	Caudal	Average	
10	Zebra	1	2	268.6	128.6	0.0	0.0	0.0	0.0	0.0	0.0	0.0
10	Zebra	1	2	265.1	134.0	0.0	0.0	0.0	0.0	0.0	0.0	0.0
10	Zebra	2	3	248.3	114.7	0.0	0.0	0.0	0.0	0.0	0.0	0.0
10	Zebra	2	3	238.2	122.6	0.0	0.0	0.0	0.0	0.0	0.0	0.0
10	Zebra	3	1	260.9	131.3	0.0	0.0	0.0	0.0	0.0	0.0	0.0
10	Zebra	3	2	258.1	131.1	0.0	0.0	0.0	0.0	0.0	0.0	0.0
10	Zebra	5	1	254.1	149.7	0.0	0.0	0.0	0.0	0.0	0.0	0.0
10	Zebra	5	2	282.8	127.4	0.0	0.0	0.0	0.0	0.0	0.0	0.0
10	Zebra	6	3	247.3	116.2	0.0	0.0	0.0	0.0	0.0	0.0	0.0
10	Zebra	6	3	241.9	128.4	0.0	0.0	0.0	0.0	0.0	0.0	0.0
10	Zebra	7	3	250.3	126.8	0.0	0.0	0.0	0.0	0.0	0.0	0.0
10	Zebra	7	3	258.2	113.3	0.0	0.0	0.0	0.0	0.0	0.0	0.0
15	Zebra	1	2	319.1	141.8	3.3	3.0	3.2	21.3	19.4	20.3	14.4
15	Zebra	1	3	334.7	152.2	4.0	4.0	4.0	22.2	22.0	22.1	14.5
15	Zebra	2	2	291.8	128.8	0.0	0.0	0.0	0.0	0.0	0.0	0.0
15	Zebra	2	3	297.6	136.2	0.0	0.0	0.0	0.0	0.0	0.0	0.0
15	Zebra	3	4	328.5	136.5	0.0	4.0	2.0	0.0	20.6	10.3	7.6
15	Zebra	3	4	323.1	155.9	0.0	2.0	1.0	0.0	11.6	5.8	3.7
15	Zebra	4	3	323.7	153.6	0.0	1.3	0.7	0.0	7.4	3.7	2.4
15	Zebra	4	3	312.7	155.4	3.0	2.3	2.7	20.2	15.4	17.8	11.5
15	Zebra	5	3	354.1	152.3	3.0	4.3	3.7	19.4	22.5	21.0	13.8
15	Zebra	5	4	348.4	167.4	4.3	6.3	5.3	21.8	35.0	28.4	17.0
15	Zebra	6	5	322.6	130.8	0.0	1.3	0.7	0.0	10.0	5.0	3.8
15	Zebra	6	5	311.0	135.8	0.0	0.0	0.0	0.0	0.0	0.0	0.0
15	Zebra	7	1	290.4	126.1	0.0	0.0	0.0	0.0	0.0	0.0	0.0
20	Zebra	1	4	370.6	182.1	3.0	5.3	4.2	22.9	30.1	26.5	14.5
20	Zebra	1	5	356.0	167.5	4.7	4.0	4.3	24.9	27.9	26.4	15.7
20	Zebra	2	2	367.5	166.4	0.0	8.3	4.2	0.0	46.3	23.2	13.9
20	Zebra	2	3	363.5	161.6	3.0	8.3	5.7	16.4	47.8	32.1	19.9
20	Zebra	3	3	449.2	196.1	8.3	11.0	9.7	48.7	58.2	53.4	27.2
20	Zebra	3	4	454.2	177.3	6.3	7.7	7.0	39.3	46.3	42.8	24.1
20	Zebra	5	3	437.1	201.2	6.3	11.7	9.0	41.4	55.5	48.5	24.1
20	Zebra	5	3	449.8	194.2	6.7	14.3	10.5	37.4	70.1	53.7	27.7
20	Zebra	6	2	441.6	186.0	6.0	7.7	6.8	32.4	41.7	37.0	19.9
20	Zebra	6	2	441.7	165.9	6.3	7.7	7.0	37.1	39.4	38.3	23.1
20	Zebra	7	3	405.6	183.6	5.3	6.7	6.0	28.7	39.4	34.1	18.6
20	Zebra	7	3	423.8	168.7	5.7	7.0	6.3	31.6	42.6	37.1	22.0
20	Zebra	8	3	383.4	175.3	4.0	5.3	4.7	24.7	33.1	28.9	16.5
20	Zebra	8	3	401.9	175.8	2.3	9.7	6.0	14.2	49.1	31.6	18.0
30	Zebra	1	3	496.2	205.8	11.7	11.3	11.5	65.0	72.6	68.8	33.4
30	Zebra	1	3	493.1	221.2	8.3	16.0	12.2	51.5	82.9	67.2	30.4
30	Zebra	2	7	449.7	163.6	9.3	12.7	11.0	53.4	71.6	62.5	38.2
30	Zebra	2	8	457.0	197.4	9.3	12.7	11.0	54.1	78.8	66.4	33.7
30	Zebra	3	2	442.3	205.4	8.3	10.0	9.2	52.9	63.9	58.4	28.4
30	Zebra	3	3	443.9	189.4	8.3	13.0	10.7	48.6	78.2	63.4	33.5
30	Zebra	4	3	425.5	164.3	5.7	8.3	7.0	42.3	54.1	48.2	29.3
30	Zebra	4	4	423.1	177.9	7.0	8.7	7.8	41.8	53.4	47.6	26.8
30	Zebra	5	2	422.5	186.4	7.3	9.3	8.3	45.5	58.3	51.9	27.9
30	Zebra	5	3	404.5	178.9	7.3	10.7	9.0	45.8	63.9	54.9	30.7

Appendix C13: Timepoint group averages and standard deviations for surface tetras, cave tetras, and zebrafish at 10-, 15-, 20-, and 30-dpf. Averages and standard deviations provided for standard length, average scleral cartilage depth (Appendix C4, C5, C6), average scleral cartilage cell count (Appendix C7, C8, C9), and average relative scleral cartilage depth (Appendix C10, C11, C12).

Age	Type	Group Size (n)	Average Standard Length (mm)	Standard Deviation	Average Scleral Cartilage Depth (µm)	Standard Deviation	Average Scleral Cartilage Cell Count (# of cells)	Standard Deviation	Average Relative Scleral Cartilage Depth (%)	Standard Deviation
10	Surface T.	8	4.6	0.09	0.00	0.00	0.00	0.00	0.0	0.0
15	Surface T.	7	5.4	0.05	15.47	5.20	1.75	0.73	10.7	3.6
20	Surface T.	7	6.2	0.22	27.16	7.17	4.06	1.00	18.4	3.4
30	Surface T.	3	8.0	0.15	32.11	4.24	4.38	0.72	17.9	2.0
10	Cave T.	8	5.2	0.13	0.00	0.00	0.00	0.00	0.0	0.0
15	Cave T.	3	5.9	0.00	4.48	4.58	0.60	0.63	10.0	10.6
20	Cave T.	6	6.4	0.07	11.66	8.32	1.58	1.18	18.9	12.3
30	Cave T.	2	9.2	0.18	43.36	4.06	6.22	0.42	72.4	8.9
10	Zebra	6	4.4	0.12	0.00	0.00	0.00	0.00	0.0	0.0
15	Zebra	7	5.0	0.12	10.34	10.23	1.78	1.82	6.8	6.5
20	Zebra	7	5.7	0.30	36.68	9.84	6.52	2.02	20.4	4.5
30	Zebra	5	6.7	0.26	58.94	7.92	9.77	1.73	31.2	3.5

Appendix C14: Measurements and averages for rostral and caudal scleral cartilage offset in surface tetras, cave tetras, and zebrafish at 30-dpf.

Eye ID				Scleral Cartilage Offset Angles (°)							
Age	Type	Sample	Slide	Rostral Angle (section 1)	Rostral Angle (section 2)	Rostral Angle (section 3)	Caudal Angle (section 1)	Caudal Angle (section 2)	Caudal Angle (section 3)	Rostral Average	Caudal Average
30	Surface	1	7	-1.9	-2.9	-4.2	9.7	10.1	9.5	-3.0	9.8
30	Surface	1	7	-3.8	-4.8	-3.7	10.2	12.2	10.3	-4.1	10.9
30	Surface	2	4	-2.0	-2.8	-0.4	8.2	5.6	7.1	-1.7	7.0
30	Surface	2	4	-3.0	-2.4	-4.4	8.3	7.9	8.8	-3.3	8.3
30	Cave	1	6	11.1	9.2	8.2	36.3	42.5	31.4	9.5	36.7
30	Cave	2	6	18.1	25.4	20.9	23.8	25.0	30.0	21.5	26.3
30	Cave	2	7	18.9	13.0	15.8	9.6	8.1	10.9	15.9	9.5
30	Zebra	1	3	-2.4	-0.4	-1.4	6.2	7.3	7.9	-1.4	7.1
30	Zebra	1	3	-1.0	-1.8	0.6	9.2	7.7	9.1	-0.7	8.7
30	Zebra	2	7	-4.2	-3.7	-1.5	9.1	10.1	9.0	-3.1	9.4
30	Zebra	2	8	-2.0	-0.3	-3.0	8.2	8.6	9.2	-1.8	8.7
30	Zebra	3	2	-0.3	-0.9	-0.2	9.6	10.5	9.8	-0.5	10.0
30	Zebra	3	3	-1.4	-1.9	-0.6	11.0	8.7	12.1	-1.3	10.6
30	Zebra	4	3	-2.4	-2.1	-4.0	12.5	11.8	13.9	-2.8	12.7
30	Zebra	4	4	-3.8	-0.6	1.1	10.7	7.0	9.5	-1.1	9.1
30	Zebra	5	2	-1.0	2.9	0.4	9.3	8.5	10.5	0.8	9.4
30	Zebra	5	3	-3.9	-3.8	-7.4	8.6	3.6	7.2	-5.0	6.4

Appendix C15.: Scleral cartilage chondrocyte and retinal ganglion cell body cross-sectional area measurement data. Number measured is the number of scleral chondrocytes present in each section. RGC, retinal ganglion cell.

Age	Morph	Sample	Slide	Cell Type	Number Measured (n)	Cell Cross-Sectional Area (μm^2)											
15	Surface	1	6	Chondrocytes	4	45.15	35.26	21.64	22.46								
				RGC	4	8.59	9.13	12.16	8.03								
15	Surface	2	3	Chondrocytes	2	24.48	28.52										
				RGC	2	10.89	8.21										
15	Surface	3	4	Chondrocytes	4	23.69	30.3	29.38	29.82								
				RGC	4	10.28	10.66	10.93	11.6								
15	Surface	4	5	Chondrocytes	5	37.32	32.76	17.76	22.16	22.78							
				RGC	5	9.62	12.48	14.01	15.81	10.88							
15	Surface	5	4	Chondrocytes	1	37.01											
				RGC	1	12.42											
15	Surface	6	3	Chondrocytes	6	21.44	24.95	38.07	26.81	18.07	22.46						
				RGC	6	11.72	13.41	11.87	15.38	11.32	8.63						
15	Surface	7	7	Chondrocytes	4	22.67	25.01	18.79	22.45								
				RGC	4	10.69	10.18	13.87	12.77								
15	Cave	3	8	Chondrocytes	0												
				RGC	0												
15	Cave	4	3	Chondrocytes	2	24.4	19.24										
				RGC	2	10.42	10.03										
15	Cave	5	5	Chondrocytes	1	25.15											
				RGC	1	10.68											
20	Surface	1	6	Chondrocytes	5	25.34	11.44	17.45	30.07	30.9							
				RGC	5	15.05	13.97	19.71	12.44	15.44							
20	Surface	2	4	Chondrocytes	9	23.56	21.81	12.2	10.89	24.27	28.87	18.48	31.8	14.4			
				RGC	9	19.18	16.27	18.96	17.74	11.54	14.5	14.69	16.71	19.08			
20	Surface	3	6	Chondrocytes	6	37.62	29.1	38.26	40.34	38.68	83.37						
				RGC	6	23.38	21.95	19.85	17.22	20.29	12.5						
20	Surface	4	6	Chondrocytes	7	27.91	38	59.35	40	86.43	35.01	26.44					
				RGC	7	16.3	26.02	12.16	16.87	18.76	26.16	21.96					
20	Surface	5	5	Chondrocytes	12	7.88	16.71	17.61	61.09	33.99	24.49	20.89	29.75	19.51	40.66	40.6	31.61
				RGC	12	17.3	15.56	22.75	21.08	16.88	13.43	12.56	15.27	25.95	14.78	19.54	17.63
20	Surface	6	5	Chondrocytes	8	21.37	44.46	83.03	53.88	27.83	15.51	24.9	24.04				
				RGC	8	17.55	13.33	16.55	16.34	16.73	21.84	14.3	12.5				
20	Surface	7	2	Chondrocytes	9	34.13	88.61	76.19	29.83	15.27	20.48	30.87	58	34.26			
				RGC	9	15.93	18.05	21.74	16.72	20.83	22.08	19.34	15.7	16.91			
30	Surface	1	7	Chondrocytes	8	57.12	56.92	48.59	34.64	27.42	70.22	43.28	19.05				
				RGC	8	15.03	17.53	15.35	16.51	17.06	14.26	18.2	15.77				
30	Surface	2	4	Chondrocytes	7	46.61	30.25	37.19	43.39	29.41	30.33	51.36					
				RGC	7	19.06	17.4	18.21	12.5	10.49	15.53	17.61					
20	Cave	2	7	Chondrocytes	3	43.2	47.72	79.97									
				RGC	3	11.27	10.21	13.89									
20	Cave	3	8	Chondrocytes	3	30.11	83.43	44.85									
				RGC	3	19.65	13.64	17.45									
20	Cave	4	7	Chondrocytes	3	46.44	61.48	36.41									
				RGC	3	11.05	12.29	16.15									
20	Cave	5	4	Chondrocytes	8	58.79	66.47	31.37	27.56	58.05	49.91	19.38	26.8				
				RGC	8	16.68	13.68	19.58	10.85	13.61	16.99	12.43	19.84				
30	Cave	1	6	Chondrocytes	11	106.08	75.28	30.57	60.08	24.39	15.96	42.89	62.75	46.15	82.93	86.83	
				RGC	11	14.99	18.25	16.99	13.96	11	14.79	9.82	16.02	12.18	6.82	8.51	
30	Cave	2	6	Chondrocytes	10	53.92	29.05	63.87	96.49	69.51	97.69	36.72	57.59	56.87	45.55		
				RGC	10	12.86	9.69	20.46	11.04	13.73	14.77	14.58	17.11	17.67	11.9		

Appendix C.16: Post-injection survival data for non-treated and DMSO controls in Chapter 3. Non-treated (NT) fish were not injected, but their survival was recorded for control. n, number of fish; %, percent survival; hpf, hours post-fertilization.

			23-hpf		26-hpf	
Day-Post	NT		DMSO		DMSO	
Injection	n	(%)	n	(%)	n	(%)
0	10	100	12	100	12	100
1	10	100	9	75	10	83
2	10	100	8	67	9	75
3	10	100	8	67	9	75
4	10	100	8	67	9	75
5	10	100	8	67	9	75
6	9	90	8	67	9	75
7	9	90	8	67	9	75
8	9	90	8	67	9	75
9	9	90	8	67	9	75
10	9	90	8	67	9	75
11	9	90	8	67	9	75
12	9	90	8	67	9	75
13	9	90	8	67	9	75
14	9	90	8	67	9	75
15	9	90	8	67	9	75
16	9	90	8	67	9	75
17	9	90	8	67	9	75
18	9	90	8	67	9	75
19	9	90	8	67	9	75
20	9	90	8	67	9	75
21	9	90	8	67	9	75
22	9	90	8	67	9	75
23	9	90	8	67	9	75
24	9	90	8	67	9	75
25	9	90	8	67	9	75
26	9	90	8	67	9	75
27	9	90	8	67	9	75
28	9	90	8	67	9	75
29	9	90	8	67	9	75
30	9	90	8	67	9	75
31	9	90	8	67	9	75
32	9	90	8	67	9	75
33	9	90	8	67	9	75
34	9	90	8	67	9	75
35	9	90	8	67	9	75

Appendix C.16: Post-injection survival data for fish injected with SSR128129E in Chapter 3. n, number of fish; %, percent survival; hpf, hours post-fertilization.

	23-hpf		26-hpf		23-hpf		26-hpf	
Day-Post	SSR 0.25 mM		SSR 0.25 mM		SSR 0.5 mM		SSR 0.5 mM	
Injection	n	(%)	n	(%)	n	(%)	n	(%)
0	22	100	20	100	20	100	23	100
1	18	82	16	80	14	70	18	78
2	16	73	15	75	12	60	17	74
3	16	73	12	60	11	55	15	65
4	16	73	10	50	9	45	15	65
5	13	59	9	45	9	45	15	65
6	10	45	9	45	9	45	14	61
7	8	36	9	45	9	45	14	61
8	8	36	9	45	6	30	13	57
9	8	36	9	45	6	30	11	48
10	8	36	9	45	6	30	10	43
11	8	36	9	45	6	30	10	43
12	8	36	9	45	6	30	10	43
13	8	36	9	45	6	30	10	43
14	8	36	9	45	6	30	10	43
15	8	36	9	45	6	30	10	43
16	6	27	9	45	6	30	10	43
17	6	27	9	45	6	30	10	43
18	6	27	8	40	6	30	10	43
19	6	27	8	40	6	30	10	43
20	6	27	8	40	6	30	10	43
21	6	27	8	40	6	30	9	39
22	6	27	8	40	6	30	9	39
23	6	27	8	40	6	30	9	39
24	6	27	8	40	6	30	9	39
25	6	27	8	40	6	30	9	39
26	6	27	8	40	6	30	9	39
27	6	27	8	40	6	30	9	39
28	6	27	8	40	4	20	9	39
29	6	27	8	40	3	15	9	39
30	6	27	8	40	3	15	9	39
31	6	27	8	40	3	15	9	39
32	6	27	8	40	3	15	9	39
33	6	27	8	40	3	15	9	39
34	6	27	6	30	3	15	9	39
35	6	27	4	20	3	15	9	39

Appendix C.16: Post-injection survival data for fish injected with LY-364947 in Chapter 3. n, number of fish; %, percent survival; hpf, hours post-fertilization.

	23-hpf		26-hpf		23-hpf		26-hpf	
Day-Post	LY 0.25 mM		LY 0.25 mM		LY 0.5 mM		LY 0.5 mM	
Injection	n	(%)	n	(%)	n	(%)	n	(%)
0	20	100	24	100	22	100	25	100
1	15	75	22	92	16	73	20	80
2	14	70	21	88	16	73	19	76
3	14	70	18	75	12	55	19	76
4	12	60	17	71	10	45	19	76
5	12	60	17	71	10	45	19	76
6	12	60	17	71	10	45	19	76
7	10	50	17	71	10	45	19	76
8	10	50	17	71	10	45	19	76
9	10	50	17	71	10	45	16	64
10	10	50	17	71	7	32	16	64
11	10	50	17	71	7	32	15	60
12	10	50	17	71	7	32	15	60
13	10	50	17	71	7	32	15	60
14	10	50	17	71	5	23	14	56
15	10	50	17	71	5	23	14	56
16	10	50	17	71	5	23	14	56
17	10	50	17	71	5	23	14	56
18	10	50	17	71	5	23	14	56
19	10	50	17	71	5	23	14	56
20	10	50	17	71	5	23	14	56
21	8	40	17	71	5	23	14	56
22	7	35	17	71	5	23	14	56
23	7	35	17	71	5	23	14	56
24	7	35	17	71	5	23	14	56
25	7	35	17	71	5	23	14	56
26	7	35	17	71	5	23	13	52
27	7	35	17	71	5	23	13	52
28	7	35	17	71	5	23	13	52
29	7	35	17	71	5	23	13	52
30	7	35	17	71	5	23	13	52
31	7	35	17	71	5	23	13	52
32	7	35	17	71	5	23	13	52
33	7	35	17	71	5	23	13	52
34	7	35	17	71	5	23	13	52
35	6	30	17	71	4	18	13	52

Appendix C.17: Non-blind head skeleton assessment data. '0' indicated normal phenotype, '1' indicates abnormal phenotype. Timepoint column indicates injection timepoint.

Tube (#)	Inhibitor	Timepoint (hpf)	Concentration	Scleral Cartilage (0/1)	Basicapsular (0/1)	Basihyal (0/1)	Epiphyseal bar (0/1)
1	NT	-	-	0	0	0	0
1	NT	-	-	0	0	0	0
1	NT	-	-	0	0	0	0
1	NT	-	-	0	0	0	1
2	NT	-	-	0	0	0	0
2	NT	-	-	0	0	0	0
2	NT	-	-	0	0	1	0
3	NT	-	-	0	0	0	0
3	NT	-	-	0	0	0	0
4	DMSO	26	5%	0	0	0	0
4	DMSO	26	5%	0	0	0	0
4	DMSO	26	5%	0	0	0	0
4	DMSO	26	5%	0	0	0	0
5	DMSO	26	5%	0	0	0	0
5	DMSO	26	5%	0	0	0	0
6	DMSO	26	5%	-	0	0	0
6	DMSO	26	5%	0	0	0	0
7	DMSO	26	5%	0	0	0	0
8	DMSO	23	5%	0	0	0	0
9	DMSO	23	5%	0	0	0	0
9	DMSO	23	5%	0	0	1	0
9	DMSO	23	5%	0	0	0	0
9	DMSO	23	5%	0	1	0	0
10	SSR	26	0.25 mM	0	1	0	0
10	SSR	26	0.25 mM	0	0	1	0
11	SSR	26	0.5 mM	0	0	0	0
11	SSR	26	0.5 mM	0	0	0	1
11	SSR	26	0.5 mM	0	0	0	0
11	SSR	26	0.5 mM	0	0	1	1
11	SSR	26	0.5 mM	0	0	1	1
12	SSR	23	0.5 mM	0	0	0	1
12	SSR	23	0.5 mM	0	0	0	1
12	SSR	23	0.5 mM	0	0	0	1
12	SSR	23	0.5 mM	0	0	1	1
13	SSR	23	0.25 mM	0	0	0	1
13	SSR	23	0.25 mM	0	0	1	1
14	LY	26	0.5 mM	0	1	0	0
14	LY	26	0.5 mM	0	0	1	1
15	LY	26	0.5 mM	0	0	0	1
15	LY	26	0.5 mM	0	0	0	0
15	LY	26	0.5 mM	0	0	0	1
16	LY	26	0.5 mM	0	0	0	1
16	LY	26	0.5 mM	0	1	1	0
17	LY	26	0.5 mM	0	0	0	0
17	LY	26	0.5 mM	0	0	0	1
17	LY	26	0.5 mM	-	0	1	1
17	LY	26	0.5 mM	0	0	0	0

18	LY	26	0.5 mM	-	0	0	1
18	LY	26	0.5 mM	0	0	0	1
19	LY	26	0.25 mM	0	0	0	0
19	LY	26	0.25 mM	0	0	0	1
19	LY	26	0.25 mM	0	1	0	0
19	LY	26	0.25 mM	0	0	0	0
19	LY	26	0.25 mM	0	0	1	1
20	LY	26	0.25 mM	0	0	0	1
21	LY	26	0.25 mM	0	0	0	1
21	LY	26	0.25 mM	0	0	0	0
21	LY	26	0.25 mM	0	0	0	0
22	LY	26	0.25 mM	0	0	0	0
22	LY	26	0.25 mM	-	0	0	1
23	LY	26	0.25 mM	0	0	0	0
23	LY	26	0.25 mM	0	0	0	0
23	LY	26	0.25 mM	0	0	0	1
23	LY	26	0.25 mM	0	0	0	1
23	LY	26	0.25 mM	0	0	0	1
23	LY	26	0.25 mM	0	0	0	-
24	LY	23	0.25 mM	0	0	0	0
24	LY	23	0.25 mM	0	0	0	0
24	LY	23	0.25 mM	0	0	1	1
24	LY	23	0.25 mM	0	0	0	0
24	LY	23	0.25 mM	0	0	1	1
25	LY	23	0.25 mM	0	1	0	1
26	DMSO	23	5%	0	0	0	0
26	DMSO	23	5%	0	0	0	1
26	DMSO	23	5%	0	1	1	0
27	SSR	26	0.25 mM	0	0	1	0
27	SSR	26	0.25 mM	0	0	0	0
28	SSR	26	0.5 mM	0	0	0	0
28	SSR	26	0.5 mM	0	0	0	0
28	SSR	26	0.5 mM	0	0	1	0
28	SSR	26	0.5 mM	0	0	-	-
28	SSR	26	0.5 mM	0	0	1	0
29	SSR	23	0.5 mM	0	1	0	1
30	SSR	23	0.25 mM	0	0	1	0
31	LY	23	0.5 mM	0	1	0	1
31	LY	23	0.5 mM	0	0	0	0
31	LY	23	0.5 mM	0	0	0	0
31	LY	23	0.5 mM	0	0	0	0
32	LY	23	0.25 mM	0	1	0	1
32	LY	23	0.25 mM	0	1	0	0
32	LY	23	0.25 mM	0	0	1	1
32	LY	23	0.25 mM	0	1	0	1

Appendix C.18: Summary non-blind of head skeleton analysis. N, total number of fish analysed. Cart., cartilage. % indicates percent affected for each structure. Timepoint indicates injection timepoint.

Treatment	Timepoint (hpf)	N	Scleral Cartilage (n affected)	%	Basicapsular Cart. (n affected)	%	Basihyal Cart. (n affected)	%	Epiphyseal Bar (n affected)	%
NT	-	9	0	0	0	0.0	1	11.1	1	11.1
DMSO	23	8	0	0	1	12.5	1	12.5	0	0.0
DMSO	26	9	0	0	1	11.1	1	11.1	0	0.0
SSR 0.25 mM	23	6	0	0	0	0.0	3	50.0	3	50.0
SSR 0.25 mM	26	4	0	0	1	25.0	2	50.0	0	0.0
SSR 0.5 mM	23	3	0	0	1	33.3	1	33.3	3	100.0
SSR 0.5 mM	26	9	0	0	0	0.0	3	33.3	4	44.4
LY 0.25 mM	23	10	0	0	4	40.0	3	30.0	6	60.0
LY 0.25 mM	26	17	0	0	1	5.9	1	5.9	8	47.1
LY 0.5 mM	23	4	0	0	1	25.0	0	0.0	1	25.0
LY 0.5 mM	26	13	0	0	2	15.4	3	23.1	8	61.5

Appendix D: Summary of Statistical Analysis

In the following tables, the numbers in the group vs. group column (i.e., Surface 10 vs. Cave 10), indicates the age of the fish in days post-fertilization, dpf.

Appendix D.1: Summary of ANOVA and Post-Hoc Comparisons of Eye Depth.

Eye Depth			
ANOVA			
DF (between)	**DF (within)**	**F**	**p**
11	100	95.64	<0.0001
Post-Hoc Comparisons (Tukey Tests)			
Group vs. Group		**Mean Difference (µm)**	**p**
Surface 10 vs.Cave 10		62.84	<0.0001
Surface 10 vs. Zebrafish 10		-12.71	0.567
Cave 10 vs. Zebrafish 10		-75.55	<0.0001
Surface 15 vs.Cave 15		95.16	<0.0001
Surface 15 vs. Zebrafish 15		2.186	>0.9999
Cave 15 vs. Zebrafish 15		-92.97	<0.0001
Surface 20 vs.Cave 20		82.75	<0.0001
Surface 20 vs. Zebrafish 20		-32.96	<0.0001
Cave 20 vs. Zebrafish 20		-115.7	<0.0001
Surface 30 vs. Cave 30		119	<0.0001
Surface 30 vs. Zebrafish 30		-10.06	0.9885
Cave 30 vs. Zebrafish 30		-129	<0.0001

Appendix D.2: Summary of ANOVA and Post-Hoc Comparisons of Eye Width.

Eye Width			
ANOVA			
DF (between)	**DF (within)**	**F**	**p**
11	100	135.4	<0.0001
Post-Hoc Comparisons (Tukey Tests)			
Group vs. Group		**Mean Difference (µm)**	**p**
Surface 10 vs.Cave 10		87.13	<0.0001
Surface 10 vs. Zebrafish 10		-25.02	0.567
Cave 10 vs. Zebrafish 10		-112.1	<0.0001
Surface 15 vs.Cave 15		203	<0.0001
Surface 15 vs. Zebrafish 15		8.5	0.9998
Cave 15 vs. Zebrafish 15		-194.5	<0.0001
Surface 20 vs.Cave 20		218.9	<0.0001
Surface 20 vs. Zebrafish 20		-47.13	0.0019
Cave 20 vs. Zebrafish 20		-266	<0.0001
Surface 30 vs. Cave 30		232.4	<0.0001
Surface 30 vs. Zebrafish 30		-52.23	0.075
Cave 30 vs. Zebrafish 30		-284.6	<0.0001

Appendix D.3: Summary of ANOVA and Post-Hoc Comparisons of Scleral Cartilage Depth.

Scleral Cartilage Depth			
ANOVA			
DF (between)	**DF (within)**	**F**	**p**
11	100	72.17	<0.0001
Post-Hoc Comparisons (Tukey Tests)			
Group vs. Group		**Mean Difference (µm)**	**p**
Surface 10 vs.Cave 10		0	>0.9999
Surface 10 vs. Zebrafish 10		0	>0.9999
Cave 10 vs. Zebrafish 10		0	>0.9999
Surface 15 vs.Cave 15		10.99	0.1206
Surface 15 vs. Zebrafish 15		5.122	0.7762
Cave 15 vs. Zebrafish 15		-5.865	0.8952
Surface 20 vs.Cave 20		14.22	0.0009
Surface 20 vs. Zebrafish 20		-9.194	0.0417
Cave 20 vs. Zebrafish 20		-23.41	<0.0001
Surface 30 vs. Cave 30		-11.25	0.5893
Surface 30 vs. Zebrafish 30		-26.83	<0.0001
Cave 30 vs. Zebrafish 30		-15.58	0.0369

Appendix D. 4: Summary of ANOVA and Post-Hoc Comparisons of Relative Scleral Cartilage Depth.

Scleral Cartilage Relative Depth			
ANOVA			
DF (between)	**DF (within)**	**F**	**p**
11	100	63.31	<0.0001
Post-Hoc Comparisons (Tukey Tests)			
Group vs. Group		**Mean Difference (%)**	**p**
Surface 10 vs.Cave 10		0	>0.9999
Surface 10 vs. Zebrafish 10		0	>0.9999
Cave 10 vs. Zebrafish 10		0	>0.9999
Surface 15 vs.Cave 15		0.675	>0.9999
Surface 15 vs. Zebrafish 15		3.852	0.8472
Cave 15 vs. Zebrafish 15		3.177	0.9945
Surface 20 vs.Cave 20		-1.917	0.9998
Surface 20 vs. Zebrafish 20		-1.713	0.9997
Cave 20 vs. Zebrafish 20		0.2036	>0.9999
Surface 30 vs. Cave 30		-54.48	<0.0001
Surface 30 vs. Zebrafish 30		-13.28	0.0055
Cave 30 vs. Zebrafish 30		41.2	<0.0001

Appendix D.5: Summary of ANOVA and Post-Hoc Comparisons of Scleral Cartilage Cell Count.

Scleral Cartilage Cell Count			
ANOVA			
DF (between)	**DF (within)**	**F**	**p**
11	100	64.2	<0.0001
Post-Hoc Comparisons (Tukey Tests)			
Group vs. Group		**Mean Difference (n cells)**	**p**
Surface 10 vs.Cave 10		0	>0.9999
Surface 10 vs. Zebrafish 10		0	>0.9999
Cave 10 vs. Zebrafish 10		0	>0.9999
Surface 15 vs.Cave 15		1.142	0.8349
Surface 15 vs. Zebrafish 15		-0.05064	>0.9999
Cave 15 vs. Zebrafish 15		-1.192	0.7806
Surface 20 vs.Cave 20		2.64	0.0009
Surface 20 vs. Zebrafish 20		-2.445	0.0001
Cave 20 vs. Zebrafish 20		-5.086	<0.0001
Surface 30 vs. Cave 30		-1.858	0.6943
Surface 30 vs. Zebrafish 30		-5.395	<0.0001
Cave 30 vs. Zebrafish 30		-3.537	0.0015

Appendix D.6: Summary of ANOVA and Post-Hoc Comparisons of Scleral Cartilage Chondrocyte Area Compared with Retinal Ganglion Cell Body Area. 15-Sur-SC, 15-dpf surface tetra scleral cartilage; 15-Sur-RGC, 15-dpf surface tetra retinal ganglion cell.

Scleral Cartilage Cell Area			
ANOVA			
DF (between)	DF (within)	F	p
11	264	29.8	<0.0001
Post-Hoc Comparisons (Tukey Tests)			
Group vs. Group		Mean Difference (µm^2)	p
15-Sur-SC vs. 15-Sur-RGC		15.6	0.0013
15-Cave-SC vs. 15-Cave-RGC		12.55	0.9898
15-Sur-SC vs 15-Cave-SC		4.04	>0.9999
15-Sur-RGC vs. 15-Cave-RGC		0.9903	>0.9999
20-Sur-SC vs. 20-Sur-RGC		16.46	<0.0001
20-Cave-SC vs. 20-Cave-RGC		33.1	<0.0001
20-Sur-SC vs 20-Cave-SC		-13.66	0.0097
20-Sur-RGC vs. 20-Cave-RGC		2.978	0.9996
30-Sur-SC vs. 30-Sur-RGC		25.68	<0.0001
30-Cave-SC vs. 30-Cave-RGC		2.361	>0.9999
30-Sur-SC vs 30-Cave-SC		-17.38	0.0054
30-Sur-RGC vs. 30-Cave-RGC		45.43	<0.0001

Appendix D.8: Summary of ANOVA and Post-Hoc Comparisons of Surface Tetra Rostral and Caudal Scleral Cartilage Depth and Cell Count. Ros, rostral; Cau, caudal; Ros-10, rostral 10-dpf.

Rostral-Caudal Scleral Cartilage Depth (Surface Tetra)			
ANOVA			
DF (between)	DF (within)	F	p
7	72	47.58	<0.0001
Post-Hoc Comparisons (Tukey Tests)			
Group vs. Group		Mean Difference (µm)	p
Ros-10 vs Cau-10		0	>0.9999
Ros-15 vs Cau-15		-10.52	0.0015
Ros-20 vs Cau-20		-3.273	0.8858
Ros-30 vs Cau-30		-4.898	0.944

Rostral-Caudal Scleral Cartilage Cells (Surface Tetra)			
ANOVA			
DF (between)	DF (within)	F	p
7	72	53.45	<0.0001
Post-Hoc Comparisons (Tukey Tests)			
Group vs. Group		Mean Difference (n cells)	p
Ros-10 vs Cau-10		0	>0.9999
Ros-15 vs Cau-15		-1.111	0.0306
Ros-20 vs Cau-20		-0.25	0.9953
Ros-30 vs Cau-30		-0.75	0.9008

Appendix D.9: Summary of ANOVA and Post-Hoc Comparisons of Cave Tetra Rostral and Caudal Scleral Cartilage Depth and Cell count. Ros, rostral; Cau, caudal; Ros-10, rostral 10-dpf.

Rostral-Caudal Scleral Cartilage Depth (Cave Tetra)			
ANOVA			
DF (between)	DF (within)	F	p
7	72	47.58	<0.0001
Post-Hoc Comparisons (Tukey Tests)			
Group vs. Group		Mean Difference (µm)	p
Ros-10 vs Cau-10		0	>0.9999
Ros-15 vs Cau-15		-6.977	0.8188
Ros-20 vs Cau-20		-12.9	0.0284
Ros-30 vs Cau-30		-8.109	0.8847

Rostral-Caudal Scleral Cartilage Cells (Cave Tetra)			
ANOVA			
DF (between)	DF (within)	F	p
7	72	53.45	<0.0001
Post-Hoc Comparisons (Tukey Tests)			
Group vs. Group		Mean Difference (n cells)	p
Ros-10 vs Cau-10		0	>0.9999
Ros-15 vs Cau-15		-0.9333	0.7893
Ros-20 vs Cau-20		-1.958	0.0054
Ros-30 vs Cau-30		-1.333	0.6948

Appendix D.10: Summary of ANOVA and Post-Hoc Comparisons of Zebrafish Rostral and Caudal Scleral Cartilage Depth and Cell count. Ros, rostral; Cau, caudal; Ros-10, rostral 10-dpf.

Rostral-Caudal Scleral Cartilage Depth (Zebrafish)			
ANOVA			
DF (between)	DF (within)	F	p
7	9	81.47	<0.0001
Post-Hoc Comparisons (Tukey Tests)			
Group vs. Group		Mean Difference (μm)	p
Ros-10 vs Cau-10		0	>0.9999
Ros-15 vs Cau-15		-4.542	0.9224
Ros-20 vs Cau-20		-16.27	0.0004
Ros-30 vs Cau-30		-17.68	0.0017

Rostral-Caudal Scleral Cartilage Cells (Zebrafish)			
ANOVA			
DF (between)	DF (within)	F	p
7	92	59.24	<0.0001
Post-Hoc Comparisons (Tukey Tests)			
Group vs. Group		Mean Difference (n cells)	p
Ros-10 vs Cau-10		0	>0.9999
Ros-15 vs Cau-15		-0.8462	0.9471
Ros-20 vs Cau-20		-3.6	<0.0001
Ros-30 vs Cau-30		-3	0.0144

Appendix D.11: Summary of Epiphyseal bar Morphology PERMANOVA and Post-Hoc Comparisons for Zebrafish Injected at 23-hpf (analysis of principal component clustering for PC1 vs PC2, and PC3 vs PC4). NT, non-treated. PC, principal component.

PERMANOVA 23-hpf: PC1 vs PC2	
F	p
1.715	0.1343
Post-Hoc Comparisons (T-Tests)	
Group vs. Group	p
NT vs. DMSO	0.1713
NT vs. LY (0.25 mM)	0.8665
NT vs. LY (0.5 mM)	0.2381
NT vs. SSR (0.25 mM)	0.1376
NT vs. SSR (0.5 mM)	0.54
DMSO vs. LY (0.25 mM)	0.1091
DMSO vs. LY (0.5 mM)	0.5616
DMSO vs. SSR (0.25 mM)	0.0043
DMSO vs. SSR (0.5 mM)	0.3696

PERMANOVA 23-hpf: PC3 vs PC4	
F	p
1.145	0.339
Post-Hoc Comparisons (T-Tests)	
Group vs. Group	p
NT vs. DMSO	0.1216
NT vs. LY (0.25 mM)	0.3717
NT vs. LY (0.5 mM)	0.7029
NT vs. SSR (0.25 mM)	0.4905
NT vs. SSR (0.5 mM)	0.0348
DMSO vs. LY (0.25 mM)	0.8783
DMSO vs. LY (0.5 mM)	0.4842
DMSO vs. SSR (0.25 mM)	0.0592
DMSO vs. SSR (0.5 mM)	0.6645

Appendix D.12: Summary of Epiphyseal bar Morphology PERMANOVA and Post-Hoc Comparisons for Zebrafish Injected at 23-hpf (analysis of principal component clustering for PC1 vs PC2, and PC3 vs PC4). NT, non-treated. PC, principal component.

PERMANOVA 26-hpf: PC1 vs PC2	
F	**p**
1.714	0.1146
Post-Hoc Comparisons (T-Tests)	
Group vs. Group	**p**
NT vs. DMSO	0.5366
NT vs. LY (0.25 mM)	0.8733
NT vs. LY (0.5 mM)	0.2886
NT vs. SSR (0.25 mM)	0.064
NT vs. SSR (0.5 mM)	0.5919
DMSO vs. LY (0.25 mM)	0.5603
DMSO vs. LY (0.5 mM)	0.1029
DMSO vs. SSR (0.25 mM)	0.0355
DMSO vs. SSR (0.5 mM)	0.8323

PERMANOVA 26-hpf: PC3 vs PC4	
F	**p**
1.129	0.3504
Post-Hoc Comparisons (T-Tests)	
Group vs. Group	**p**
NT vs. DMSO	0.2954
NT vs. LY (0.25 mM)	0.317
NT vs. LY (0.5 mM)	0.1184
NT vs. SSR (0.25 mM)	0.8304
NT vs. SSR (0.5 mM)	0.937
DMSO vs. LY (0.25 mM)	0.421
DMSO vs. LY (0.5 mM)	0.4596
DMSO vs. SSR (0.25 mM)	0.3833
DMSO vs. SSR (0.5 mM)	0.3537

Appendix E: Full Protocols

Appendix E.1: Agarose Pre-embedding Protocol.

Fixed samples should be stored in 1X PBS. If necessary, decalcify samples with 10% EDTA prior to pre-embedding.

1. Prepare 1% agarose solution in a beaker with medium-low heat and stirring:
2. 10 mL 1X PBS
3. 0.1 g Agarose (IBI IB70071)
4. Continue heating and stirring until solution becomes clear.
5. Carefully remove beaker from heat and pour a small amount into a small plastic petri dish (enough for approximately 3 – 4 mm of depth).
6. Once slightly cooled, transfer samples to the agarose using forceps.
7. Orient the samples with there ventral side facing the bottom of the dish.
8. Continue to adjust samples, if necessary, as the agarose gel sets.
9. Once stable, allow the gel to set for an additional 20 minutes.
10. Using a razor blade, cut out the samples in small blocks of agarose and transfer to a clean glass vial containing 25% ethanol.
11. Continue with dehydration (Appendix E.2).

Appendix E.2: Paraffin Wax Embedding Protocol.

1. Allow samples to incubate in the following solutions:

a. 25% ethanol – 45 minutes

b. 50% ethanol – 45 minutes

c. 70% ethanol – 45 minutes

d. 90% ethanol – 45 minutes

e. 95% ethanol – 45 minutes

f. 100% ethanol – 60 minutes

g. 100% ethanol – 60 minutes

h. Citrisolv (Decon Labs 1601H) – 60 minutes

i. Citrisolv – 60 minutes

2. Blot of excess Citrisolv and transfer samples to a pre-heated metal mould containing molten paraffin wax (McCormick 39503002) (62°C).

3. Vacuum oven for two hours at 58°C with 15 mmHg.

4. Remove from oven, refresh wax, and return to oven with same conditions overnight.

5. Preheat forceps in block heater and label plastic block holders for each sample.

6. Remove samples from vacuum oven and refresh wax.

7. Adjust sample position with preheated forceps and touch the metal mould to an ice pack to secure the sample.

8. Place a plastic block holder on the mould and fill with molten wax.

9. Transfer to a -20°C freezer to harden overnight.

Appendix E.3: Tissue Sectioning Protocol.

1. Place glass slides on slide warmer.
2. Trim sample block with razor blade around the sample tissue.
3. Secure block onto microtome.
4. Unlock microtome safety lock.
5. Line up block with microtome knife as close as possible.
6. Section sample at 6 µm thickness and transfer ribbons to cardboard tray with paint brushes.
7. Wet brush and add a few drops of water to slide.
8. Pick up sections using wet brush and place on top of water on slide.
9. Remove excess water with a kimwipe (Kimtech).
10. Place slides on tray and transfer to warmer to dry overnight at 37°C.

Appendix E.4: Hall and Brunt's Quadruple Stain Protocol.

Place slides in the following reagents for the following time series:

<u>Hydration</u>

1. Citrisolv (Decon Labs 1601H) – 5 minutes
2. Citrisolv – 5 minutes
3. 100% EtOH – 1 minute
4. 100% EtOH – 1 minute

5. 90% EtOH – 1 minute
6. 70% EtOH – 1 minute
7. 50% EtOH – 1 minute
8. Distilled water – 2 minutes

Staining

1. Celestine Blue solution – 5 minutes
2. Distilled water – 1 minute
3. Mayer's Hematoxylin (Sigma Aldrich MKCD8359) – 5 minutes.
4. Distilled water – 1 minute
5. Alcian Blue solution – 5 minutes.
6. Distilled water – 2 minutes
7. Phosphomolybdic Acid (Sigma Aldrich SLCB5310) – 1 minute
8. Distilled water – 1 minute
9. Direct Red solution – 5 minutes.
10. Distilled water – 20 seconds
11. 100% ethanol - 20 seconds
12. 100% ethanol – 20 seconds

Clearing

1. Citrisolv – 1 minute
2. Citrisolv – 1 minute
3. Citrisolv – 1 minute
4. Citrisolv – 1 minute

Mounting

1. Add DPX mountant (Sigma 44581) to coverslip using wide opening of a Pasteur pipette.
2. Lower coverslip onto slide.
3. Use forceps to adjust cover slip and to remove any bubbles.

Leave slides overnight in fume hood to dry.

Appendix E.5: Detailed Intravitreal Injection Protocol.

1. Dechorionate and stage fish prior to the injection timepoint to determine precisely when injection should be performed.
2. Transfer dechorionated fish to a petri plate containing embryo medium (recipe in Appendix F.2).
3. Store in incubator at 28°C.
4. Set up additionally petri plates to later transfer fish post-injection (one plate per timepoint/concentration)
5. Also prepare a plate containing 0.01% MS-222 (recipe in Appendix F.3).

6. Prepare the injection apparatus by ensuring that gas flow is working, everything is operational.
7. Load a femtotip needle (Eppendorf 5242.957.000) with ~5 µL injection solution using a well-loading pipette tip.
8. Store loaded tip in incubator temporarily to keep solution warm.
9. Upon reaching injection timepoint (determined by restaging at predicted time), load needle into Patchman needle adjuster.
10. Test needle flow by performing test injection.
11. Measure size of injection bolus at the tip of the needle
12. Volume can be estimated using sphere volume formula.
13. Adjust injection pressure to achieve volume of 0.5 nL.
14. Anesthetize five embryos via submersion in 0.01% MS-222 at 28°C to prevent twitching.
15. Transfer embryos to a plate containing embryo medium and transfer to injection apparatus.
16. Place injections in the right eye of each fish and return to respective petri dish in incubator.
17. Complete all injection by repeating steps 14-16.
    a. Check bolus volume intermittently, adjust as necessary.
18. Monitor embryos each hour throughout the day, removing any dead.

19. At the end of the day, carefully transfer fish to labeled cups in an off-system tank in the fish room and raise as per the appropriate SOP/protocol.

Appendix E.6: Bone and Cartilage Staining Protocol.

Acid-Free Double Stain (Bone and Cartilage) – adapted from Walker & Kimmel, 2007 and optimized by Franz-Odendaal lab.

1. Fix larvae in 4% PFA in 1X PBS (2 hours at room temperature with agitation or
2. overnight at 4°C) – Store in 1X PBS
3. Put samples directly into 50% ethanol for 10 minutes at room temperature with gentle agitation.
4. Remove ethanol and add bone and cartilage staining solution (Appendix F.9) to tubes – incubate overnight at room temperature with gentle agitation.
5. Briefly rinse larvae with distilled water (inverting the tube twice).
6. Remove water and add bleach solution (Appendix F.11) to tubes for approximately 2.5 hours.
7. Check bleaching progress at the 2-hour mark, though more than 2.5 hour may be required.
8. Remove bleach and add 20% glycerol solution (Appendix F.12) – agitate tubes gently at room temperature for 30 minutes.
9. Replace 20% glycerol solution with 40% glycerol solution (Appendix F.12) – agitate tubes gently at room temperature for 2 hours.

10. Store larvae in 100% glycerol.

Appendix E.7: Isolation of pET-28b-RfxCas13d-His+ *E. coli.*

1. Streak pET-28b-RfxCas13d-His^{+} *E. coli* (Addgene on 141322; Kushawah et al., 2020) 1% LB agarose kanamycin^{+} plate (Appendix F.13) to isolate single colonies.
2. Incubate overnight at 37°C.
3. Using a sterile loop, inoculate 50 mL kanamycin^{+} LB broth (Appendix F.14) with *E.* coli from a single colony.
4. Incubate overnight at 37°C with orbital shaking.

Appendix E.8: Isolation of Plasmid DNA (Miniprep).

1. Aliquot overnight culture from Appendix E.7 into several 2 mL Eppendorf tubes.
2. Centrifuge tubes at 6000 RPM for three minutes.
3. Decant and discard supernatant (can be sterilized by mixing with household bleach 3%).
4. If necessary, briefly centrifuge and remove remaining supernatant with a micropipette.
5. Add 100 µL of miniprep solution I (Appendix F.15) to each tube and drag across the top of an Eppendorf tube holder to suspend *E. coli*.
6. Add 200 µL of miniprep solution II (Appendix F.16) to each tube and invert five times.
7. Incubate on ice for five minutes.
8. Add 150 µL of miniprep solution III (Appendix F.17) to each tube and invert several times.

9. Incubate on ice for five minutes.
10. Centrifuge tubes at 13000 RPM for five minutes at 4°C.
11. Transfer supernatant to new sterile 2 mL Eppendorf tubes (400 µL per tube).
12. Add one volume (400 µL) of 2 M $CaCl_2$ (Appendix F.19) to each tube and incubate at room temperature for 10 minutes.
13. Add 600 µL of 100% isopropyl alcohol (Sigma I9030) to each tube and mix by inversion several times.
14. Incubate at room temperature for 10 minutes.
15. Centrifuge tubes at 13000 RPM for five minutes at 4°C; pellet should form.
16. Carefully decant supernatant and remove any remaining with a micropipette.
17. Add 500 µL of cold 70% ethanol to each tube.
18. Centrifuge tubes at 13000 RPM for five minutes at 4°C.
19. Carefully decant ethanol and repeat steps 16-18.
20. Carefully decant ethanol and remove any remaining with micropipette.
21. Invert open tubes on a kimwipe and allow pellets to dry for approximately 20 minutes.
22. Once dry, add 10-100 µL TE buffer (Appendix F.21) (or nuclease-free water depending on downstream use).
23. Store short-term at 4°C, long-term at -20°C.

Appendix E.9: Restriction Enzyme Digest.

1. Thaw reagents (step 2) on ice.
2. In a sterile 0.5 mL Eppendorf tube:
    a. 1.0 µL pET-28b-RfxCas13d-His plasmid.
    b. 5.0 µL NEB 3.1 Buffer 10X (New England Biolabs B7203S)
    c. 1.0 µL BGLII (New England Biolabs R0144S)
    d. 1.0 µL NotI (New England Biolabs R0189L)
    e. 42 µL nuclease-free water
3. Incubate at 37°C for 20 minutes.
4. Run on agarose gel to verify (Appendix E.11, E.12)

Appendix E.10: Polymerase Chain Reaction (PCR).

1. Reconstitute DNA primers in TE buffer (Appendix F.21) to a concentration of 100 µM.
2. Flick tubes to resuspend and incubate at room temperature for approximately two hours.
3. Thaw 5X GoTaq PCR Buffer (Promega M791A), GoTaq DNA polymerase (Promega M300A), and Promega PCR Nucleotide Mix, 10 mM (Promega U144A).
4. Prepare PCR mix in sterile 0.5 mL Eppendorf tube suitable for PCR:
    a. 10 µL 5X GoTaq Buffer.
    b. 1 µL dNTP mix.
    c. 5 µL primer #1 (cas13d_universal primer).

d. 5 µL primer #2 (vax1-201_288-310 primer).

e. 0.25 µL GoTaq DNA polymerase.

f. 28.75 µL nuclease free water (bring to 50 µL total volume).

5. Centrifuge briefly to bring contents to bottom of tube.

6. Place tube in thermocycler and initiate PCR program:

a. Preheat lid to 104°C.

b. Initial denaturation – 94°C for 4 minutes.

c. Cycles (X30) – 94°C for 30 seconds; 60°C for 40 seconds; 72°C for 30 seconds.

d. Final extension – 72°C for 10 minutes.

e. Hold at 4°C (for when you are unable to immediately retrieve sample after completion).

7. Store short-term at 4°C, long-term at -20°C.

Appendix E.11. DNA Gel Preparation.

1. In a 250 mL Erlenmeyer flask, add 100 mL of 1X TAE (Appendix F.25) buffer and 0.8 – 2.0 g agarose (for preparation of 0.8% to 2.0% agarose gels respectively).

i) If making a bleach gel, use 99 mL 1X TAE and 1 mL household bleach (3%).

2. Stir contents with medium-low heat on a stir table (in a fume hood if using bleach), until solution becomes clear.

3. Remove from heat and incubate at room temperature until flask can be handled.

4. While waiting, prepare gel mould for pouring.

5. Once flask can be handled add 6 µL of 12000X Gel Red Nucleic Acid Stain (Biotium 41003) and swirl until dye is dispersed.

6. Pour molten agarose into gel mould, ensuring even spread and no leaks.

7. Place desired well-comb in gel mould

8. Cover with tin foil and incubate at room temperature until gel is set (>30 minutes).

Appendix E.12. DNA Gel Electrophoresis.

1. Prepare DNA samples for gel-loading in a sterile Eppendorf tubes:

    a. 0.5 µL DNA (ladder or PCR product)

        i) Ladders used were Promega 1 kb Step Ladder (Promega G6941), and

    b. 1.0 µL 6X gel-loading dye (Promega G190A)

    c. 4.5 µL nuclease-free water (bring to 6 µL total volume)

2. Gently remove well-comb and remove gel from mould.

3. Place gel in electrophoresis chamber, cover with 1X TAE (Appendix F.25) buffer.

4. Carefully load samples in wells.

5. Place cover on chamber, cover apparatus with tin foil.

6. Run at 80V for 90 minutes, monitoring throughout run period.

7. When fastest running bands have migrated 3/4 to 4/5 gel length, turn off and unplug apparatus.

8. Remove gel and place on tray from imaging.

9. TAE buffer can be reused for subsequent runs.

Appendix E.13. PCR Product Purification.

11. Prepare PCR product from Appendix E.10 for agarose gel electrophoresis in a sterile tube:

    a. 5.0 µL PCR product

    b. 1.0 µL 6X gel-loading dye

12. Run gel at 80V until DNA has migrated 3/4 to 4/5 gel length.

13. Carefully cut-out desired DNA band.

14. Determine mass in grams of cut-out piece of gel in a sterile Eppendorf tube.

15. Add 300 µL of binding buffer per 0.1 g of gel. (from Roche High Pure PCR Product Purification Kit (Sigma 11732668001))

16. Heat tube at 57°C with intermittent vortexing until gel has dissolved (approximately 30 minutes).

17. Place tubes in -80°C for 10 minutes – agarose should begin to precipitate; DNA stays in solution.

18. Centrifuge tubes at 13000 RPM for 15 minutes; agarose should pellet at bottom.

19. Transfer supernatant to sterile Eppendorf tubes (read below steps to determine appropriate volume per tube – need extra space for addition of solutions).

20. Add 1/10 volume of 3 M sodium acetate (Appendix F.20), vortex briefly.

21. Add 2 volumes of cold 95% ethanol, vortex briefly (should turn milky white if there is a lot of DNA)

22. Incubate at -80°C for at least 45 minutes (the longer the better).

23. Centrifuge samples at 13000 RPM for 15 minutes at 4°C – pellet should form.

24. Decant and discard ethanol.

25. Add cold 70% ethanol, centrifuge as above for two minutes.

26. Remove all ethanol from tube.

27. Invert open tubes on a kimwipe and allow pellets to dry for approximately 20 minutes.

28. Once dry, add 10-100 µL TE buffer (or nuclease-free water depending on downstream use).

Appendix F: Solution Recipes

Appendix F.1 Zebrafish Medium (E3 Medium) 60X Stock.

- In 600 mL distilled water, dissolve:
    - 34.8 g NaCl (BDH 9286)
    - 1.6 g KCl (MP 191427)
    - 5.8 g $CaCl_2 \cdot 2H2O$ (EMD CX0130)
    - 9.78 g $MgCl_2 \cdot 6H2O$ (Fisher Biotech BP214-500)
- Bring to 2 L final volume.
- pH to 7.2

Appendix F.2 Zebrafish Medium (E3 Medium) 1X Solution.

- Dilute 16.5 mL 60X stock to 1 L.
- Add 100 µL 1% methylene blue.

Appendix F.3: Buffered 0.1% MS222 – Lethal Dose (300 mL).

1. 0.1% MS222 powder in 300 mL H_2O
2. 615 µL 1M NaOH (Sigma-Aldrich S5881)

For anesthetic dose (i.e., 0.01%, dilute 1:10 in zebrafish water).

Appendix F.4: Paraformaldehyde Fixation Solution (PFA; pH 7.4, 500 mL).

1. Heat 400 mL 1X PBS in glass beaker to 60°C on a hot plate in fume hood.
    a. Add stir bar.

b. Monitor temperature using thermometer.

2. While wearing a mask, weigh out 20 g PFA and add to beaker.

3. Stir until solution is dissolved.

4. Cool solution to room temperature and adjust pH.

5. Top up to 500 mL with 1X PBS.

Divide solution into 50 mL aliquots and store at -20°C.

Appendix F.5: 10X Phosphate Buffered Saline (PBS; pH 7.4, 1 L).

1. In 800 mL distilled water, add:

    a. 80 g NaCl (BDH 9286)

    b. 2.0 g KCl (MP 191427)

    c. 11.5 g (Na_2HPO_4) sodium phosphate dibasic (Sigma 1.06586)

    d. 2.0 g ($Na_2H_2PO_4 * 2H_2O$) potassium phosphate monobasic (EMD SX0711)

2. Stir until dissolved.

3. Adjust pH to 7.4.

4. Top up to 1 L with distilled water.

Appendix F.6: 1X Phosphate Buffered Saline (PBS; pH 7.4, 1 L).

1. 100 mL 10X PBS.

2. Top up to 1 L with distilled water.

Appendix F.7: Inhibitor Stock Solutions (50.0 mM).

For a 50.0 mM stock of LY-364947

1. Weigh out 1.0 mg of desiccated LY-364947 (Abcam 141890).
2. Dissolve in 36.7 µL DMSO (Fisher D128-1)
3. Store at -80°C

For a 50.0 mM stock of SSR128129E

1. Weigh out 1.0 mg of desiccated SSR128129E (Abcam 146107).
2. Dissolve in 57.7 µL DMSO (Fisher D128-1)
3. Store at -80°C

Appendix F.8: Preparation of Inhibitor Injection Solutions (0.25 mM and 0.5 mM).

For a 0.25 mM solution of either inhibitor (starting from a 50.0 mM stock):

- In 95 µL zebrafish embryo medium (Appendix F1).
- Add 0.005 g phenol red (Sigma P3532).
- Add 5.0 µL of 50.0 mM inhibitor stock (Appendix F7).

For a 0.5 mM solution of the either inhibitor (starting from a 50.0 mM stock):

- In 90 µL zebrafish embryo medium
- Add 0.005 g phenol red (Sigma P3532).
- Add 10 µL of 50.0 mM inhibitor stock.

Appendix F.9: Bone and Cartilage Double-Stain Solution.

1 mL of staining solution = 990 µL Part A + 10 µL Part B

Part A:

- 100 mL 0.02% Alcian Blue, 4 mM $MgCl_2$, 70% ethanol solution:
    - 5 mL 0.4% Alcian Blue (Sigma A3157) in 70% ethanol
    - 70 mL 95% ethanol
    - 25 mL 20 mM $MgCl_2$

Part B:

10 mL solution:

- 0.5% Alizarin Red (Sigma A5533) in distilled water

Appendix F.10: 20 mM Magnesium Chloride

- 25 mL distilled water
- 0.1 g $MgCl_2 \cdot 6H2O$ (Fisher Biotech BP214-500)

Appendix F.11: Double-Stain Bleaching Solution.

Equal parts 3% H_2O_2 and 2% KOH

Example for 20 mL solution: 1.5% H2O2, 1% KOH:

- 0.2 g KOH (Sigma 221473) in 10 mL 1X PBS (makes 2% KOH).
- 10 mL 3% H_2O_2 (generic drug store brand).

Appendix F.12: Double-Stain Glycerol-PBS Solutions.

20% Glycerol in 1X PBS (50 mL)

- 10 mL Glycerol (VWR BDH1172)
- 40 mL 1X PBS

40% Glycerol in 1X PBS (50 mL)

- 20 mL Glycerol (VWR BDH1172)
- 30 mL 1X PBS

Appendix F.13: 1% LB Agarose Kanamycin$^+$ Plates.

- In a flask with 200 mL distilled water:
    - Dissolve 8 g Difco LB agar (Difco 244520) with heat and stirring.
- Autoclave solution.
- Once cooled (able to be handled), add 200 µL 1000X kanamycin (Sigma 60615)
- Pour evenly into sterile petri plates and allow to cool.
- Store inverted at 4°C.

Appendix F.14: Kanamycin$^+$ LB Broth.

- In a sterile, autoclavable bottle:
    - 100 mL distilled water
    - 2.5 g Difco LB broth (Difco 244620)

- Autoclave solution.
- Store at 4°C until use.

Appendix F.15: Miniprep Solution I – Resuspension Buffer (50mL stock).

- 1.25 mL 1M Tris-Cl.
- 1 mL 0.5M EDTA.
- 0.4504 g glucose (50mM final conc.).
- pH to 8.0.
- Top up to 50mL with sterile H_2O.

Appendix F.16: Miniprep Solution II – Denaturing Solution (50mL stock).

- 10mL 1N NaOH.
- 5mL 10% SDS (0.5g SDS in 5 mL DEPC-H2O).
- Add 35 mL sterile H_2O.

Appendix F.17: Miniprep Solution III – Renaturing Solution (50mL stock).

- 30 mL 5M potassium acetate
- 5.75 mL glacial acetic acid (Fisher UN2789)
- 14.25 mL sterile H_2O

Appendix F.18: 5M Potassium Acetate (50mL, stock).

- 24.5375 g potassium acetate (Sigma, P1190)
- 10 mL sterile H2O

Appendix F.19: 2M Calcium Chloride.

- In 70 mL distilled water:
    - Dissolve 29.4 g $CaCl_2$ (EMD CX0130).
- Adjust volume to 100 mL with distilled water.

Appendix F.20: 3M Sodium Acetate.

- In 50 mL distilled water:
    - Dissolve 24.6 g sodium acetate (Sigma 2889)
- Adjust pH to 5.2 with glacial acetic acid (Fisher UN2789)
- Top up to 100 mL with distilled water.
- Autoclave.

Appendix F.21: TE Buffer.

- 0.2 mL 0.5 M EDTA (pH 8.0)
- 1.0 mL 1M Tris-Cl (pH 8.0)
- Top up to 100 mL with DEPC-treated water.

Appendix F.22: 0.5 M EDTA (pH 8.0).

- In 80 mL distilled water:
    - Dissolve 18.6 g EDTA (Sigma E5134).
- Adjust pH to 8.0.
- Top up to 100 mL with distilled water.

- Autoclave

Appendix F.23: 1M Tris-Cl (pH 8.0).

- In 80 mL distilled water:
    - Dissolve 12.11 g Tris (Sigma 93362).
- pH to 8.0.
- Top up to 100 mL with distilled water.
- Autoclave.

Appendix F.24: 10X TAE Buffer Stock.

- In 800 mL distilled water:
    - 48.4 g Tris base (Roche 03 118 142 001).
    - 11.4 mL glacial acetic acid (Fisher UN2789).
    - 3.7 g EDTA (Sigma E5134).
- Top up to 1 L with distilled water.

Appendix F.25: 1X TAE Buffer.

- Dilute 100 mL 10X TAE Stock to 1 L with distilled water.